Automatic Edema Segmentation and Quantification from Cardiac MRI with 3D Visualization

By
Kushsairy Abdul Kadir

In the fulfilment of the requirement for the degree of
Doctor of Philosophy

Centre for excellence in Signal and Image Processing,
Department of Electronic and Electrical Engineering,
University of Strathclyde

Declaration

I declare that this Thesis embodies my own research work and that it is composed by myself. Where appropriate, I have made acknowledgments to the work of others.

Kushsairy Abdul Kadir

Acknowledgment

It is a pleasure to thank the many people who made this thesis possible. I would like to begin with expressing my deepest gratitude to my PhD supervisor, Prof. John J. Soraghan. Throughout my PhD, he provided encouragement, guidance, and valuable input to my research. He has provided unlimited mental and practical support to numerous personal concerns. His enthusiasm in research, systematic organisation in work and optimistic attitude towards life positively influenced my study and life. Hence without his help and support, this thesis would never have been completed.

I sincerely thank postdoctoral member of staff Dr Hao Gao who, as a collaborator in the project, has actively participated and provided his technical input to the research. MRI data and related supported were provided by Professor Collin Berry's group (Dr Alex Payne) from the University of Glasgow. They provided essential help in MRI data processing (tissue characterization from MRI and segmentation). I also would like to thank Prof. Xiaoyu Luo's Group for his valuable discussions and suggestions during group meetings. Another group that should be mentioned is the doctors and staff at Golden Jubilee National Hospital for giving me full access and help while collecting the MRI data.

I would like to extend my sincere gratitude to my sponsor, Majlis Amanah Rakyat (MARA), and my employer University Kuala Lumpur (UniKL) for giving me the opportunity to pursue my PhD in the University of Strathclyde.

My deepest and sincere thanks are always to my parents, parent-in-laws, brothers, sisters, brother-in-laws and sister-in-laws for their constant support and prayers. I am so lucky and so proud to have such a wonderful family.

Most importantly, I owe my loving thanks to my wife Haidawati, daughters Adriana and Arissa and Son Adam without their understanding, endless patience and encouragement it would have been impossible for me to finish this work.

Abstract

The extent of myocardial edema delineates the ischemic area-at-risk (AAR) after myocardial infarction (MI). Since AAR can be used to estimate the amount of salvageable myocardial post-MI, edema imaging has potential clinical utility in the management of acute MI patients. T_2 weighted Cardiac Magnetic Resonance (CMR) imaging is widely used to investigate the extent of edema with recent acute MI patient.

This thesis describes new approaches and methods of automatic edema segmentation and quantification with 3D visualization. An integrated approach has been developed, including the localization of Left Ventricle (LV) wall, segmentation of myocardial wall, segmentation and quantification of edema and 3D visualization and quantification.

A novel automatic segmentation of LV wall is proposed. First a new LV wall localization algorithm is used to locate the centre of the blood pool region of the LV wall. Then a novel LV wall segmentation algorithm is used to segment the LV wall from the rest of anatomical structure. The advantage of the proposed method is in its ability to automatically localize the blood pool region of LV wall and the additional shape constraint which is adaptive to the data.

A novel, Automatic Edema Segmentation and Quantification algorithm is presented which is developed based on a statistical mixture model. The technique takes advantage of the characteristic of the MRI signal where the signal is governed by a Rician distribution and using this information regions of edema are segmented over the rest of LV wall. A post-processing step in used to include microvascular obstruction as part of the edema region. The computational simplicity and good edema discrimination are described.

Finally, a novel integrated approach to 3D visualization and quantification algorithm is presented. It extracts the information of the LV wall boundary and edema boundary. Then the information is used to generate an interactive 3D image which helps the clinician to visualize the extent of edema and its location. This edema quantification and 3D visualization method is evaluated by expert clinicians with favourable results.

CONTENTS

List of Figures

List of Tables

List of Acronyms

2D	Two dimensional
3D	Three dimensional
4D	Four dimensional
AAM	Active appearance model
AAR	Area at risk
AMI	Acute myocardial infarction
ASM	Active shape model
ASMM	Automatic statistical mixture model
CAD	Coronary artery disease
CeSIP	Centre for excellence in Signal & Image Processing
CHD	Coronary heart disease
CHF	Congestive heart failure
CMR	Cardiovascular magnetic resonance
CT	Computer tomography
CVD	Cardiovascular disease
DFT	Discreet Fourier transform
DGVF	Directional Gradient Vector Field Snake
DSC	Dice similarity coefficient
ED	End diastole
EDV	End-diastolic volume
EM	Expectation Maximization
ES	End systole
ESV	End-systolic volume
FHL	Fuzzy horizontal line
FID	Free induction decay
FOV	Field of view
FVL	Fuzzy vertical line
GVF	Gradient vector field
HTOSA	Hybrid thresholding edema quantification algorithm
LA	Long axis
LE	Late enhance
LSM	Level set method
LSMwASC	Level set method with additional shape constraint
LV	Left ventricle
LVCP	Left ventricle centre point
M	Magnetization
MI	Myocardial infarction
MR	Magnetic resonance
MRI	Magnetic resonance imaging
MVO	Microvascular obstruction
NMI	Normalize mutual instruction
NMR	Nuclear magnetic resonance
NMV	Net magnetization vector
NSTEMI	Non ST elevation myocardial infarction
PCA	Principle component analysis

RF	Radio frequency
ROI	Region of interest
RS_{FC}	Right sided fuzzy centre
RV	Right ventricle
SA	Short axis
SD	Standard deviation
STEMI	ST elevation myocardial infarction
TE	Echo time
TR	Repetition time

CHAPTER 1

1. INTRODUCTION

1.1 Introduction

Cardiovascular disease (CVD) is one of the major causes of death in modern society. In Scotland alone death rates from coronary heart disease (CHD) are among the highest in the world, and are the second highest in Western Europe. CHD is the second most common cause of death after cancer in Scotland; in 2008 16% of deaths were attributed to it (Macgregor, 2009, pp 230-266).

With advancement in the treatment of heart attack more people can survive from heart attack, thus many people are living with injured hearts. Since MR imaging is a non-invasive diagnostic technology which can provide serial pathology and function after a heart attack, it is the modality of choice for clinicians.

Myocardial infarction (MI) or heart attack is the result of the complete occlusion of one or more of the coronary arteries, which supply oxygen-rich blood to the heart muscle (myocardium). The timely quantification of area at risk (AAR) (Reimer et al., 1977) after MI and the distinction between viable and non-viable myocardial tissue are essential for cardiac treatment decision making. Myocardial edema, characterized by fluid retention in myocardial tissue due to damaged tissue resulting swelling in the affected area, has been demonstrated to be a promising feature for characterizing AAR (Abdel-Aty et al., 2009). Moreover edema has a significant impact on left ventricle (LV) function (Miyamoto et al., 1998). Currently, myocardial edema can be accurately detected by using T_2-weighted cardiovascular magnetic resonance (CMR) (Aletras et al., 2008, Giri et al., 2009, Payne et al., 2011), appearing as a relatively bright area compare to the non-infarcted myocardial tissue as shown in Figure 1.1

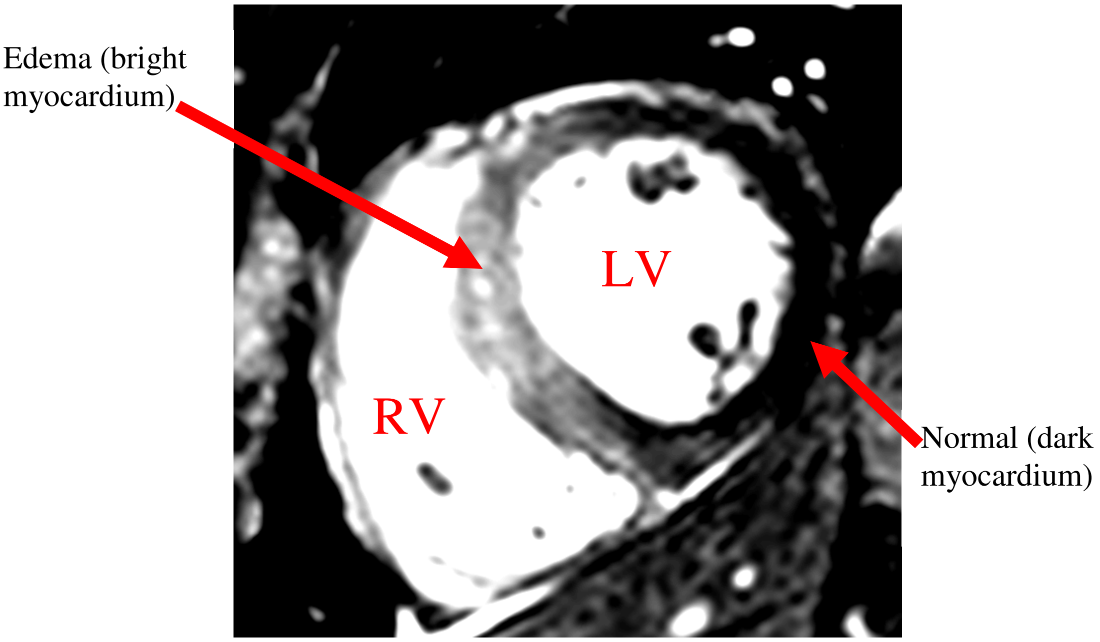

Figure 1.1: Short Axis T_2-Weighted Image

1.2 Motivation of Our Research

The current technique to quantify the size of edema is performed manually where an expert clinician will delineate the LV wall area first and then segment the edema area from the normal wall area of the LV on every short axis (SA) MR image from the basal to the apex of a CMR image stack. This process is both time consuming and suffers from inter- and intra- observable variations. Figure 1.2 shows a screen shot of segmentation by a clinician on a single slice. Thus this thesis looks into the problem of automatic edema quantification and 3D visualization.

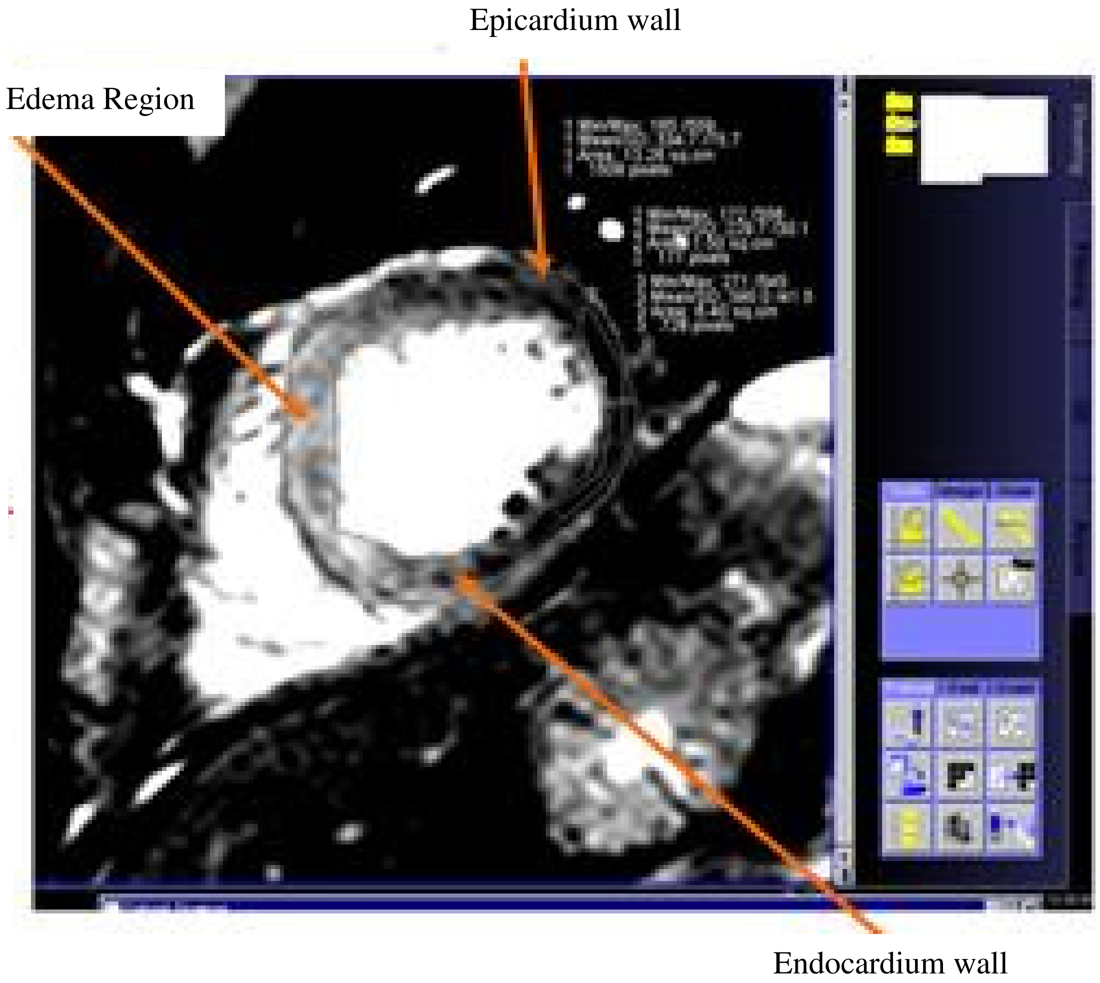

Figure 1.2: Screen shot of Manual Segmentation (courtesy of Golden Jubilee National hospital, Glasgow)

There is a need of developing automatic edema segmentation and quantification methods because to the best of our knowledge no known commercially available systems exist.

3D visualization of anatomical object provides significant information about the objects and their properties from which the images are derived. However, the significant potential for 3-D visualization in medicine remains largely unexploited, and practical tools remain undeveloped. Thus this motivates the work in the development of 3D visualization of edema, which will provide significant improvement on how the clinicians view the pathological structure of edema within the LV wall.

1.3 Summary of Original Contribution

In this work, the main research contributions are described below:

1) A new LV wall localization based on fuzzy logic is implemented. The technique incorporates the knowledge of the LV position in a CMR image in a fuzzy way to classify a few candidate pixels points as guidance point to initialise the level set. The detection of the centre point is achieved using the knowledge from the observation of a typical SA CMR image

2) A new segmentation method for LV wall is implemented using Level Set Method with Additional Shape Constraint (LSMwASC). The technique improves conventional Level set method (LSM) by creating new edge indicator function from typical LV wall thickness information. First conventional LSM is used to segment the endocardium. Then convex hull is applied to the result of the endocardium to remove the papillary muscle. Next a new constraint for the epicardium is introduced by estimating the thickness of the septum. Finally this information is used to create new edge map for the segmentation of the epicardium.

3) A new Hybrid Thresholding Edema Quantification Algorithm (HTOSA) is implemented. The automatic technique used to segment and quantify edema by automatically set the threshold value from image intensity information and the used of feature analysis to eliminate spurious small positive bright object on the LV wall and to include the microvascular obstruction within the edema boundary.

4) New Automatic Statistical Mixture Model (ASMM) is implemented. The technique used a Rayleigh distribution combined with Gaussian distribution to automatically set the threshold value for edema region. Then a post processing stage which consists of morphological filtering and Region Feature Analysis is applied to include microvascular obstruction into the final edema region.

5) New 3D edema visualization is implemented. The technique consists of 3D reconstruction from SA image stack information and 3D reconstruction with inclusion of the apex region. This is achieved by manually segmenting the apex region in a long axis view (LA). Then using the CMR scan information the location of each SA slice can be determined on the LA view. Rigid motion correction is performed to eliminate motion effect from the SA view onto the LA view.

6) A database of T_2 weighted CMR images have been established. Currently there is no publicly available database for T_2 Weighted for the investigation of edema. The database is developed with collaboration from Golden Jubilee National Hospital Glasgow, from which an annotated database of over 30 patients was created.

1.4 Organization of the Thesis

The organization of the thesis is as follows:

Chapter 1 describes the objective and motivation for the research, as well as original contribution that are presented in this work.

Chapter 2 provides fundamental information about the anatomy, physiology, and common pathologic conditions of human heart. This is followed by background information on Magnetic Resonance Imaging such as the principle behind image reconstruction, MRI instrumentation, Cardiac MRI and lastly some MRI image artefact.

Chapter 3 provides a review of image processing techniques in various stages of the automatic edema quantification and 3D visualization used in this research. A background review of LV wall segmentation methods is presented. This inspires our work on new Level Set Method with Additional Shape Constraint for the segmentation of the LV wall. The chapter also reviews current research on edema segmentation and quantification technique, which provides basic understanding on our new Automatic Statistical Mixture Model for the segmentation and quantification of edema. Finally the chapter review current application of 3D visualization in CMR imaging that motivates our work on 3D visualization of edema.

Chapter 4 introduced the CMR data collection such as the study protocol and the type of scanner been used. The chapter also discusses the assessment parameters used to test the proposed system for evaluating its performance.

Chapter 5 presents the background of Level Set Method and from the conventional LSM we derive a new LSM to segment the LV wall from the T_2 weighted images. The formulation takes into account the special characteristic of the T_2 weighted images. The results obtained by the automatic method are then compared with manual segmentation to assess the performance of the proposed method.

Chapter 6 presents two new methods for the segmentation and quantification of edema on T_2 weighted image. A comparative study is then performed to assess the performance of both algorithm with conventional 2SD and Fuzzy C-mean algorithm to assess the performance of the new algorithms.

Chapter 7 provides new 3D quantification and visualization of edema from a stack of SA images for 3D reconstruction. The chapter describes how the 3D image is reconstructed and how the proposed method has potential clinical application. The chapter also provides experimental results by comparing the proposed 3D method with 3D quantification and visualization from manual delineation for performance evaluation.

Chapter 8 presents the summary of the research and with some suggestions for future work.

CHAPTER 2

2. HUMAN HEART ANATOMY AND CARDIAC MAGNETIC RESONANCE

2.1 Introduction

One of the main cardiac illnesses is heart attack which is due to complete occlusion of one or more of the coronary arteries, which supply oxygen-rich blood to the heart muscle (myocardium). After heart attack, blood is retained within the myocardial tissue due to damage tissue causing swelling in the affected area of heart attack. This phenomenon is known as edema. The importance of studying edema is to differentiate between viable myocardial tissue and dead myocardial tissue.

Magnetic Resonance (MR) Imaging is a non-invasive imaging technique that creates detailed images of organ and tissues. Unlike other imaging modality such as CT-scan and X-ray, MR imaging uses a non-ionizing radiation and has no known risk of causing cancer. The earliest study on the use of MR imaging to produce images of body was conducted by Dr Paul Lauterbug (Lauterbur, 1973). This was followed up by the development of mathematical reconstruction algorithms by Peter Mansfield (Mansfield, 1977). Since then significant advancements in the field of magnetic imaging from existing 2D imaging up to 4D MR imaging are used to produce detailed images of internal organs of the human body.

In the studies of cardiovascular disease, CMR imaging is widely used to diagnose physiological function of the heart and pathological insight into myocardial injury. Thus CMR imaging plays a significant role in clinical diagnosis and follows up treatment of CVD.

This chapter provides information on heart anatomy and MR imaging system. Section 2.2 and Section 2.3 describe fundamental of heart anatomy and its physiological function. Section 2.4 explains some common heart diseases. In Section 2.5 the principle of MRI is discussed and includes MR imaging hardware, image acquisition. Section 2.6 introduces CMR imaging techniques and diagnostics. Section 2.7 discusses MR image artefact. The chapter is then concluded with Section 2.8.

2.2 Anatomy of the Heart

Figure 2.1 shows the detailed anatomy of the heart. The heart is located under the ribcage in the centre of the chest between the right and left lung. It is shaped like an upside-down pear. The beating action of its muscular walls beat, pumps blood continuously to all parts of the body. The size of a heart can vary depending on age, size, or heart condition. A normal, healthy, adult heart most often is the size of an average clenched adult fist

The heart wall consists of the epicardium (outer layer), the myocardium (middle layer comprised of cardiac muscle tissue), and the endocardium (inner layer). The heart consists of four chambers: the left ventricle (LV), the right ventricle (RV), the left atrium and the right atrium. The wall that separates the epicardium and the endocardium is called septum. The papillary muscles attach to the lower portion of the interior wall of the ventricles. They connect to the chordae tendineae, which attached to tricuspid valve in the RV and the mitral (bicuspid) valve in the LV. The contraction of papillary muscles opens these valves. When the papillary muscle relaxes, the valve close (Martini and Nath, 2009). The two ventricles are clearly identified in Figure 2.1 by the thick layer of the myocardium that makes up their walls. The short axis (SA) slices used in CMR images have a similar appearance to the transverse view (below) where regular contours, consisting of two concentric circles, can be readily fitted to the LV endocardium and epicardium. This is very useful in cardiac image analysis.

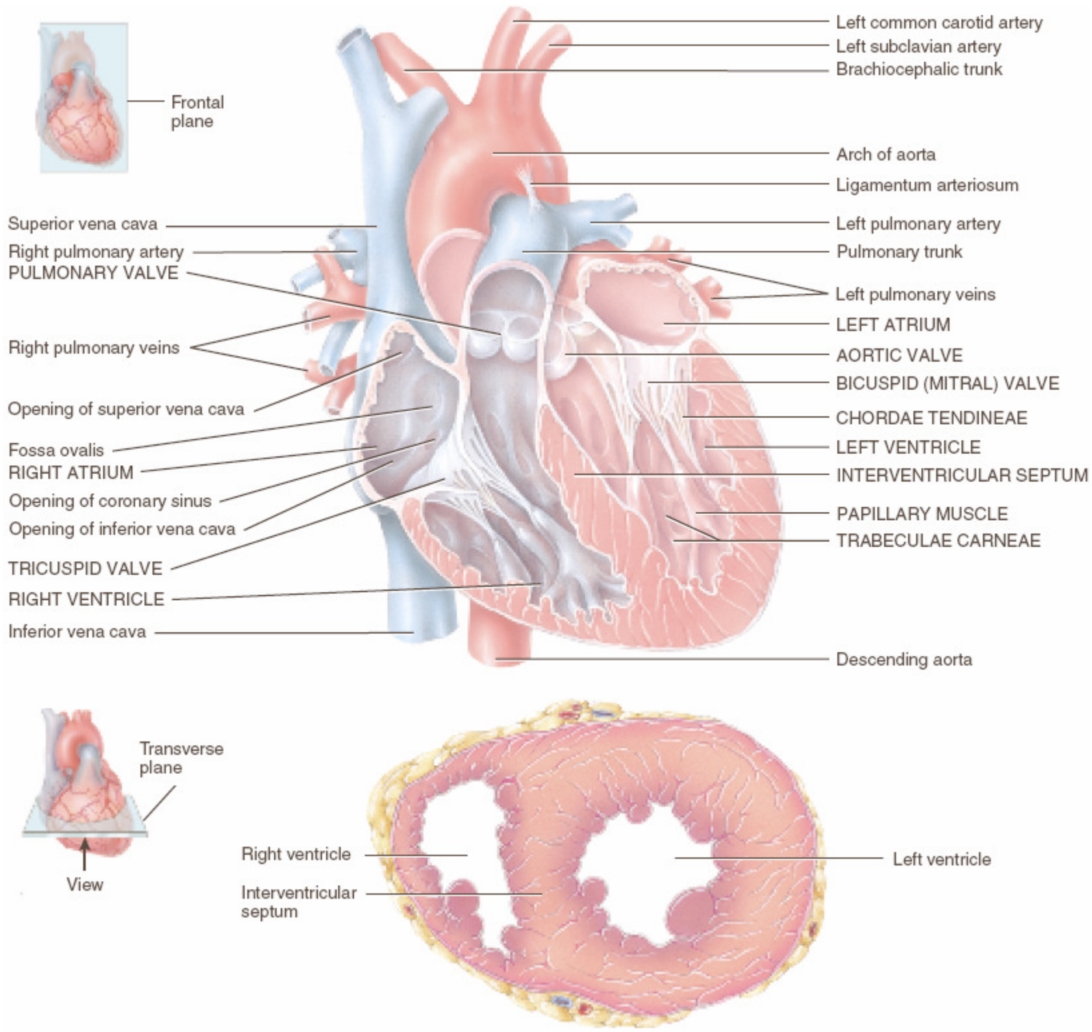

Figure 2.1 Anatomy of Heart in Frontal and Transverse View (G. J. Tortora and Derrickson, 2005)

2.3 Physiology of the Heart

The periodic motion of the walls of the heart chambers during one heartbeat is referred to as one cardiac cycle. One heart beat consists of rhythmic contraction (systole) and relaxation (diastole) of both atria and ventricles. Figure 2.2 shows one cardiac cycle. The cycle begins with atrial systole where blood is actively pumped from the atria into the ventricles. The end of the atrial systole marks the end of the ventricular diastole. The volume of blood (end-diastolic volume or EDV) contained in each of the ventricles reaches their maximum at end-diastole (ED). Ventricular systole causes the pressure inside the ventricles to rise sharply and ejection of blood from the heart through the aortic or pulmonary valves begins. The end-systolic volume (ESV) is computed at end-systole (ES) when the blood volume in the ventricles reaches a minimum. The volume changes during the entire cycle and the corresponding electrocardiogram (ECG) are presented in Figure 2.2.

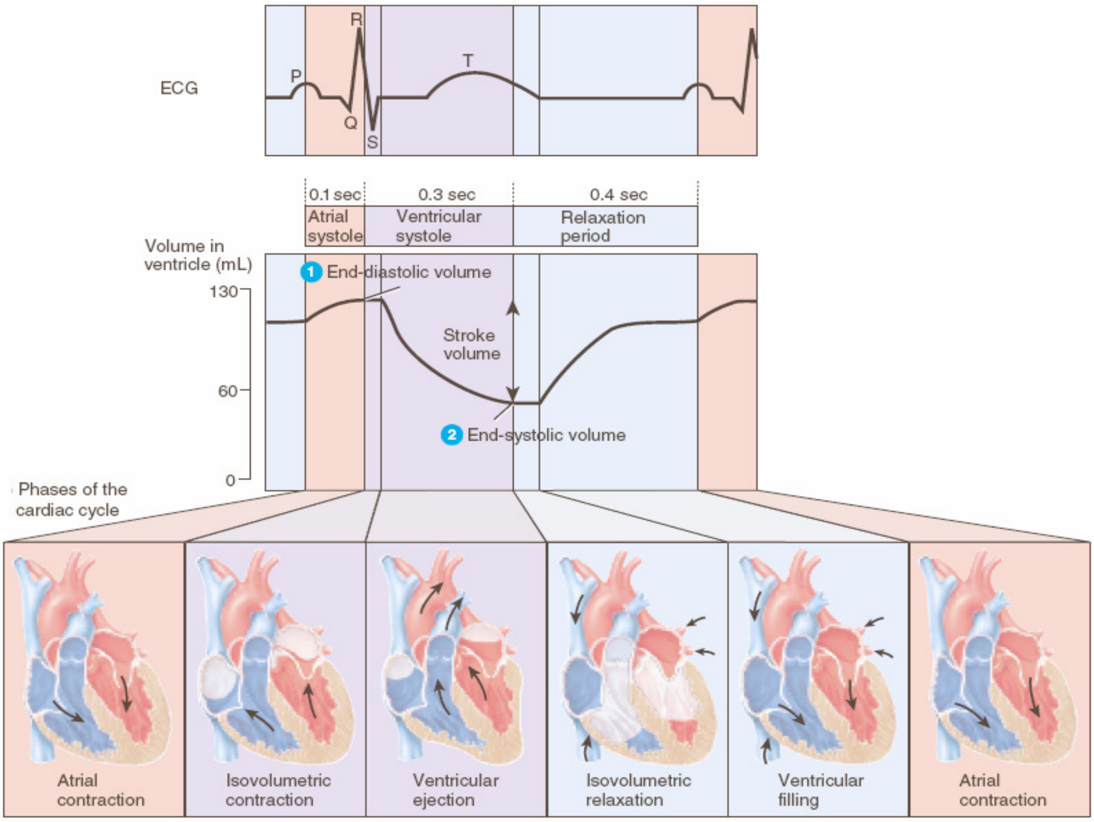

Figure 2.2: ECG, Volume change and phases in Cardiac cycle (G. J. Tortora and Derrickson, 2005)

2.4 Cardiovascular Disease

This section gives a brief introduction to some common causes of CVD, with special emphasis on the heart conditions diagnosed using the image processing techniques discussed in this thesis.

2.4.1 Coronary artery disease (CAD)

CAD refers to partial or complete blockage of coronary circulation by fatty deposits (plaque) (G. J. Tortora and Derrickson, 2005). The condition when the plaque builds in the inner wall of the arteries is known as atherosclerosis as shown in Figure 2.3

where the coronary artery narrows because of the deposit of plaque in its inner wall. As the size of the plaque increases, it reduces the blood flow to the heart muscles. Over time CAD can weaken the heart muscles and lead to heart failure.

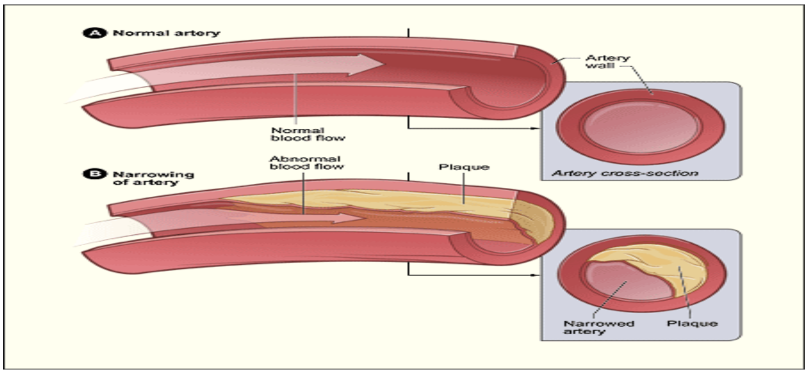

Figure 2.3: (A) Normal Artery with normal Blood Flow, and (B) Artery with plaque build-up (National Heart Lung and Blood Institute)

2.4.2 Acute myocardial infarction

Acute myocardial Infarction (AMI) or commonly known as heart attack as shown in Figure 2.4 is a condition when there is a sudden obstruction of the coronary artery by a blood clot. The blockage of the artery deprives the heart muscle of blood and oxygen, causing injury to the heart muscle(G. J. Tortora and Derrickson, 2005).

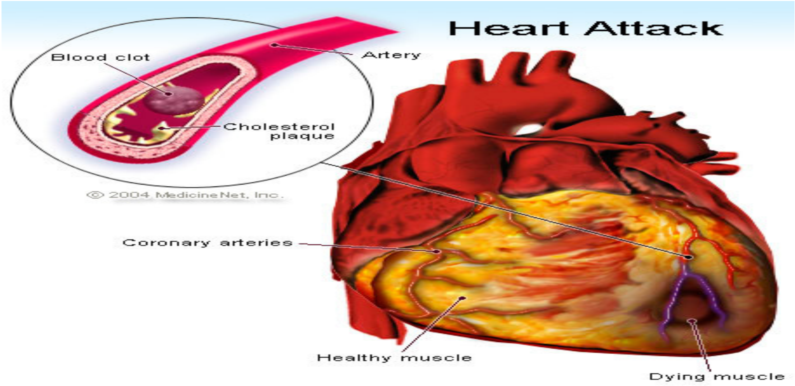

Figure 2.4: Acute Myocardial Infarction (Medicinenet)

Myocardial infarction can be classified based on its Electrocardiogram (ECG) pattern. From the ECG pattern two MI can be classified: (i) ST elevation MI

(STEMI) due to total blockage of the artery Figure 2.5(a), and (ii) NST elevation MI (NSTEMI) due to partial blockage of the artery as shown in Figure 2.5(b).

STEMI size depends heavily on duration of occlusion, collateral flow, and size of the initial myocardium at risk (Carlsson et al., 2009). After STEMI, myocardial water content is retained within the myocardial tissue due to damage tissue causing swelling in the affected area of myocardial and it is known as edema or area at risk. The STEMI is treated with reperfusion therapy as soon as possible. The area at risk is an important measure since a variable amount of this area will become infarcted (death heart tissues).

Two methods are used to assess the effectiveness of post STEMI therapy where can be salvaged. These are: (i) physiological study such wall motion analysis, or (ii) pathological study which is measuring the final edema area in relation to the initial edema area from the CMR image.

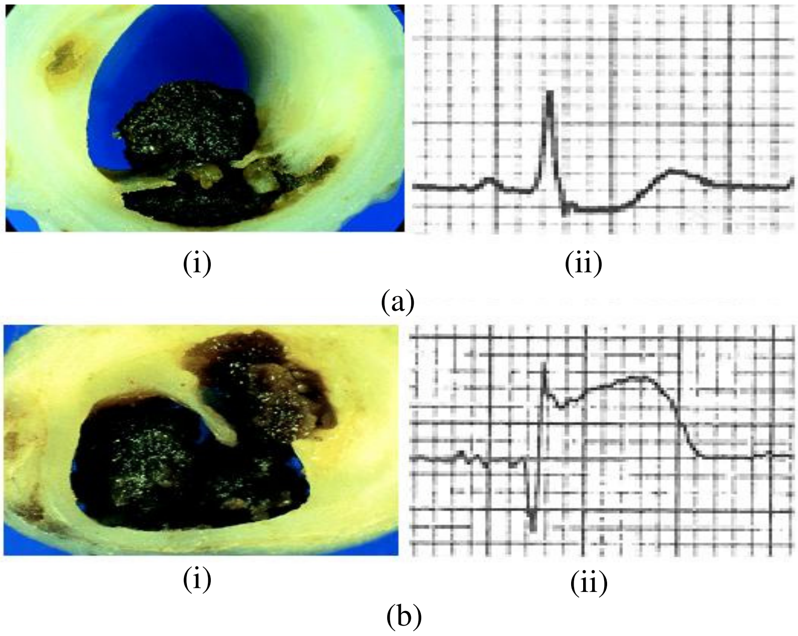

Figure 2.5: (a) NST elevation of MI, (i) partial blockage of artery, (ii) corresponding ECG signal; (b) ST elevation of MI, (ii) total blockage of artery, (ii) corresponding ECG signal (courtesy of Golden Jubilee Hospital, Glasgow)

2.4.3 Congestive heart failure (CHF)

Congestive heart failure (CHF) is a serious medical condition which occurs when the heart's pump function is inadequate to supply oxygen rich blood to the body. As the pump become less effective, more blood remains in the ventricle at the end of each cycle. This ultimately results in heart failure (G. J. Tortora and Derrickson, 2005).

Two types of CHF (Bales and Sorrentino, 1997) are:

- Systolic heart failure which is the most common type. It occurs when the heart muscle does not contract with enough force, so there is not enough oxygen-rich blood to be pumped throughout the body.
- Diastolic heart failure which occurs when the heart contracts normally, but the ventricle does not relax properly. So, less blood can enter the heart.

2.5 Magnetic Resonance (MR) Imaging

Magnetic Resonance (MR) Imaging or Nuclear Magnetic Resonance Imaging (NMR) is a non invasive imaging technique used to visualize the internal organs, soft tissues, bone and all other internal body structures. The advantages of MR imaging compare to other modalities are: (i) high resolution for anatomic structure, (ii) high contrast between different soft tissues, and (iii) no exposure to radiation and hence safe. A typical MR scanner is shown in Figure 2.6.

The basic idea of MR imaging is that it uses a powerful magnetic field to align magnetization of certain atoms in the human body and then uses radio frequency fields to systematically alter the alignment of this magnetization. This causes the nuclei to produce a rotating magnetic field detectable by the scanner and this information is recorded to construct an image of the scanned area of the body.

Figure 2.6: MR Imaging Machine (Mrc Cognition and Brain Sciences Unit, 2008)

In this section we summarize how an MR image is generated and the physics behind. The basic cardiac MR scan used within this PhD is also discussed. For a detailed description of the methodology on MR, the reader is referred to (Dominik Weishaupt et al., 2006, Z P Liang and Lauterburgh, 2000), and (Jerry L. Prince and Links, 2006)

2.5.1 Basic principle of MR imaging

The basic principle of MR is based on the interaction of a magnetic field and a nucleus that possesses spin. Medical MR imaging uses the signal from the nuclei of hydrogen atoms (1H) for image generation. This is due to the abundance of hydrogen atoms (1H) in the human body which is composed of tissues that contain water and fat, both of which contain hydrogen atoms (1H).

The characteristic of the hydrogen atom is that it has an angular momentum or spin due to the presence of only one proton. Any electrically charged particle which moves induces a magnetic field around it called a magnetic moment or net magnetization vector (NMV). Similar to the precession of a spinning top in the presence of a gravitational field, in the presence of a magnetic field, each magnetization moment vector precesses around the magnetic field with a frequency given by the Larmor equation (Hornak, 1996) :

$$\omega = \beta_0 \gamma \qquad 2\text{-}1$$

where ω is the resonance frequency, β_0 is the magnetic field strength in tesla (T), γ is gyromagnetic constant which is specific to a particular nucleus, The gyromagnetic ratio of a hydrogen atom is 42.57Mhz (Jerry L. Prince and Links, 2006). Figure 2.7 shows that in the absence of an external magnetic field, the spin orientations of the nuclei are random and cancel each other and the vector sum of all the microscopic magnetic moment in a given region, or the net macroscopic magnetization M, is zero. Once exposed to a strong external magnetic field B_0, the spins align parallel to the magnetic field B_0 which is shown in Figure 2.8(a). However, MR imaging systems are unable to directly detect the magnetization along the z-axis: they can only detect magnetization changes in the x-y plane (also known as the transverse plane). The RF excitation field B1 is used to tip the spins into the x-y plane so that they can be measured. This field is applied in a direction perpendicular to the main magnetic field (rotating in the x-y plane) as shown in Figure 2.8(b) and has a much smaller magnitude than B_0. The application of this rotating magnetic field is often called excitation. The angle α (in radians) at which the spins are tipped away from the z-axis and into the x-y plane is often referred to as the “flip angle”. The M now has two components, the transverse magnetization component M_{xy} and the longitudinal magnetization component M_z.

A receiver coil is situated in the transverse plane and as the rapidly rotating transverse magnetization M_{xy} creates a radio frequency excitation within the sample inducing a voltage in it according to Faraday’s law of induction. This signal is collected and processed with sensitive receivers and computers to generate the MR image.

Once an RF pulse is removed, the energy starts to decrease because the NMV tries to realign with B_0. As a result the amplitude of the MR signal will gradually decrease and is termed free induction decay (FID)

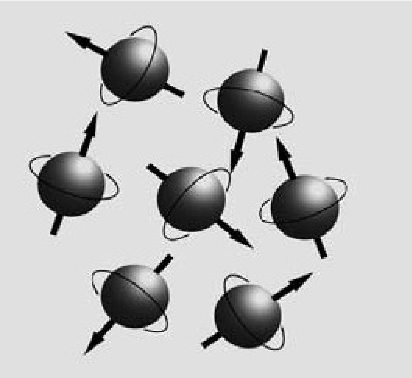

Figure 2.7: With no external Magnetic Field present, nuclei rotate about their axes in random direction, (D. Weishaupt et al., 2007)

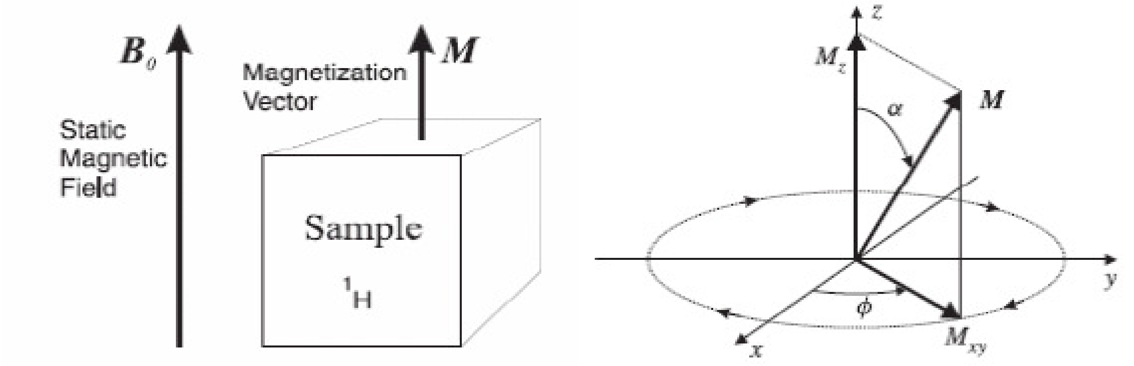

(a) (b)

Figure 2.8: (a) The Magnetization Vector *M*, (b) The Magnetization *M* precesses about the z-axis (Jerry L. Prince and Links, 2006)

2.5.2 MR imaging parameters

Many parameters are used in describing MR image generation. Some of the most common are the strength of the magnetic field and the Lamor frequency which are mentioned in section 2.5.1 previously. The other common parameters used are the relaxation time (T_1, T_2), the repetition time (TR), and the echo time (TE).

As explained in section 2.5.1 when RF pulses are applied it will result in nuclear magnetization (M) to split into two components, the transverse magnetization component (M_{xy}) and the longitudinal magnetization component (M_z). After the removal of RF pulse, the energy of NMZ decreases. The process is called relaxation.

Relaxation causes the loss of phase coherence in the transverse plane which is called transverse relaxation time T_2 and the exponential recovery of longitudinal magnetization which is called longitudinal relaxation time T_1. These two components are then used to construct the MRI images (Najarian and Splinter, 2006).

Figure 2.9 shows a single pulse of MR imaging sequence. The repetition time (TR) is the time from the application of one RF pulse to the application of the next RF pulse, measured in milliseconds (ms). It determines the amount of T_1 recovery time that will occur. The echo time (TE) is the time from the application of the RF pulse to the peak of the signal induced in the coil and is measured in ms. TE controls the amount of T_2 decay that will occur.

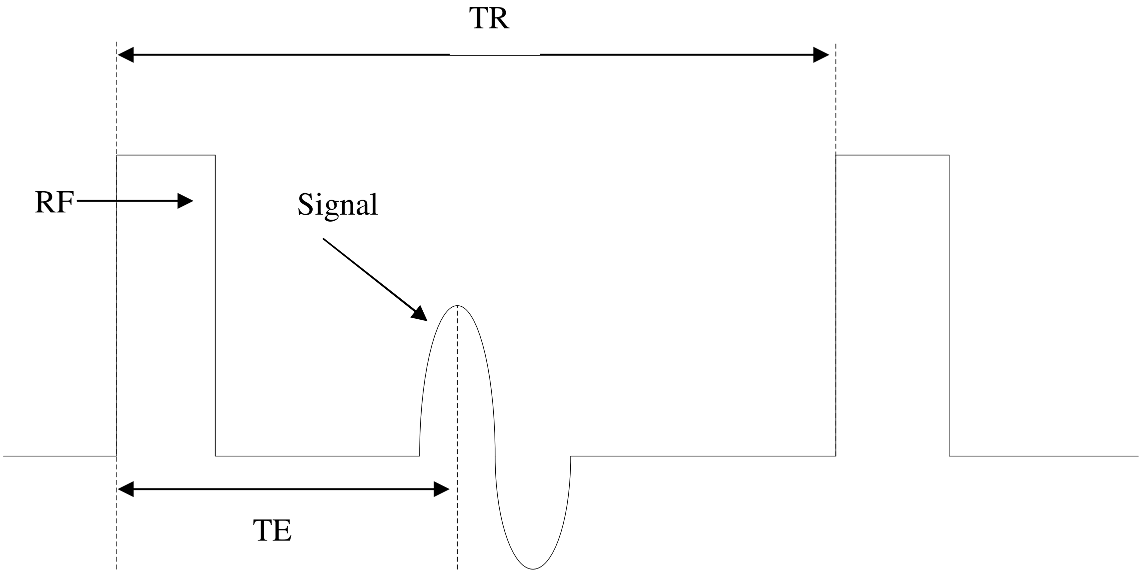

Figure 2.9: Single Pulse Sequence of MR Imaging

In T_1-weighted images tissues with short T_1 recovery time such as fat are bright. This is because they recover most of their longitudinal magnetization during TR, more magnetization is available in order to allow them to flipped into the transverse plane by the next RF pulse, by contrast in T_2-weighted images tissues with long T_2 decay time such as water appear bright. This is due to the ability to retain most of their transverse coherence during the TE period. Table 2-1 shows typical brightness of some tissues in different types of MR imaging.

Table 2-1: Brightness of typical Tissues in different MR Images (Hesselink, 2003)

Image types / Tissue	T_1-weighted	T_2-weighted
Fat	Bright	Dark
Cyst	Dark	Bright
White matter	Bright	Grey
Gray matter	Grey	Bright
CSF	Dark	Bright

2.5.3 K-Space analysis of MR imaging

In analyzing MRI data, the envelope of the normalized complex FID signal in the rotating frame can be written as:

$$s(t) = sk(k_x(t), k_y(t)) = \int_{-\infty}^{\infty}\int_{-\infty}^{\infty} \rho(x,y) e^{-j[k_x(t)+k_y(t)]} dxdy, \qquad 2\text{-}2$$

where *sk* is the envelope in k space, ρ(x,y) is the spin density and $k_x(t)$ and $k_y(t)$ are given by:

$$k_x(t) = \int_0^t \gamma G_x(\tau)d\tau \text{ and } k_y(t) = \int_0^t \gamma G_y(\tau)d\tau \qquad 2\text{-}3$$

where $G_{(x)}$ and $G_{(y)}$ are spatially varying gradient fields. Thus the signal received is the two-dimensional Fourier Transform of the spin density with frequency variables $k_x(t)$ value corresponds to a different complex time point in the readout direction and $k_y(t)$ value corresponds to a different phase-encoding gradient amplitude. For example, if a constant gradient magnetic field $G_{(x)}$ is applied for τ1 second following the RF pulse and a constant gradient magnetic field $G_{(y)}$ is applied for τ2 second the corresponding position in k-space would be ($k_x = \gamma G_x \tau 1, k_y = \gamma G_y \tau 2$).

Figure 2.10 shows a k-space plane, the magnetic field gradient is applied such that the k-space is filled in a rectangular fashion, thus allowing the inverse Fourier

Transform to be directly applied on the collected k-space data for image reconstruction.

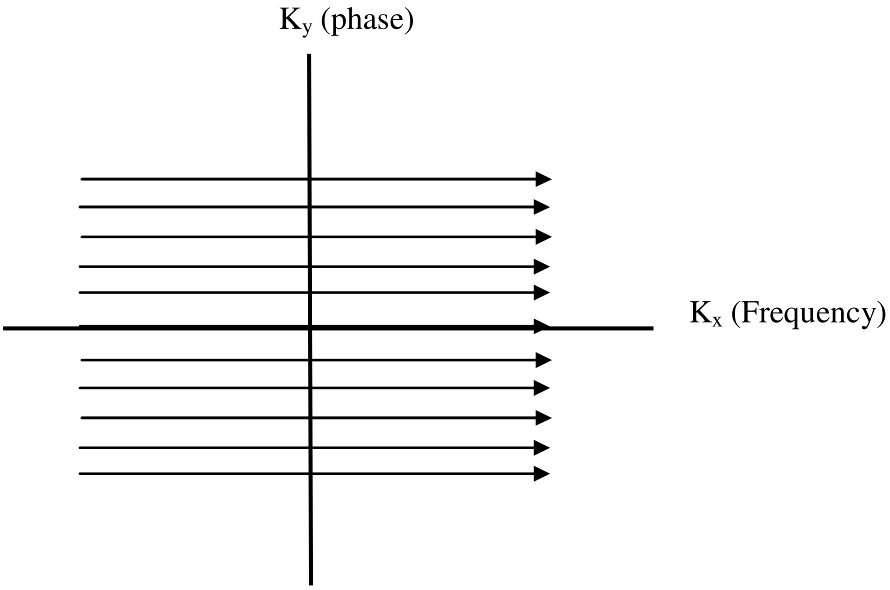

Figure 2.10: K-space. k_x is the frequency axis, k_y the phase axis. The data from each measurement fills a different horizontal line

2.5.4 Conventional MR sequence

Spin echo pulse sequence which is shown in Figure 2.11 is one of the basic pulse sequences used in MR imaging. The pulse sequence begins with the simultaneous application of a slice selection gradient and a 90° RF excitation pulse, which flips the net magnetization in the selected slice onto the xy-plane. Next the phase encoding gradient are applied to give the net magnetization precession and a phase proportional to its x and y directions respectively. The incremental signal induced in the receiver coil at this point, however rapidly decays with an exponential envelope. This decay is called T_2^* (T_2-star) and is caused by a destructive interference between the magnetic dipoles in the slice due to loss of phase coherence. This decay can be recovered somewhat by reversing the precession direction with a 180° RF pulse, called the echo pulse. The interval between the 90° and the 180° RF pulse is called the echo time. The echo signal is sampled and stored.

The raw data for an MR image is acquired by repeating the pulse sequence for several phase encoding levels. The time interval between consecutive 90° pulses is called the repetition time, T_R. The arrangement of the sampled echo signals line by line per phase encoding can be expressed as the 2D discrete Fourier transform (DFT) matrix of the final MR image. Therefore by taking the inverse 2D DFT of the arranged samples of the echo signals, an MR image is generated.

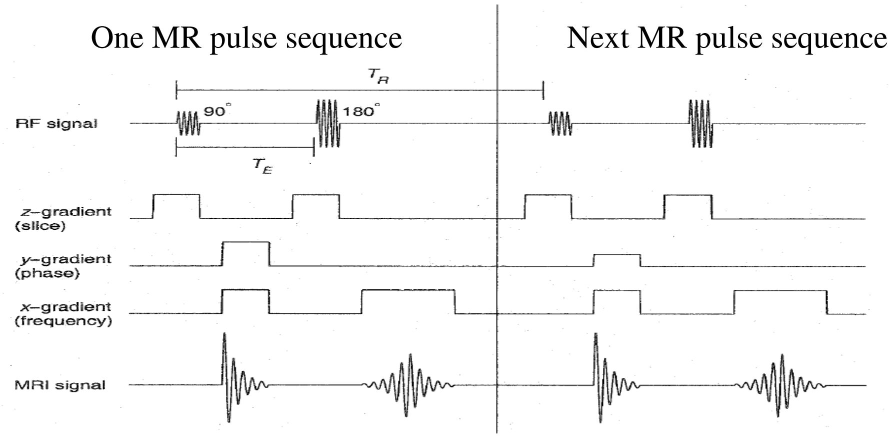

Figure 2.11: Spin Echo MR Pulse Sequence (Charncai Pluempitiwiriyawej, 2003)

Thus the reconstruction of MR image for a flip angle α, the MR intensity $I(x,y)$ is given by (Zhi-Pei Liang and Lauterbur, 2000):

$$\mathrm{I(x,y)=M}_0(x,y)\sin\alpha e^{-\frac{TE}{T_2(x,y)}}\left[1+(\cos\alpha-1)e^{\frac{TR}{T_1(x,y)}}\right] \qquad \text{2-4}$$

where $M_0(x, y)$ is the spatial proton distribution in the sample, $T_1(x,y)$ and $T_2(x,y)$ are the relaxation parameters of the sample, and T_E and T_R is the imaging times, therefore by manipulating the pulse sequence parameters; T_E and T_R. The contrast of the image can be adjusted.

2.5.5 Magnetic resonance imaging instrumentation

The instrumentation involved in acquiring MR images is discussed in this section. Figure 2.12 shows a typical schematic diagram of a MR machine. The system consists of four major subsystems a magnet, gradient system, RF electronic system and a computer system.

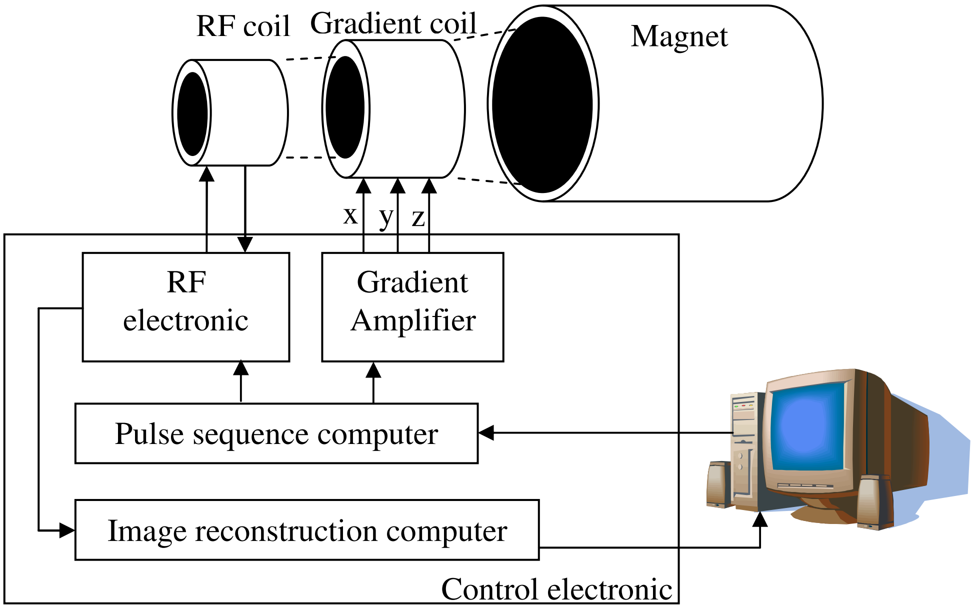

Figure 2.12: Block diagram of MR IMAGE Scanner

2.5.5.1 MR imaging magnet

The most important component of a MR system is the Magnet, which creates the main static magnetic field require for acquiring the image. The magnet is constructed in order to allow positioning of the patient inside the main static field. There are three types of magnet available. These are the permanent magnet, the resistive magnet and the superconductor magnet. The key requirements in selecting a magnet are field strength, field homogeneity, cost of maintenance and patient access.

The permanent magnet design is suited for low field applications because the highest field that can be generated by a permanent magnet is less than 0.3T which make it less advantageous. Although the field from the permanent magnet is low the advantages of permanent magnets are it is economic to operate and they greatly reduce interaction with the environment.

Resistive magnet design uses a current loop through a metal wire to create a static magnetic field. Due to the passing of current, the resistive magnet design tends to heat up and it needs a cooling scheme to cool the system. Because of the heat constraint the resistive magnet design can generate a field strength of up to 0.3T.

Superconducting magnet designs use the phenomenon of superconductivity where the resistance drops to approximately zero when it is cooled to a temperature close to absolute zero(-273°C). Currently the type of superconducting material used for MR imaging is niobium-titanium alloy because of its ability to support high magnetic field strength. The principal advantages of superconducting magnets are high field strength, reliability and stability.

2.5.5.2 Gradient coil system

The key to MR imaging is the ability of a gradient coil system to provide temporary change in magnitude of the main magnetic field B_O as a function of position. This temporary change of B_O provides the means to choose image slices and also provides the means to spatially encode the pixels within a given image (Hornak, 1996).

In a typical configuration three orthogonal gradient coils are used, one for each direction x-direction, y-direction and z-direction. In a process to acquire an image the three gradient coils are turned on and turned off. The purpose is to add or subtract a spatially dependent magnetic field to the B_O for the creation of MR image.

2.5.5.3 RF coils

The function of RF coils is to create the B_1 field which rotates the net magnetization in the pulse sequence during the transmission mode and then detects the transverse magnetization as it precesses in the xy-plane in the receive mode. There are two basic types of RF coils; volume coils and surface coils with typical operating frequency range from 1 to 170MHz for both. Volume coils are designed to surround the object being image and the surface coils are designed to be place near to the object being image. The volume coils are preferred to the surface coils because their field sensitivity patterns are very uniform which means that the transmitted energy is uniformly distributed throughout the object being image.

2.5.5.4 Scanning console and computer

The function of the console as shown in Figure 2.12 is to select imaging sequence and parameter such as scanning protocol, set the gating to the patient ECG or breathing in order to synchronous the MR acquisition to the appropriate periodic physiology process. The console is also used to select orientation plane of the scan image, review image obtained and change the variable in the pulse sequence to modify the contrast between tissues. Present scanners can reconstruct 10 to 50 images per second which is sufficient for real time scanning slice.

2.6 Cardiac MR Imaging and Diagnostic

Cardiac MR is an MR imaging technique used specifically for non-invasive assessment of the structure and the function of cardiovascular system. With the advantage of MR imaging in showing detailed images of heart muscles and how the blood moves through certain organs and blood vessels, allowing problems, such as blockages, to be identified. Thus allow physicians to better evaluate various cardiac ailments.

This section describes various types of cardiac imaging methods and common diagnostic testing carried out using MR imaging.

2.6.1 Cardiac MR imaging

Figure 2.13 shows a typical CMR image. First a Long axis view is acquired for the planning to acquire the short axis view as shown in Figure 2.13(a). Typically nine to twelve slices of SA images from basal to apical are acquired depending on the types of assessment performed. Figure 2.13(b-d) shows three slices acquired from a single patient correspond to basal, middle and apical slice.

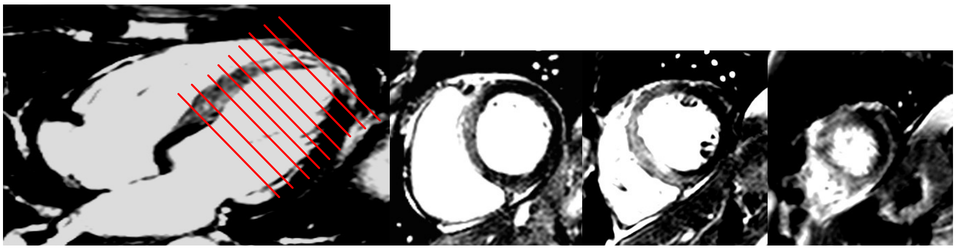
(a) (b) (c) (d)

Figure 2.13 : (a) Long Axis (LA) view and planning of Short Axis (SA) images, (b) Basal slice, (c) Middle slice, and (d) Apical slice (courtesy of Golden Jubilee National Hospital, Glasgow)

Three types of CMR images are commonly used Cine CMR, Late enhance CMR and T_2-weighted CMR. A Cine CMR image shown in Figure 2.14(a) is used to study functionality of the heart, usually the CMR images are taken over a period of time from the end of the diastolic cycle to the end of the systolic cycle. These images are acquired to investigate the whole heart volume. Some of the assessments that can be performed using Cine CMR are ejection fraction, systolic wall thickening and wall motion analysis (Frangi et al., 2001). The Late enhance CMR and T_2-weighted CMR shown in Figure 2.14(b) and Figure 2.14(c) are used to the study the LV wall structure. In both image sequences a single image is acquired for every slice from the basal slice to the apical slice. In Late enhance (LE) image a contrast agent normally gadolinium solution is administered to the patient and after a period of time the image is then acquired. Normal heart muscles appear dark, while the damage area will appear bright white as shown in Figure 2.14(b). In a T_2-weighted image shown in Figure 2.14(c) the same image characteristic can be observed where normal wall area will appear dark compare to the damage area which is known as edema region. The advantage of T_2-weighted method is that there is no contrast agent thus the image can be acquired much faster.

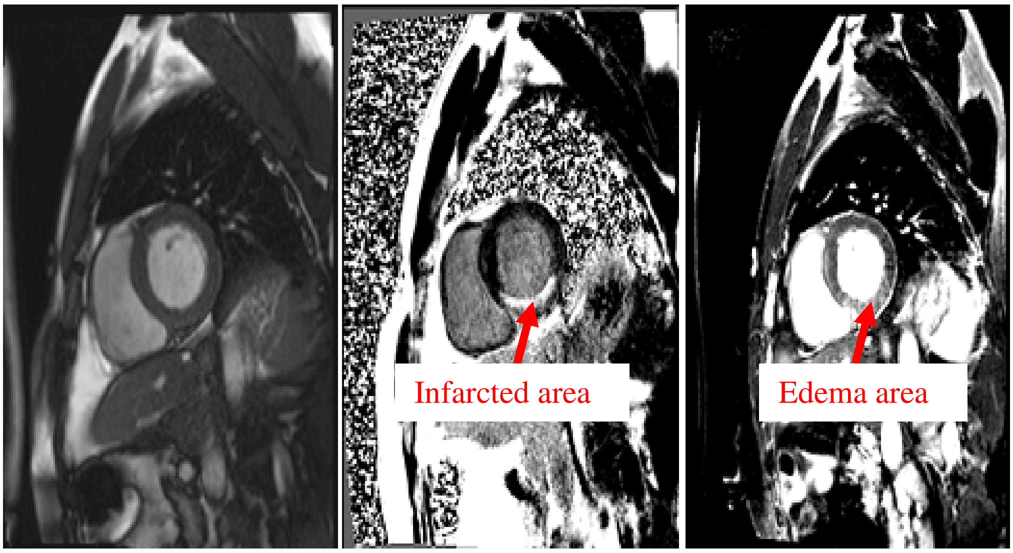

(a) (b) (c)

Figure 2.14: SA view of (a) Cine Image, (b) Late Enhance Image, and (c) T_2-Weighted Image (courtesy of Golden Jubilee National Hospital, Glasgow)

2.6.2 Cardiac diagnostic

As mentioned in the previous section the main intention of MR imaging is to diagnose the condition of the heart. Depending on the nature of CMR image being acquired, two types of diagnosis can be performed by the clinician. The studies are i) the study of physiological functions of the heart and ii) the study of the pathological structure of the wall.

2.6.2.1 Physiological function of LV wall

Wall Motion analysis is one of the clinical techniques used by physicians to study the condition of the heart. As the heart is a moving organ, the condition of the heart can be investigated by looking into the motion of the heart over a complete cardiac cycle from the end of the diastole to the end of the systole. These wall motion changes may represent ischemia or infarction of myocardium. Quantifying the extent of regional wall motion abnormality may aid in determining the myocardial effects of coronary artery disease (Gelberg et al., 1979).

Another form of study that can be performed to investigate functionality of the heart is the wall thickening analysis. Lieberman et al (Lieberman et al., 1981) demonstrated in a study using a dog model of acute infarction that there was evidence of an abrupt deterioration of systolic wall thickening in segments with more than 20% transmural extent of infarction. In another study, involving patients with perfused chronic infarcts, Mahrholdt et al (Mahrholdt et al., 2003) determined that systolic wall thickening was diminished in segments containing more than 50% nonviable myocardium. These studies proved that wall thickness analysis is a reliable indicator to analyzing abnormality of the heart.

The above discussion is not exhaustive. There are many other types of study that can be done to analyze the functionality of the heart and details of these can be found in (Frangi et al., 2001).

2.6.2.2 Pathological study of LV wall

In pathological studies of LV wall rather than looking into how the heart functions over a period of time, we are interested to look at the actual myocardial scar in patients with chronic ischemic heart disease. This can be achieved using either LE images or T_2-weighted images.

LE is an imaging modality capable of high spatial resolution and able to assess the presence of viable myocardium in infarcted and poor contractile areas (Kim et al., 1999). In another study Kim et al (Kim et al., 2000) shows, in the chronic phase of MI, LE image has been shown to correlate well with fibrosis and be a marker of irreversible injury.

In T_2-weighted images several studies have demonstrated that these images can be used to delineate the ischemic AAR and myocardial salvage in patients with recent acute MI (Kellman et al., 2007, Berry et al., 2010). The advantage of T_2-weighted images when compared to LE images are that in T_2-weighted images there is no contrast agent being used thus the acquisition can be done instantly, whereas in LE images some delay is expected due to the time taken for the contrast agent to flow through the heart wall. In T_2-weighted images the hyperenhanced region is known as myocardial edema (Abdel-Aty et al., 2009). Myocardial edema is due to fluid accumulation following myocardial injury, such as ischaemia or inflammation, and the quantification of edema is an important step in distinguishing between viable and non viable myocardial tissue. This is an important consideration for risk assessment and treatment decisions making (Van De Werf et al., 2008)

2.7 MR Image Artefacts

MR image artefacts in MR images are produced by various complications of the imaging process, which results in an image that does not portray an accurate representation of a slice of tissue (Savoy and Jovicich, 2001) and can result in inaccurate diagnosis.

MR artefacts can be classified into two general categories. 1) Hardware related artefacts which are uncommon and difficult to diagnose that usually require service personnel to correct and 2) artefacts related to the patient or under operator control. This category is encountered much more commonly and may be easily prevented or corrected once they are recognized. Examples of sources of these artefacts are motion artefact, chemical shift artefact, aliasing, RF inhomogeneity, Gibbs or truncation artefact, and partial volume artefact (Hornak, 1996).

2.7.1 Motion artefacts

Motion is the most prevalent source of MR imaging artefacts (Smith and Nayak, 2010). As the name implies, motion artefacts are caused by motion of the imaged object or a part of the imaged object during the imaging sequence. The motion artefacts are observed along the phase-encoding direction of the image result with blurring of the image with ghost images as shown in Figure 2.15(a). The voluntary motion of the patient can usually be prevented, but cardiac motion, respiratory motion, vascular pulsation, and etc cannot be eliminated. In the case of cardiac motion, it produces a series of ghost artefacts along the phase-encoding direction of the MR image. The solution for reducing cardiac motion artefacts is electrocardiographic triggering, in which data collection is synchronized with cardiac phase as shown in Figure 2.15(b). This synchronization enables cardiac tissue to be located in a consistent position as each successive phase-encoding step is acquired, resulting in increased tissue signal intensity and decreased phase errors. Other approaches include the use of fast imaging sequences that reduce the opportunity for motion during data acquisition.

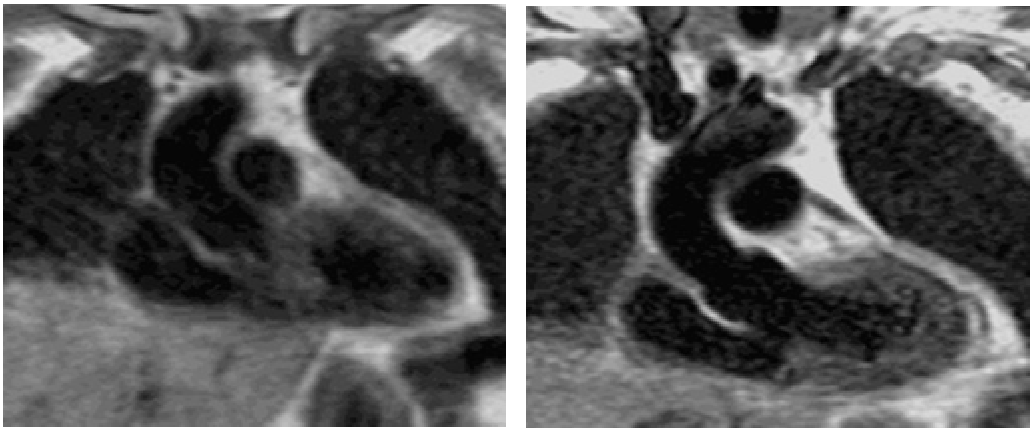

(a) (b)

Figure 2.15: (a) Image without Motion Compensation Technique, (b) Image with Cardiac Gating(Ruan, 2003).

2.7.2 Chemical shift artefact

The chemical shift artefact (Ballinger, 1996) is due to misregistration of relative positions of two tissues with different Larmor frequencies. Most common chemical shift is the misregistration of fat and water which is then transformed into spatial difference as shown in Figure 2.16 the arrow shows the location of the chemical shift artefact which shows an appearance of a dark rim at one edge of the object.

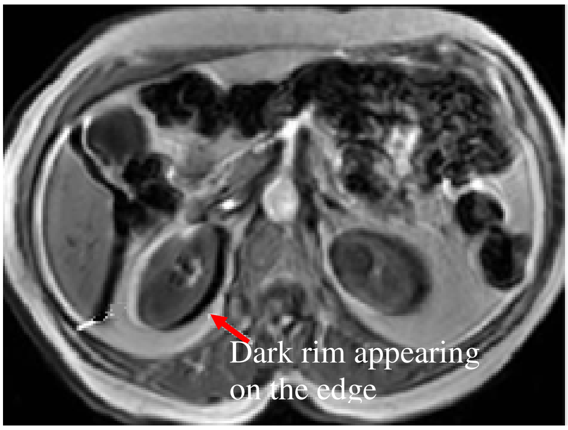

Figure 2.16: Chemical Shift Artefact (Richard Bitar, 2006)

Chemical shift artefact can be reduced by performing imaging at low magnetic field strength, by increasing receiver bandwidth, or by decreasing voxel size. The artefacts tend to be more prominent on T_2-weighted than on T_1-weighted images. Fat suppression methods often eliminate visible artefacts, and gradient reorientation can redirect chemical shift artefacts to another portion of the image.

2.7.3 Aliasing artefact

Aliasing artefact is a common artefact when the field of view (FOV) is smaller than the body part being imaged causing the region beyond to project on the other side of the image as shown in Figure 2.17, where the aliasing occurs at the back of the head and on the front of the head. The solution to a wrap around artefact is to choose a larger field of view, adjust the position of the image centre, or select an imaging coil which will not excite or detect spins from tissues outside of the desired field of view.

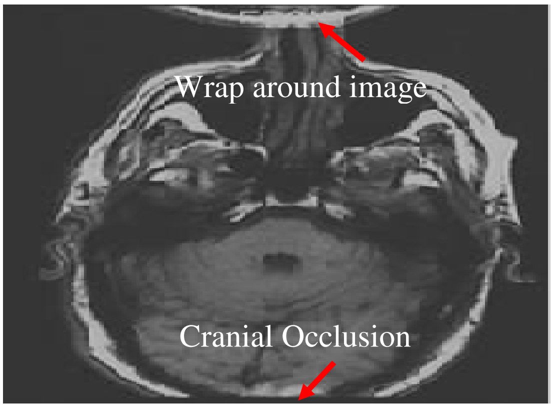

Figure 2.17: Aliasing Artefact (Ballinger, 1996)

2.7.4 RF inhomogeneity

An RF inhomogeneity artefact is due to the presence of an undesired variation in signal intensity across an image and also due to non-uniform fat suppression. Figure 2.18 shows an image from a surface coil with its characteristic intensity decreasing as the relative distance of the patient increases away from the coil. In some RF coils such as surface coils have a natural variation in sensitivity and will always display this artefact. The presence of this artefact in other coils represents the failure of an element in the RF coil or the presence of metal in the imaged object. The RF inhomogeneity can be reduced by using superconducting magnet which produces homogenous magnetic field over time.

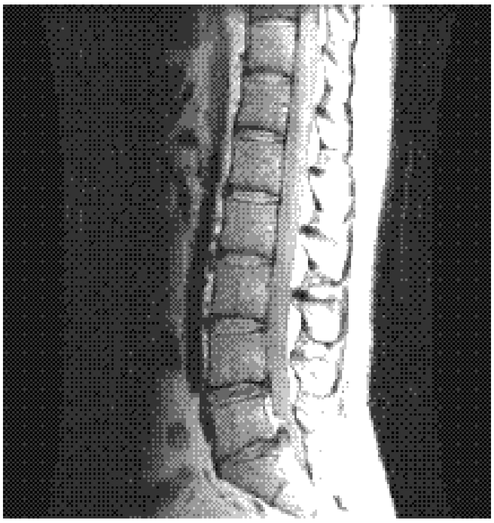

Figure 2.18: RF Inhomogeneity (Hornak, 1996)

2.7.5 Gibbs ringing artefact

Gibbs ringing artefact (Ruan, 2003) is the result of under sampling of the data so that the interface of high and low signal is incorrectly represented on the image. The artefact results in parallel dark or bright lines appearing next to borders of abrupt intensity change. Ballinger (Ballinger, 1996) describes three methods that can be used to reduce the artefacts namely: (i) increase the resolution of the imaging matrix, (ii) lessen the intensity and (iii) narrow the artefact. Figure 2.19(a) shows fine lines appearing on the image as indicated by the arrows, which is due to undersampling of the high spatial frequency. The solution to this problem is to increase the number of samples of the image as shown in Figure 2.19(b)

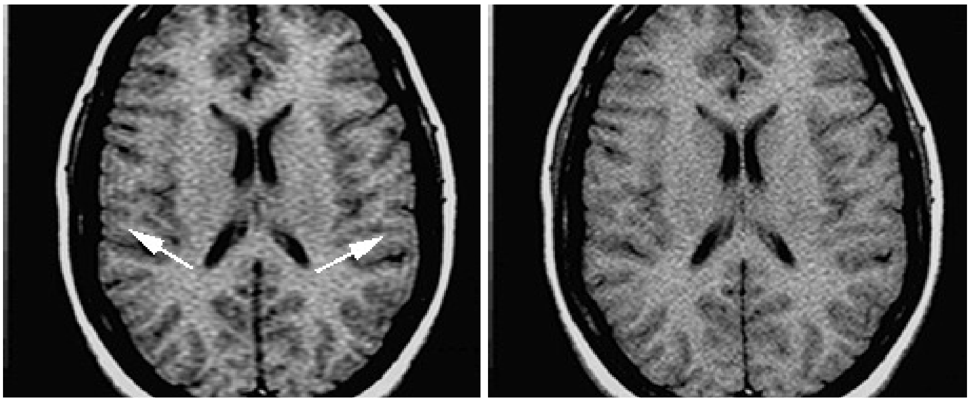

(a) (b)

Figure 2.19: (a) Gibbs Ringing appearing as fine lines, (b) MR Image with 256 phase encodes (Ruan, 2003)

2.7.6 Partial volume artefact

Partial volume artefact (Hornak, 1996) is described as any artefact that occurs when the size of the image voxel is larger than the size of the feature to be imaged. For example, if a small voxel contains only fat or water signal, and a larger voxel might contain a combination of the two, the large voxel possesses signal intensity equal to the weighted average of the quantity of the two tissues in the voxel. This is manifested as a loss of resolution caused by multiple features present in the image voxel. Figure 2.20 shows a comparison of two axial slices through the same location of the head. One is taken with a 3 mm slice thickness and the other with a 10 mm thickness. In Figure 2.20(b) the loss or resolution is obvious and the details of some structure disappear compared to Figure 2.20(a).

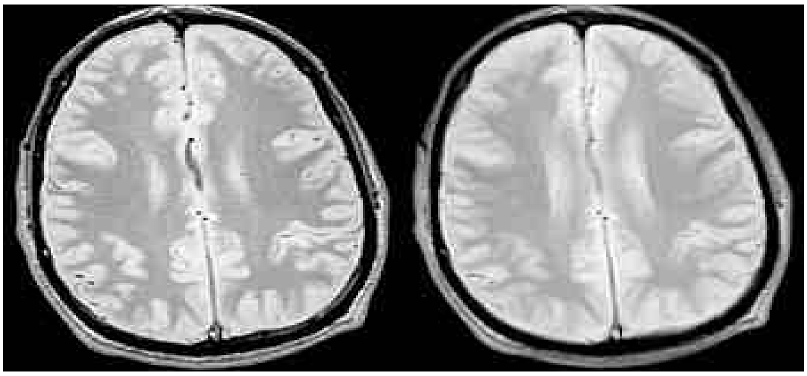

(a) (b)

Figure 2.20: Resolution comparison (a) 3mm slice thickness, (b) 10mm slice thickness(Alanallur, 2009)

2.8 Conclusion

This chapter has reviewed cardiovascular disease which is a major cause of death in the modern world. To understand the disease the anatomy and physiology of the heart along with the common heart conditions were described.

The chapter also discusses the MR imaging technology and types of CMR images being used by the clinician for non-invasive assessment of the structure and the function of the cardiovascular system, including the principles of magnetic resonance, the MR instrumentation, image acquisition and reconstruction, the views that that are widely used and some MR image artefacts. A T_2 weighted CMR image with short axis view is used in this research because of the advantage of using T_2 weighted CMR image to assess the structure of the heart wall.

The research included in this thesis involves the segmentation, quantification and 3D visualization of edema from the LV CMR images. Thus in the following chapters, various image processing techniques applied to CMR images to solve this problem and to develop a semi or fully automatic algorithm for edema quantification with 3D Visualization is presented.

CHAPTER 3

3. DIGITAL IMAGE PROCESSING IN CARDIAC MAGNETIC RESONANCE (CMR) IMAGING

3.1 Introduction

The previous chapter reviewed the fundamentals of the anatomy and physiological of a human heart. Then the technology behind MR imaging was discussed, including principle of MR imaging, MR instrumentation, Cardiac MR imaging and finally some MR imaging artefact.

The purpose of this chapter is to give an overview of general technique for MR image processing system. Figure 3.1 shows a general block of a typical MR image processing system. Generally MR data processing can be divided into two parts. Part one is the fundamental block in all automatic MR imaging systems which consist of i) Image pre-processing and LV localization and ii) LV wall segmentation, where the stack of CMR images is processed to delineate the LV wall region from the rest of the images. Part two is specific to the research problem of this thesis namely; i) Edema Segmentation and Quantification in which the result from the LV wall region is used for the segmentation and quantification of edema and ii) 3-D reconstruction and visualization, where the output of the previous two processes are used to reconstruct the SA axis images into 3-D which illustrates edema region and normal region.

This chapter is structured as follows: Section 3.2 presents image pre-processing techniques and LV localization techniques. In 3.3, a discussion on the state of the art in LV wall segmentations is presented. In section 3.4, current methods in edema segmentation and quantification techniques for CMR images are discussed. Section 3.5 presents the 3-D reconstruction techniques from 2-D images to 3-D models. Finally section 3.6 concludes the chapter.

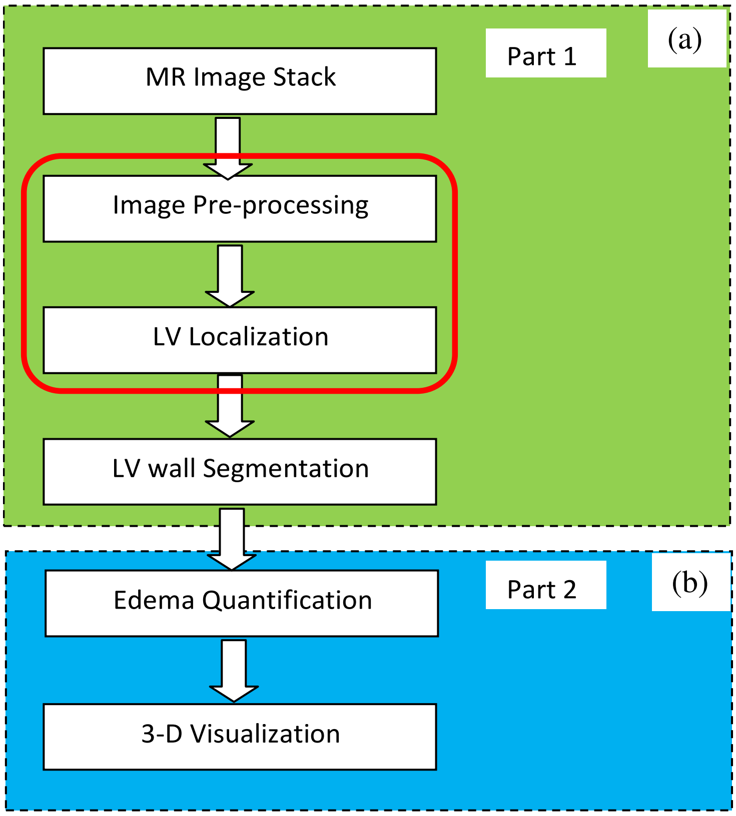

Figure 3.1: (a) General block diagram of MR Imaging Algorithm, (b) Edema segmentation and 3D Visualization Algorithm

3.2 Overview of Image pre-processing and LV wall localization methods

The segmentation of the LV wall requires several preliminary steps before any LV wall segmentation algorithm can be applied. In this section a review of image pre-processing techniques and LV wall localization are presented.

3.2.1 Image pre-processing methods

Image pre-processing is an important step before any LV wall segmentation because of the challenges of automatically segmenting the LV wall. The segmentation of LV wall consists in segmenting the endocardium and then segmenting the epicardium. Each process presents specific difficulties such as grey level inhomogeneities in the blood pool flow and the presence of papillary muscles and trabeculation (wall irregularity) inside the heart chamber for endocardium. In epicardium feature extraction the challenges are weak edges around the epicardium, and the fact that the presence of edema in the myocardial tissues for T_2-weighted image which has higher signal intensity and variations compared to normal myocardial tissue further complicated the segmentation process.

Due the challenges above in most LV wall segmentation algorithm a pre-processing is added into the process. The main image pre-processing methods applied to CMR data are based on non-linear filtering and morphological filtering as indicated in Table 3-1.

Table 3-1: Common image pre-processing methods used to pre-process CMR data

Technique	Author	Basic Principle
non-linear filtering	Santarelli et al., 1999 Santarelli et al., 2003 Lynch et al., 2006	Anisotropic filtering
	Ting et al., 2008	multistage median filtering
	(Yuwei et al., 2009)	selective smoothing diffusion filtering
Mathematical morphological filter	El Berbari et al., 2007	Connected opening and closing
	Cocosco et al., 2008	Combined Otsu thresholding with binary morphological operation

3.2.1.1 Anisotropic filtering

Anisotropic filtering is a non-linear filtering which concentrates on the preservation of important surface features like sharp edges and corners by applying direction dependent smoothing. Smoothing is formulated as a diffusive process, which is suppressed or stopped at boundaries by selecting locally adaptive diffusion strengths such as the statistic of noise degradation and the edge strength (Perona and Malik, 1990, Gerig et al., 1992). A direct implementation of anisotropic filtering has been presented in by (Santarelli et al., 2003, Lynch et al., 2006a, Santarelli et al., 1999). In Ting (Ting et al., 2008), a multistage median filtering is applied to suppress random noise with better edge preserving capability compared to median filtering. Yuwei (Yuwei et al., 2009) applied a selective smoothing diffusion as proposed by (F. Catté et al., 1992) to smooth the CMR image to improve the segmentation of the Directional Gradient Vector Field Snake (DGVF).

3.2.1.2 Morphological based filtering

Morphological based filtering is based on a form of set algebra known as mathematical morphology. Most morphological filters use extreme order statistics (minimum and maximum values) within a filter window (Maragos and Schafer, 1990) for image filtering. In El Berbari (El Berbari et al., 2007) a connected opening and closing is applied to CMR image, the objective being to produce an image that consists mostly of a flat image and a large region. Cocosco (Cocosco et al., 2008) combined Otsu thresholding with a binary morphological operation using a 4-neighbour connectivity kernel. A dilation process is repeated for “A”[1] times and largest connected component is identified and kept.

3.2.2 LV wall localization methods

LV wall localization is an important aspect in automatic LV wall segmentation. As indicated in Table 3-2 LV wall localization can generally be classified into two types: time based approaches which takes advantage of the fact that the heart is the only moving organ in the CMR image and object detection approaches, which uses spatial information from SA image to locate the location of the LV wall (Petitjean and Dacher, 2011).

---

[1] “ A “ is tunable parameter in the ROI computation method

Table 3-2: Common LV localization methods used to localize the LV

Technique	Author	Basic Principle
time based approach	Gering, 2003 Cocosco et al., 2004	3D+t image variance combined with convex hull
	Colantonio et al., 2005	a cluster based analysis (fuzzy c-means algorithm)
	Pednekar et al., 2006	Computation of motion analysis from two consecutive images combined with Hough transform
	Junzhou et al., 2007	Image difference combined with dynamic texture analysis and k-means clustering
	Jia et al., 2008	Intensity difference from two consecutive frames combined with Hough transform.
	Constantinides et al., 2010	Gray level variation over entire cardiac cycle combined with 3D labelling
	Hae-Yeoun et al., 2010	Image intensity difference combined with Hough transform
	Lin et al., 2006 Jolly, 2008	Fourier transform
object detection approaches	Jolly, 2006 Pavani et al., 2010	Learning based method. Optimization of Haar-like features by assigning optimal weights to its different Haar basis functions
	Lynch et al., 2006	Un-supervise classification using K-means algorithm combine with shape descriptor
	Kurkure et al., 2009	Combination of processing LA and SA and application of Otsu thresholding to identify binary component of the CMR image.

3.2.2.1 Timed based approaches

In time based approaches the difference or variance in image characteristic over cardiac cycles can be used to locate the LV region. The work by (Gering, 2003, Cocosco et al., 2004) uses variance computation where from a 3-D+t of the original image, variability along time dimension is measured using standard deviation of each voxel. Then the maximum intensity of the resulting 3-D image is projected on a 2-D image. The resulting 2-D image is subsequently binarized using Otsu's method and dilated several times. The convex hull of the obtained region is the final 2-D region-of-interest (ROI). Colantonio (Colantonio et al., 2005) used a cluster based analysis where fuzzy c-means algorithm is applied to indentify and label homogeneous region in each slice. Once the homogeneous regions have been classified they are then analysed over an entire cardiac cycle to determine the LV. In Pednekar (Pednekar et al., 2006) the difference of two consecutive images on a basal slice near the end diastolic (ED) is computed to construct a motion resulting in a circular region around the LV, which can then be detected by applying the Hough transform. Image difference is also used in (Junzhou et al., 2007) followed by dynamic texture analysis and k-means clustering to locate the heart region, Jiang (Jia et al., 2008) also used intensity difference from two consecutive frames and then by applying the Hough transform the LV is located, Constantinides (Constantinides et al., 2010) used the difference of every pixel scanned over a cardiac cycle with the assumption that gray level variation is more significant with pixel belonging to the heart due to heart motion. This is then combined with 3-D labelling to ensure spatial continuity.

In the work proposed by Hae-Yeoun (Hae-Yeoun et al., 2010) where a circular Hough transform is performed on the subtraction magnitude of images across the whole cardiac cycle on a mid ventricle slice. The seed is then propagated across the remaining slices and phases by examining 11x11 pixel windows whose centres are the centre of gravity of the segmented LV region of the previous image. Image based difference can suffer in noisy conditions. An alternative approach is to use a Fourier transform of the image sequence over time which can provide an image moving object (Lin et al., 2006, Jolly, 2008). The LV location is detected by computing the first harmonic of the Fourier transform on image sequence which allows for localizing of the heart (see Figure 3.2).

The disadvantage of the above methods is that they are only suitable for cine CMR images and not directly applicable to LE or T_2-weighted image because in these types of images the images are not acquired over the whole cardiac cycle.

Furthermore by processing consecutive image or the whole cardiac cycle will create heavy demand on the processor.

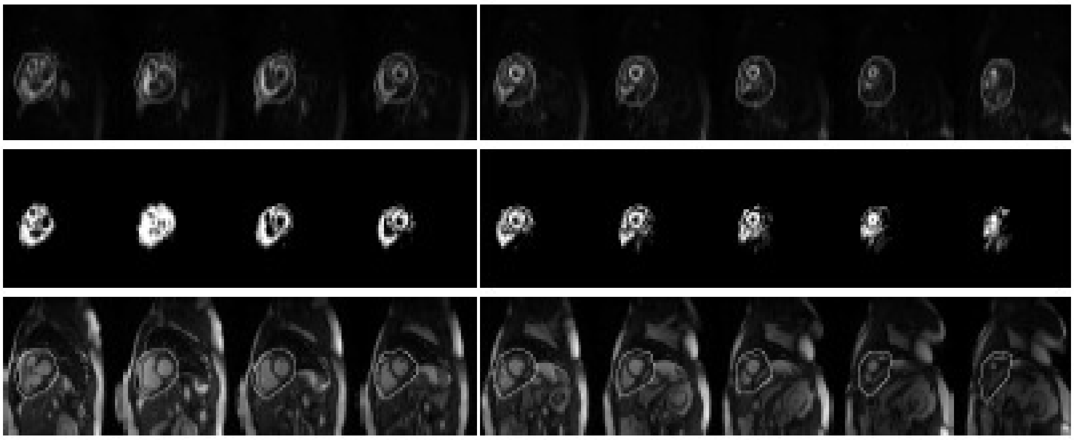

Figure 3.2: Automatic heart localization: first row: first harmonic of the Fourier transform with the region extracted after 3D line fitting and distant artefact removal; second row: white connected components were kept and gray ones were discarded; third row: region of interest localizing the heart (Jolly, 2008)

3.2.2.2 Object recognition approaches

Another approach in LV localization is based on object recognition utilising a learning based algorithm. The aims of learning based approaches are to extract rectangular sub-windows from the CMR image, and derive their features, to train the classifier to accept the LV and discard others anatomical structures. The global profile is based on maximum discrimination, where the system models feature vectors as Markov processes. Then the system is trained to minimize between positive and negative samples. In the detection each pixel is cluster into potential LV wall candidates and by using the Hough transform a voting based procedure on the individual profiles are created, which produce a circle representing the rough positioned of the LV (Jolly, 2006). Pavani (Pavani et al., 2010) proposed a method based on face detection approach (Viola and Jones, 2001), which uses Haar-like features (Papageorgiou et al., 1998). The aim is to optimise Haar-like features for a given object detection problem by assigning optimal weights to its rectangular windows. The optimal weight is determined by using a training dataset. As with any training based algorithm the accuracy of the method depends on the number of training dataset and as the dataset getting bigger, this increases the computational cost.

Unsupervised learning has also been used Lynch (Lynch et al., 2006a) where the image is clustered using a *k*-means algorithm then a shape descriptor is used with the assumption that the LV is a circular shape. Approximation of the circle is calculated as the error between the shape and the least square approximation of the circle. In Kurkure (Kurkure et al., 2009), the LV is localized by computing the projection lines from the long axis (LA) view and four chamber view to obtained intersection crosshair onto end diastolic (ED) SA image. Then extract the ROI and compute an 8-bit histogram of the ROI. An Otsu's based threshold is then applied to the ROI and the LV is located by identifying the binary component that is closest to the cross-hair

3.3 LV Wall Segmentation Methods

The LV boundary segmentation is performed to remove the rest of the anatomical structures from the LV wall of the CMR image. Once the LV wall has been segmented further investigation can be performed either for pathological study or physiological study. Research on the segmentation of the LV wall is an important field as the manual identification of the LV wall has significant intra-observer and inter-observer variability. LV wall segmentation methods can generally be categorized into pixel classification methods, deformable model based methods, statistical models methods, and atlas based methods (Pham et al., 2000, Petitjean and Dacher, 2011). Although each technique is described separately, multiple techniques are often employed together to obtain better solutions. In the rest of this section, we will discuss recent techniques used to segment the LV wall boundary.

3.3.1 Pixel classification based methods

In pixel classification methods images are partitioned into regions or classes, composed of pixels that have close feature values, using either supervised techniques (with learning samples) or unsupervised techniques as indicated in Table 3-3.

Table 3-3: Pixel classification based segmentation methods

		Author	Basic Principle
Pixel classification methods	Supervise classification method	(Stalidis et al., 2002)	Neural network combined with spatial-temporal technique
	unsupervised classification techniques	(Lynch et al., 2006a)	k-means algorithm with edge information is used to segment the LV and final segmentation is achieved by cubic-spline to close the LV wall contour
		(Van Assen et al., 2006)	Fuzzy c-means clustering. The CMR image is clustered into three clusters.
		(Gering, 2003)	EM + MRF
		(Pednekar et al., 2006)	EM embedded in cost matrix for dynamic programming
		(Lynch et al., 2007)	Iterative EM algorithm to find optimal number of seed

3.3.1.1 Supervised classification techniques

Supervised classification approaches such as maximum-likelihood and Bayes classifier methods are often used when training data is available. The algorithms require a tedious learning phase, which consists of providing the algorithm with gray levels of labelled pixels. The learning phase is often performed by manually segmenting sample data such as in Stalidis (Stalidis et al., 2002) where a few sample pixels belonging to myocardium, blood and lung are manually selected. Theses samples are provided to a generating-shrinking neural network, combined with a spatiotemporal parametric modelling. In this work, the LV wall boundary is found through a radial search, using the previously defined LV wall model. The weakness of the method is the training data which is often required to be manually segmented and the algorithm is not robust to intensity inhomogeneities (Xiang, 2008).

3.3.1.2 Unsupervised classification techniques

In unsupervised classification techniques images are clustered without the use of training data, which makes them easy to use in different image modalities. Three common algorithms are k-means, fuzzy c-means and expectation-maximisation (EM).

Lynch (Lynch et al., 2006a) proposed the use of adapted k-means algorithm to segment the CMR image into separate clusters. After separate cluster regions have been found, the LV cavity is recognized by computing the error between the shape and the approximation to the circle. Since the closest blood pool to the LV cavity is the right ventricle (RV), the wall between these two blood pools is measured, which guides the epicardium segmentation using edge information. Finally cubic-spline is used to close the epicardium contour. In the k-means algorithm hard thresholding is used to determine whether the pixel belongs to one cluster as compared to another cluster, but the problem with clustering human organs are the changes can sometime be more gradual. Thus to solve the problem of hard thresholding Van Assen (Van Assen et al., 2006), applied fuzzy c-means for clustering the CMR image into three clusters. Unlike k-means, fuzzy c-means allows partial class membership.

The Expectation-maximization (EM) algorithm (Dempster et al., 1977) is a general method to estimate unknown parameters from given information, which uses histogram distribution estimation for image classification. Gering (Gering, 2003) proposed the use of EM as an initial step before using Markov Random Field (MRF) to incorporate spatial correlation into the segmentation process. Pednekar (Pednekar et al., 2006) proposed that the EM algorithm result can be embedded into a cost matrix for dynamic programming. Lynch (Lynch et al., 2007) proposed the used of EM algorithm to segment the MR image. First the algorithm selects a large number of possible partitions, using peaks (local maxima) from the intensity histogram. Then using the EM algorithm iterative clustering is performed to these peaks, using their histogram heights and greyscale difference until the optimal number of seeds is reached.

3.3.2 Deformable model based methods

Deformable models are techniques for delineating region boundaries using 2-D closed parametric curves or 3D surfaces which deform under the influence of internal and external forces (Pham et al., 2000). External energy is constructed from a feature space or directly from the image to drive the curve or surface towards desired image features such as edges. Internal energy is the energy of the contour, such as motion curvature which maintains smoothness throughout the deformation.

3.3.2.1 Active contour

The active contour algorithm, also known as snakes was first introduced by Kass (Kass et al., 1988). The contour can be described by $v(s) = [x(s), y(s)]$ that moves through the spatial domain of an image through energy minimize function of:

$$E^{*}_{Snake} = \int_{0}^{1} E_{Snake}(V(s))\, ds = \int_{0}^{1} E_{\text{int}}(V(s)) + E_{image}(V(s))\, ds \qquad 3\text{-}1$$

where, E_{int} represents the internal energy of the contour with respect to elastic deformations and bending of the active contour. The internal energy is defined as:

$$E_{\text{int}} = \frac{(\alpha(s)|V_s(s)|^2 + \beta(s)|V_{ss}(s)|^2)}{2} \qquad 3\text{-}2$$

where α and β are the measure of the elasticity of the active contour and the stiffness of the active contour respectively. The image energy term E_{image} pulls the active contour towards features in the image such as the image intensity gradient (Kass et al., 1988):

$$E_{image} = w_{line}E_{line} + w_{edge}E_{edge} + w_{term}E_{term} \qquad 3\text{-}3$$

where

$$E_{line} = I(x, y), E_{edge} = -\left|\nabla I(x, y)\right|, E_{term} = \frac{d\theta}{d(-\sin\theta, \cos\theta)}$$

During the optimization process, the active contour is deformed with respect to the features to be localized.

Santarelli (Santarelli et al., 2003) applied a gradient vector flow (GVF) snake to segment the LV wall which improved the performance of the active contour because the traditional active contour suffers from two limitations; sensitivity of the initialisation curve that needs to be near the boundary, and difficulties in progressing into boundary concavity. In Jinsoo (Jinsoo et al., 2003) a new image force is used called tensor-based orientation gradient force, using three-directional velocity images from the phase contrast MR image. Hautvast (Hautvast et al., 2005) proposed the use of a contour propagation method based on an active contour. In this work an initial manual segmentation is performed by the user and then this contour is propagated over all phases exploiting information from adjacent images. As with the traditional snake the use of GVF snake still suffer, to some degree from the problem of concavities and weak edges which is significant in CMR image.

The work of Berbari (El Berbari et al., 2007)(see Figure 3.3), uses a GVF snake to segment endocardium on a filtered image and for the epicardium image Berbari introduces a distance constraint by measuring the thickness of the myocardial around the septum area and then computes a new edge map keeping the information between the endocardium boundary to the dilation of myocardial thickness. This work solve the problem of weak edges of GVF by introduce distance constraint from the image information.

Ciofolo (Ciofolo et al., 2008) applied the active contour in segmenting a late enhance (LE) image. In this work 3-D shape terms are combined which is achieved by applying active contour to cine image which best matches with the LE image and builds the 3-D mesh and region term to the active contour formulation for the final segmentation of the LE image. Han-Yeoun (Hae-Yeoun et al., 2010) proposed the combination of region growing to segment the endocardium and active contour guided by the endocardium boundary and myocardial signal information estimated by iterative thresholding.

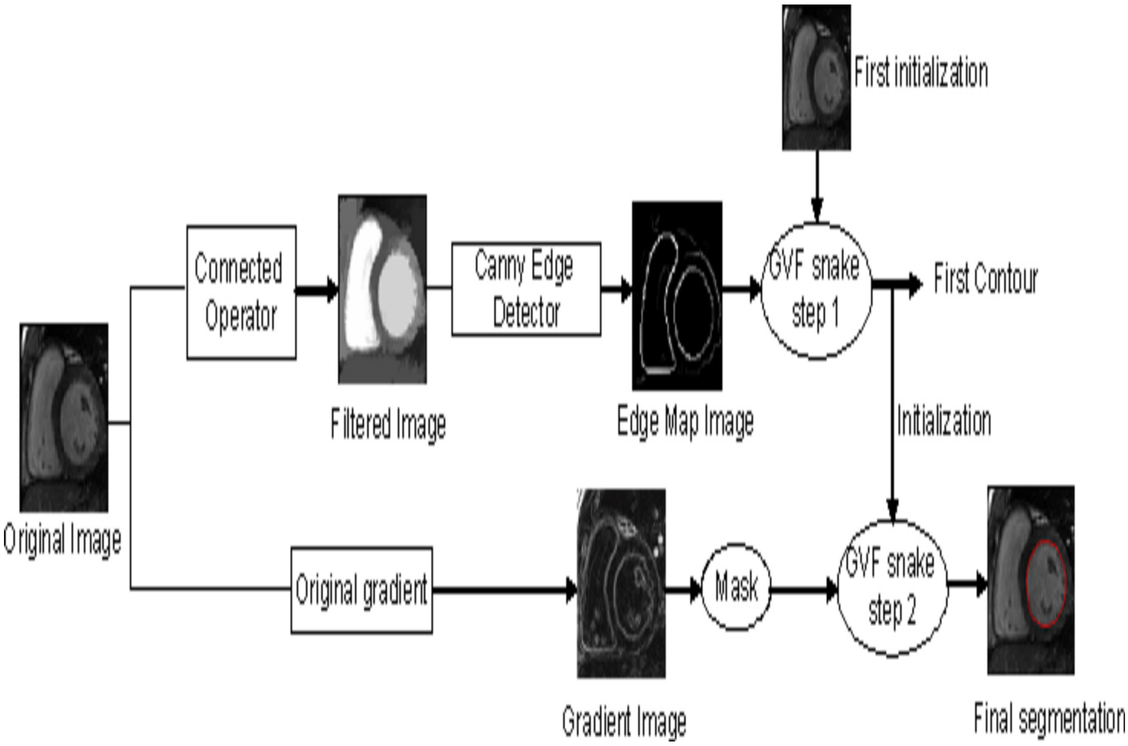

Figure 3.3: GVF Snake with Shape Constraint (El Berbari et al., 2007)

Due to their flexibility active contours have been widely used for medical image segmentation, with many of the authors have suggested method to adapt active contour specific for LV wall segmentation such as shape constraint, introducing region based term, pre-process the CMR image and introducing new edge map. The summary of methods fall under this category is shown in Table 3-4.

Table 3-4: Deformable based segmentation methods (active contour)

		Author	Basic Principle
Deformable model based methods	active contour algorithm	(Santarelli et al., 2003) (Jinsoo et al., 2003) (Hautvast et al., 2005) (El Berbari et al., 2007) (Ciofolo et al., 2008) (Hae-Yeoun et al., 2010)	GVF snake tensor-based orientation gradient force is introduced as snake energy to segment the LV wall propagate the active contour over CMR image phase and exploiting the information from adjacent frame to segment the LV wall GVF snake with distance constraint for the segmentation of epicardium Applying active contour on cine image and created 3-D mesh region then using active contour for LE image and used 3-D information for final LV wall on LE image. Combination of region growing with active contour.

3.3.2.2 Level set method

The level set method (LSM) was introduced by (Osher and Sethian, 1988, Malladi et al., 1995) and is a powerful technique which can easily integrate different information into one framework. The central idea of LSM is to track the motion of a curve C which separates one region from another in the whole space. Instead of representing the curve C explicitly, the curve C in LSM is represented implicitly by zero level set $C(t) = \{(x, y) | \phi(t, x, y) = 0\}$ of a level set function $\phi(t, x, y)$. The evolution equation of the level set function ϕ can be written in the following general form:

$$\frac{d\phi}{dt} = F_{\text{int}} + F_{ext} \qquad 3\text{-}4$$

where F_{int} *and* F_{ext} are the respective internal and external energy functions that drive the evolution of the level set function with various arguments, such as the curvature gradient and image intensity gradient.

In the implementation of LSM for LV wall segmentation the regularization term does not change much and is often curvature based. The contribution comes from with the data driven term.

A prior shape is introduced to the LSM evolution either by pixel-wise stochastic level-set representation of training data (Paragios, 2003), or incorporating probability density function from manually segmented boundaries (Lynch, 2006) (see Figure 3.4).

Figure 3.4: Images show the probability density functions from a priori manually segmented images. (a) Shows the combined contours while (b) and (c) show the endo- and epicardium boundaries, respectively. Darker gray tone defines a higher probability of the boundaries (Lynch et al., 2006b)

To further improve the LSM a region based term has also been introduced, which is based on the region homogeneity (C. Pluempitiwiriyawej et al., 2005, Ting et al., 2008). Another level-set based method incorporating both gradient and region-based information was proposed in Fritscher (Fritscher et al., 2007). In incorporating both gradient terms and region terms the problem of noise can be reduced. Next the extension of the LSM is in Lynch (Lynch et al., 2008), which proposed to incorporate prior knowledge about cardiac temporal evolution in LSM formulation and applied expectation and maximisation algorithms to tracks the LV wall deformation.

Another extension of the LSM was proposed by Ben Ayed (Ben Ayed et al., 2009) that considered the intensity distribution overlap that exists between myocardium and cavity, and background and myocardium. From the information he proposed a new energy term which measures how close the overlaps are to a manually obtain boundary in the first frame. Punithakumar (Punithakumar et al., 2010) further improved the work , by introducing recursive Bayesian filtering as the post processing step in LV wall segmentation. Table 3-5 summarize segmentation method based on level set.

Table 3-5: Deformable based segmentation methods (level set)

		Author	Basic Principle
Deformable model based methods	level set method (LSM)	(Paragios, 2003, Lynch et al., 2006b)	Prior information using PDF from hand segmented data
		(C. Pluempitiwiriyawej et al., 2005, Ting et al., 2008)	Region based term based on region homogeneity to drive the level set.
		(Fritscher et al., 2007)	Combination of region based and gradient based
		(Lynch et al., 2008)	In cooperating prior knowledge into LSM formulation and combined with EM to track the LV wall segmentation
		(Ben Ayed et al., 2009)	New energy term which measure closeness from manually obtained boundary from first frame.
		(Punithakumar et al., 2010)	(Ben Ayed et al., 2009) + introducing recursive Bayesian filtering fro post processing

3.3.3 Statistical models methods

Table 3-6 shows a summary of segmentation method based on statistical technique. Statistical model-based approaches are able to provide constraints derived from a training set on the analysis for improved LV wall segmentation. Thus automatic LV wall segmentation can benefit from the use of a statistical model regarding shape and/or pixel intensity, to increase its robustness and accuracy. Two commonly used techniques are Active Shape Models (ASM) and Active Appearance Models (AAM) (Cootes et al., 2001).

Table 3-6: Statistical model segmentation methods

		Author	Basic Principle
Statistical models methods	Active Shape Model (ASM)	(Van Assen et al., 2006)	3-D atlas constructed using non-rigid registration and the use of fuzzy c-means to detect the feature points.
		(O'brien et al., 2011)	Using unified framework which consist of shape, spatial, and temporal variation of LV
	Active Appearance Model (AAM)	(Mitchell et al., 2000)	AAM for LV wall segmentation
		(S. C. Mitchell et al., 2001, Honghai et al., 2010)	AAM+ASM
		(S. C. Mitchell et al., 2001)	Multistage AAM
		(Honghai et al., 2010)	AAM follow with ASM. Then combination of the two is used to compute the new appearance model.
		(S. C. Mitchell et al., 2002)	3-D AAM

3.3.3.1 Active shape models (ASM)

ASM (Cootes et al., 1995) is a deformable technique which uses 2-D or 3-D shape variation from training dataset and iteratively deforms to fit the new image using the statistical information from the training dataset. The constraint is based on point distribution models (PDM) which is obtained by Principal Component Analysis (PCA) (Abdi and Williams, 2010) that provides number of constraint parameters, which control the variation found in the training dataset. Van Assen (Van Assen et al., 2006) proposed the use of a 3-D atlas which was constructed from non-rigid registration for the shape model. Then the feature point detection is performed by fuzzy inference system based on fuzzy C-means as illustrated in Figure 3.5. O’ Brien (O'brien et al., 2011) proposed a combination of shape, spatial, and temporal variation of LV wall into a unified framework that results in reduce of training time.

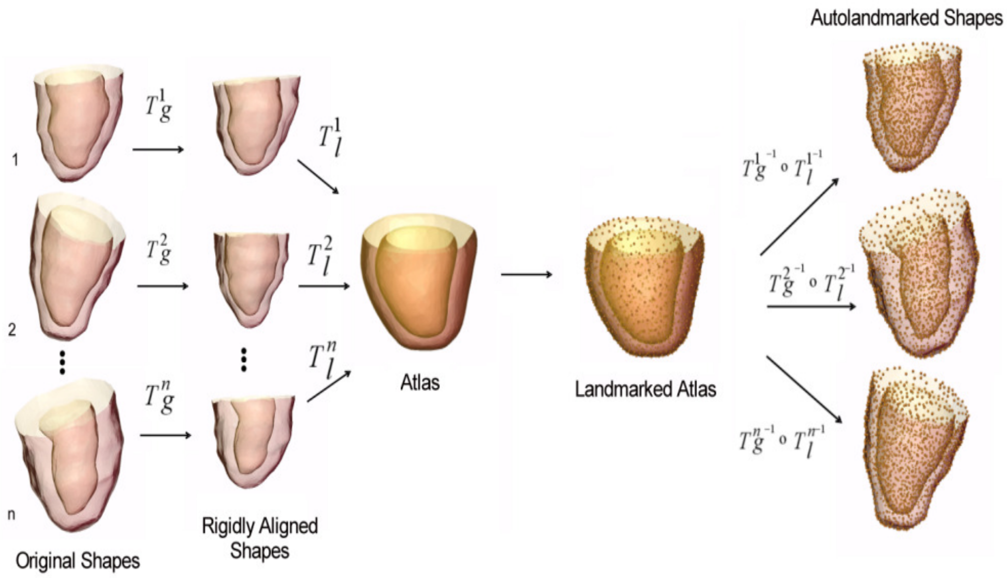

Figure 3.5: Atlas construction, a set of final global (Tg) and local (Tl) transformations can take any sample shape of the training set, to the atlas coordinate system. On the left, there is landmark propagation. Once the final global and local transformations are obtained, they are inverted and used to propagate any number of arbitrarily sampled landmarks on the atlas, to the coordinate system of the original samples (Van Assen et al., 2006)

3.3.3.2 Active appearance models (AAM)

In AAM instead of only shape modelling as in ASM, the image intensity values of the structures and surroundings are taken into account to build the complete models. AAM has better convergence than ASM but is much slower.

Mitchell (Mitchell et al., 2000) proposed the use of AAM for LV wall segmentation and demonstrated the clinical potential of AAM. A Hybrid model which combine the strength of both ASM and AAM are proposed in (S. C. Mitchell et al., 2001, Honghai et al., 2010). In Mitchell (S. C. Mitchell et al., 2001) a multistage AAM is proposed to combine an AAM which is optimised on global appearance but imprecise local structures, with an ASM which has better local structure. Honghai (Honghai et al., 2010) further improved the hybrid method by first calculating the shape information from AAM and the next stage using the result from ASM to calculate the shape information of the ASM. The two shapes are then combined to compute the new appearance model indices. This hybrid approach provides extra momentum to bring model matching out of local minima and thus increases the chance of finding a global minimum.

The extension of 3-D AAM is proposed in Mitchell (S. C. Mitchell et al., 2002), the extension of 3-D AAM is achieved by extending the two-dimensional PDM to three dimensions. The great amount of data involve to model a 3-D surface leads to increased computational cost.

3.3.4 Atlas based methods

In Atlas-based segmentation methods, image segmentation is regarded as a registration problem. The methods rely on existence of a reference image (or the atlas) in which structure of interest is labelled by manually segmenting an actual image. It is then used to find the transformation that maps the pre-segmented atlas to the study image. Therefore the key to atlas based segmentation algorithm is to design a registration method capable of computing the transformation between the atlas and the image to be segmented.

Lorenzo-Valdes (M. Lorenzo-Valdés et al., 2002) proposed a method based from the average of 14 healthy volunteers to reconstruct and non-rigid registration algorithm based on cubic-spline to register the model in the form of a cardiac atlas to a cine sequence of 3D MR volumes. In Lorenzo (Maria Lorenzo-Valdés et al., 2004), combines expectation and maximization algorithm and a 4D probabilistic atlas of the heart for the automatic segmentation of 4D cardiac MR images. Zhuang (Zhuang et al., 2008) used similarity criterion based on region based registrations to introduce the heart anatomical constraints and fluid deformation model for the registration of the atlas to the image to be segmented. Xiahai (Xiahai et al., 2010) proposed new Locally Affine Registration Method based on mutual information (MI) or normalized mutual information (NMI) as the global cost function and optimize the affine transformations within a global scheme. The methods are summarized in Table 3-7.

Table 3-7: Atlas based segmentation methods

		Author	Basic Principle
Atlas based methods		(Lorenzo-Valdés et al., 2002 (Maria Lorenzo-Valdés et al., 2004) (Zhuang et al., 2008) (Xiahai et al., 2010)	Cubic spline registration in the form of a cardiac atlas to a cine sequence of 3D MR volumes. EM+ 4D probabilistic atlas region based registrations + fluid deformation model for the registration of the atlas to the test image.

3.4 Edema Segmentation and Quantification Methods

Automatic edema region segmentation for T_2-weighted images have received limited attention compared to segmentation of infarcted area from LE images. This section describes the development of pathological study of the LV wall from manual segmentation to automatic segmentation starting from the segmentation of LE image This is because of its similar characteristic the methods applied to LE can be transform to T_2-weighted image with some modification.

The importance of segmenting and quantifying the edema is because its ability to determine AAR. When the result of the edema is superimposed with the infarcted region a viability assessment can be performed and treatment can be personalised to each patient.

3.4.1 Semi automatic methods

Semi-automatic methods where the LV wall is outlined manually have been proposed by some researchers and by using different segmentation techniques the acute area from LE image or T_2-weighted images are then quantified. To speed up the quantification of edema some semi-automatic methods used simple intensity thresholding based on the standard deviation (SD) method (Fieno et al., 2000, Setser et al., 2003, Green et al., 2009). (Amado et al., 2004) use multi-pass region-growing algorithm. Here the user needs to click at the hyperenhanced region to provide the seed point. The final infarct boundaries are then determined using the Full Width Half Maximum (FWHM) criterion. (Hsu et al., 2006) measured infarct size by a computer algorithm based on automated feature analysis and combined thresholding with delayed enhanced MR image. Fuzzy C-mean (Vincenzo Positano et al., 2005, Kachenoura et al., 2008) (see Figure 3.6). (Hennemuth et al., 2008) combined intensity histogram with constraint watershed to segment the hyperenhanced tissues. (Heiberg et al., 2008) applied k-means algorithm to adaptively set the k+SD threshold to automatically quantify the infarction area.

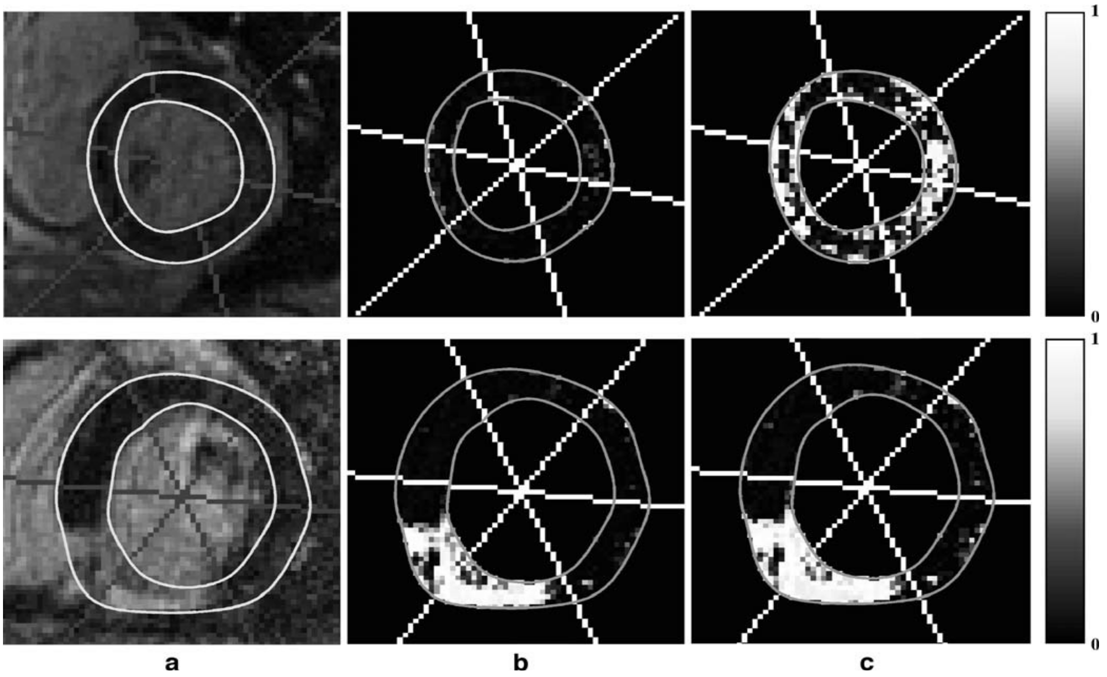

Figure 3.6: Application of the Fuzzy C-means clustering algorithm on a slice without infarcted area (upper row) and on a slice with inferior infarction (lower row). (a) Raw images, (b) Membership maps for the CE class when applying the fuzzy c-means on both myocardium and cavity and (c) only on the myocardium

3.4.2 Automatic methods

Automatic methods have been proposed by Dikici (Dikici et al., 2004) where the LV wall is segmented by using region segmentation and active contour on cine images and then using non-rigid registration the segmentation result is superimposed on the LE images. Then a Support Vector Machine (SVM) is used to classify non viable tissues. Elagouni et al (Elagouni et al., 2010) proposed the use of active contour with geometrical template to segment the LV wall on the LE CMR image and then used a shape prior to the segmentation by building a 3-D mesh from the segmentation of Cine MRI. Then the LV wall is fitted with myocardial intensity histogram by using a mixed model consisting of a Rayleigh distribution for normal tissue and a Gaussian distribution for MI region (see Figure 3.7) . They demonstrated that their method could delineate the hyper-enhanced MI region well compared with a manual approach for LE images. The disadvantages of this method are that it is time consuming since it needs segmentation of two CMR images for each slice, and the need to identify the phase which best matches the late-enhancement acquisition time in the cardiac cycle. Kadir et al (K Kadir et al., 2010b) proposed an automatic method, where the LV wall is segmented based on a radial search method according to signal intensity difference between myocardial tissue and blood pool. This was done by combining a fuzzy method for LV boundary segmentation and a hybrid thresholding edema sizing algorithm, which is based on a combination of a histogram thresholding with an iterative dilation, to automatically quantify edema from T_2-weighted MRI. The problem with using this technique is that the method could be unstable when the LV wall shows great heterogeneity in signal intensity and the characteristic of dark CMR signal is not Gaussian distributed but more of a Rician distribution which a is better representation of the dark CMR signal (Hákon Gudbjartsson and Patz, 1995b).

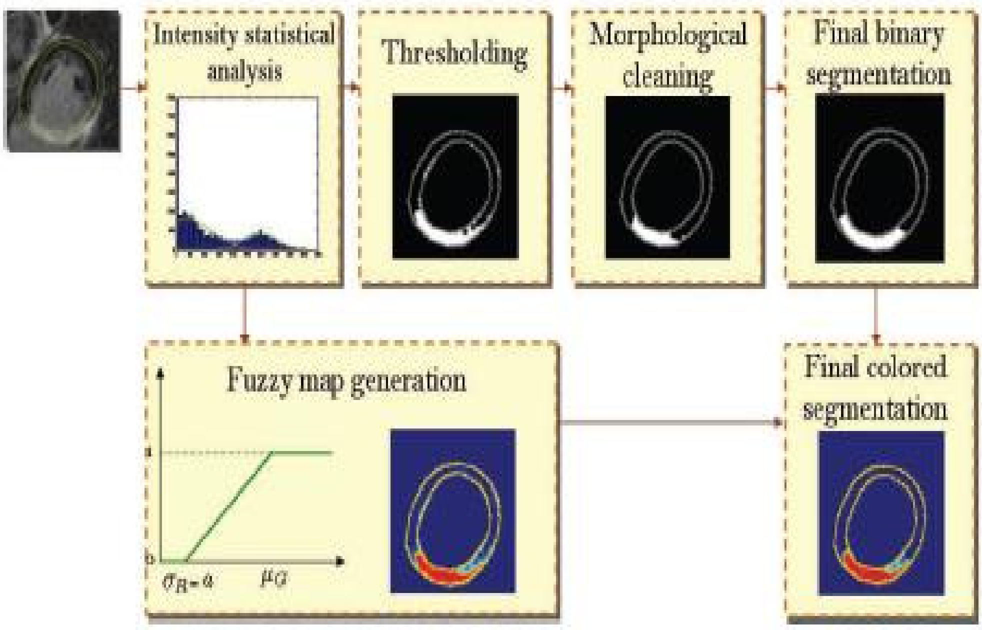

Figure 3.7: Pathological Tissues Detection Scheme (Elagouni et al., 2010)

3.5 Three-Dimensional Reconstruction of CMR Image

Three-dimensional (3-D) imaging of the heart has become one of the fastest growing research areas in medical imaging and it is made possible with the advent of hardware and new methods in CMR imaging. The 3-D imaging methods have been used for the study of physiological functions, 3-D reconstruction and visualization and for surgical planning (Frangi et al., 2001). Currently most of the research in 3-D imaging concentrates on the study to extract physiological characteristic of the heart such as shape and function. Thus research into pathological characteristic of the LV wall either from LE image or T_2-weighted image is very much of interest. In this section a review of 3-D imaging techniques used for the investigation of LV wall are presented.

3.5.1 3-D imaging for investigation of physiological function

The majority of 3-D imaging works deal with the physiological study of the heart such as motion analysis, and wall thickening. This section describes the development in the investigation of physiological function of the LV heart.

3.5.1.1 Wall motion analysis

The study of wall motion analysis involves the detection of abnormal wall movement. To reconstruct the wall motion closed meshes have been proposed to represent the LV such as spheres, ellipsoids or cylinders. In Azhari (Azhari et al., 1992) a hollow conical shell is used to characterize transmural motion. Huang (Huang and Goldgof, 1993) used bending and stretching model to represent the LV wall. The limitations of these traditional models are that they do not provide intuitive motion parameters to describe the motion of the LV. A popular approach in 3-D wall motion analysis is to use deformable techniques (Frangi et al., 2001). Stalidis (Stalidis et al., 2002) proposed a multiphase and multislice approach which uses generating-shrinking neural networks combined with spatiotemporal parametric modelling for 4-D cardiac MRI analysis. Li (Li et al., 2005) used harmonic phase called 3-D HARP which is time invariant to track the motion of the LV mesh model through cardiac cycle. Other alternative approaches are based on statistical shape model (Cootes et al., 1995). Frangi (Frangi et al., 2002) proposed using non-rigid registration to build 3-D ASM by finding corresponding landmarks between surfaces. (Remme et al., 2004)

3.5.1.2 Wall Thickening analysis

3-D wall thickening analysis has been shown to be more accurate in detecting regional area of ischemic compared to wall motion analysis (Azhari et al., 1990). Thus many studies have been done to incorporate wall motion index to the analysis of the LV wall. Taratorin (Taratorin and Sideman, 1995) and Azhari et al (Azhari et al., 1996) used the technique of dividing the LV wall into small cuboids. Then the regional wall thickness analysis is performed by dividing the volume of a particular section by averaging the area of the LV wall surface. Buller and Bolson (Buller et al., 1995, Bolson et al., 1995) used a centreline method where a three-dimensional surface was constructed at mid-myocardium through all the midpoints of the centerline chords. Ordas (Ordas and Frangi, 2005) used 3-D ASM to build a 3-D using non-rigid registration from a training data set of 90 hearts with common pathology. As with any statistical model the accuracy of the model is constrained by the quality of its data set. In Sun (Sun et al., 2008), they model the 3-D heart wall by explicitly defining its skeleton (medial model) and developing the boundary geometry according to medial geometry. Tobon (Tobon-Gomez et al., 2010) used a 3-D statistical model from 100 patients to build the shape models of the 3-D LV wall. The practical limitation in building statistical shape models, and in particular point distribution models (PDM), is the manual delineation of the training set.

3.5.2 3-D imaging for investigation of pathological characteristics

The advantage of 3-D visualization on pathological characteristics of the LV wall is in its ability to better visualize the extent of injury to the LV wall compared to 2-D visualization. This section describes the development in the investigation of pathological characteristics of the LV heart.

Positano (V. Positano et al., 2003) used a semi automatic LV boundary to segment the LV wall. Then the infracted area is classified using Fuzzy C-means algorithm. Finally a 3-D model is reconstructed by using a simple graphical tool. The disadvantage of the proposed 3-D visualization is that, it is very primitive with the 3-D image appearing jagged and clearly stacking from one slice to the other. Noble (Noble et al., 2004) proposed using a shape based method to create prior information for smooth 3-D contour followed by a marching cubes algorithm. Then rigid registration method is applied to align cine-MR contour to LE image. Next the scar area is manually delineated. The information can then be visualized into 3-D representation. The disadvantage of this 3-D visualization is that the system requires human intervention such as manual segmentation of the scar area. Termeer (Termeer et al., 2007) proposed a comprehensive visualization of artery diseases. Here the LV wall is manually segmented, and then the scars tissues are classified by the user specifying two regions which are used as density ranges for a healthy region and a scar region. The 3-D visualization is based on polygonal mesh for the whole heart data and direct volume rendering is used for the LE image. Then the two images are blended together. In Hennemuth (Hennemuth et al., 2008) used semi automatic method based on live wire to segment LV wall on the LE images. Then rigid registration method is used to align whole heart volume to the LE slices. A combination of intensity histogram with constraint watershed is then used to segment the scars tissues. Lastly using surface rendering the 3-D model of the heart can then be constructed. Lehman (Lehmann et al., 2009) applied a 3-D model integrating viability information into a cardiac model for interventional guidance. The technique used 3-D model based segmentation applied to the cine image by adapting triangular surface mesh to an image and then the cardiac model of the whole heart 3-D MRI data set that matches to the 3-D LE MRI data set. Then to classify the LV wall into viable and non-viable tissues a simple thresholding is applied, where the thresholding value is manually set. The 3-D shape can then be reconstructed from the model incorporating the scar tissues.

3.6 Conclusion

This chapter discussed various image processing techniques for CMR imaging to solve the problem of segmentation, edema quantification and 3-D visualization and to develop a semi or fully automatic edema quantification with 3-D visualization system.

Image pre-processing is an important aspect of any image processing algorithm. Since the original T_2-weighted CMR image consists of characteristic that make the automatic segmentation difficult, such as heterogeneity in the blood pool region, presence of papillary muscles, and weak edges for the epicardium segmentation. Thus this research proposed the use of non linear filtering based on anisotropic diffusion method to process the image for further processing. This is due the advantages of the filter in terms of edge preserving and its capability to reduce grey scale inhomogeneity.

When considering the development of automatic quantification of edema it is important to consider automatic localization of the LV wall. Hence we proposed the use of object recognition methods based on fuzzy rules to localize the LV wall.

The review of the existing segmentation technique showed that LSM is a very popular segmentation method used in medical image segmentation with the advantages due to its ability to deal with changes in topology such as splitting and merging which makes it a great segmentation method for these applications. Hence a new Level set method with additional shape constrain is used in this research for solving specific challenges in the segmentation of LV wall on T_2-weighted CMR image.

The automatic quantification of edema on T_2-weighted images will directly benefit the clinician in estimating viable myocardial tissues in a timely fashion. From the review the majority of works done are on LE CMR image and not many works have been done on T_2-weighted CMR images. Popular methods such as thresholding and classification have been investigated. Since a CMR image is governed by Rician distribution Thus a modified two statistical mixture model is used with the capability to include microvascular obstruction (MVO) within the edema areas are applied in this research.

Finally 3-D visualization methods were reviewed. In the literature it was found most of the work involved the investigation of physiological functions of the heart and few investigate the pathological characteristics of the heart. Thus the research into 3-D visualization of edema from T_2-weighted image is an interesting topic to be developed. In our research we proposed a modified surface rendering technique to reconstruct a 3-D image of the LV wall with the ability to visualize the edema areas within the 3-D wall volume.

CHAPTER 4

4. IMAGE DATA SET AND EVALUATION PARAMETERS

4.1 Introduction

The previous chapter reviewed CMR imaging in general and specifically on edema quantification and 3-D visualization. The main objective of the research is to develop automatic edema quantification with 3-D visualization which will help the clinician to easily assess the extent of edema and visualize the location of edema within the LV wall volume.

At present the only publicly available CMR imaging data set is based on Cine image. Therefore to the best of our knowledge there is no publicly available T_2-weighted CMR image database that is suitable for the purpose of this research. The key factor contributing to the success of this research has been the collection of real T_2-weighted data from patients with of acute myocardial infarction.

MRI data were collected at Golden Jubilee National Hospital as part of bi-weekly visits to the Department of Radiology. The MRI data in our database are taken from patients who recently experienced a heart attack. During the acquisition process the patient will lie on a motorized bed that can be moved inside the scanner. Then patient will enter the MRI scanner head first. A computer is used to operate the MRI scanner. A radiographer operates the computer in a separate room to the patient. However, the patient will be able to talk to the radiographer through an intercom and the radiographer will be able to monitor the patient at all times on a television monitor.

In the thesis the data is separated into two datasets. The first dataset consist of 15 patients used for the development of the algorithm and the second dataset consists of another 15 patients used to test the ability of the algorithm with unseen data. The collection of the data is presented in the first section of this chapter.

In any algorithm development it is important to assess the capability of the proposed algorithm with some standard evaluation testing. Section two presents evaluation assessments used to assess the performance of the proposed algorithm

4.2 Image Data Set

T_2-weighted CMR image data was obtained from Golden Jubilee National Hospital, Glasgow. The image data used in this research is the standard short axis views (SA views) and long axis view (LA). The studies were performed on 30 patients (24 male, 6 female) post primary percutaneous coronary intervention (pPCI). The Mean (SD) age was 54 (13) years with known artery disease and proven visible edema. Time from pPCI MRI imaging was mean (SD) 25 (9) hours. The study protocol was approved by the local ethics committee and all patients gave written informed consent. MRI was performed on a Siemens Magnetom Avanto (Erlangen, Germany) 1.5-Tesla scanner with an 8-element phased array cardiac surface coil. A breath hold bright blood T_2-weighted Acquisition for Cardiac Unified T_2 Edema (ACUTE) pulse sequence with normalisation for coil sensitivity: acquisition time 7-12s, matrix 192 x 192, flip angle 180°, echo time (TE) = 1.69 ms, bandwidth = 789 Hz/pixel, echo spacing = 3.4ms, echo train length = 29 and trigger pulse = 2 i.e. alternate heartbeats. The voxel size was 1.9 x 1.9 x 6 mm^3. Myocardial infarction was imaged using segmented phase-sensitive inversion recovery (PSIR) turbo fast low-angle shot starting around 7 minutes after intravenous injection of 0.10 mmol/kg of gadoterate meglumine (Gd^{2+}-DOTA, Dotarem, Guebert S.A.). Typical imaging parameters were: matrix = 192 x 256, flip angle = 25°, TE = 3.36 ms, bandwidth = 130 Hz/pixel, echo spacing = 8.7ms and trigger pulse = 2. The voxel size was 1.8 x 1.3 x 8 mm^3. All images were stored in the standard digital imaging and communications in medicine (DICOM) format. Figure 4.1 illustrate an example of image from one patient from the database.

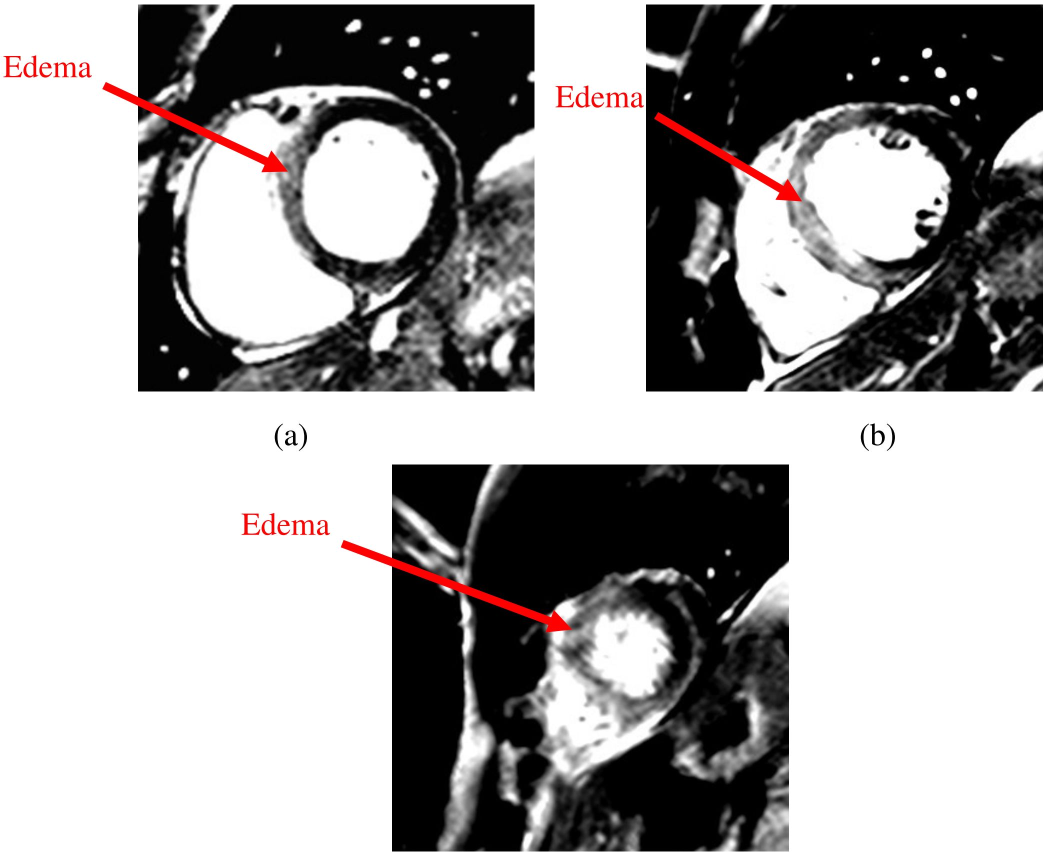

(a) (b)

(c)

Figure 4.1: T_2 Weighted CMR Image of a single patient (a) Basal, (b) middle and (c) apical

4.3 Objective Evaluation Indicators

Validation of any algorithm for this work is difficult because there is no standard database to assess the performance of the proposed algorithm for comparative study. However several studies have shown that manual techniques can be used to assess the performance of any proposed algorithm (Thiele et al., 2006, Hsu et al., 2006). Thus in this thesis manual techniques such as segmentation of LV wall and quantification of edema from one experienced clinician is used as the gold standard for the performance evaluation of the proposed methods.

4.3.1 Correlation analysis

A correlation analysis is performed to measure the strength of the linear relationship between two sets of variables. The relationship of the correlation analysis can be easily visualized by using scatter plot. Figure 4.2 and Figure 4.3 illustrate the examples of positive correlation and negative correlation.

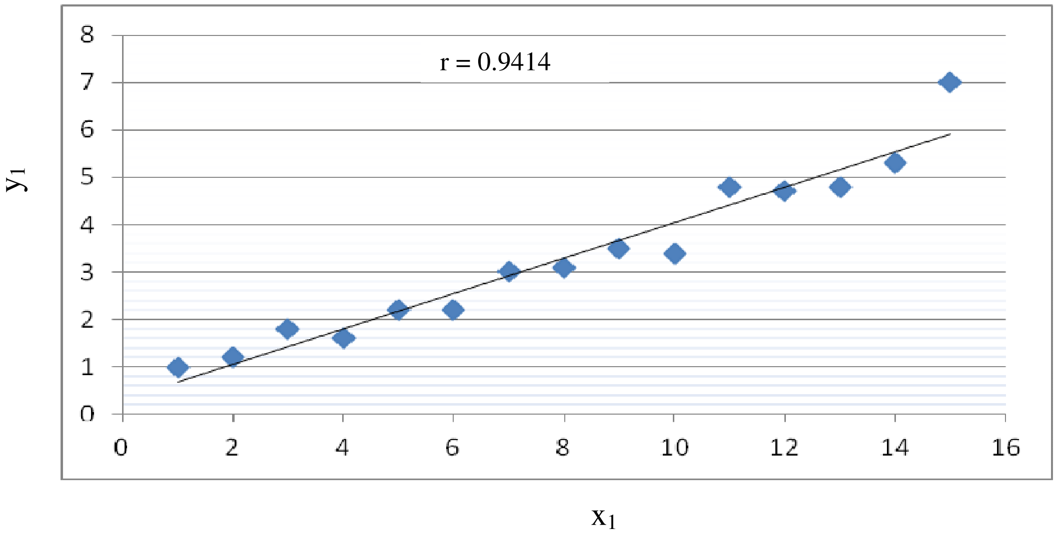

Figure 4.2: Positive Linear correlation

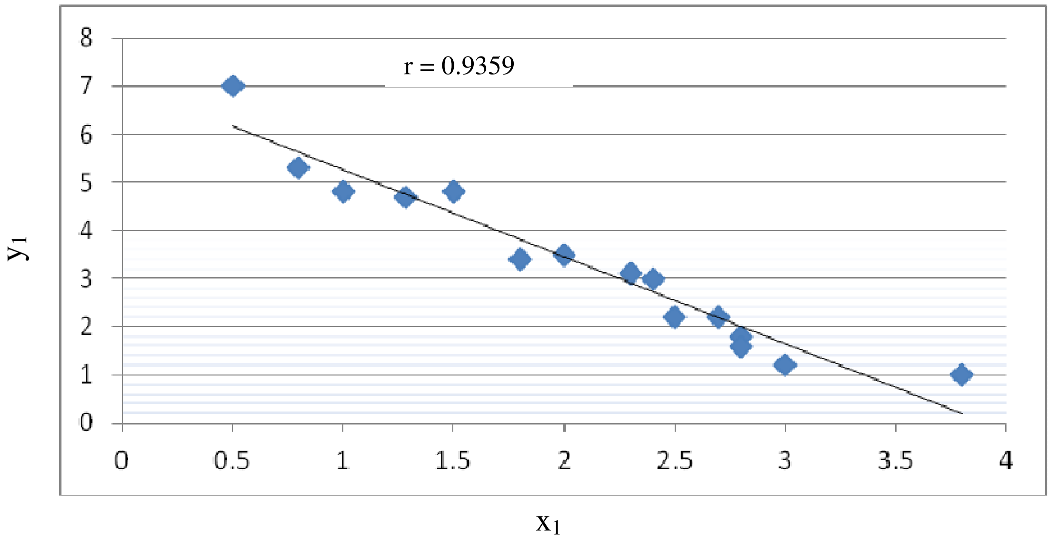

Figure 4.3: Negative Linear correlation

Notice that in Figure 4.2 as the heights increases, the displacement of the data also increases. If this is a perfect positive correlation, all of the points would fall on a straight line. The more linear the data points, the closer the relationship between the two variables. In Figure 4.3 a negative correlation is observed. In this example as *x*-axis increases, the *y*-axis decreases. If this is a perfect negative correlation all of the points would fall on a line with a negative slope. The more linear the data points, the more negatively correlated are the two variables. Another parameter that can be observed from both figures is the r value, which is the correlation coefficient and is used to measure the strength of the linear relationship in the sample observation. A higher r value indicates a higher linear relationship between the two samples. A mean $r = 1$ indicates perfect linear relationship.

4.3.2 Bland-Altman analysis

The Bland-Altman analysis (Altman and Bland, 1983, Bland and Altman, 1999) is a graphical tool to measure agreement between two methods. The need for the Bland-Altman analysis is because correlation analysis can only measure linear correlation between two variables but does not explain the difference of the two methods. Figure 4.4 shows a Bland-Altman plot for two measures.

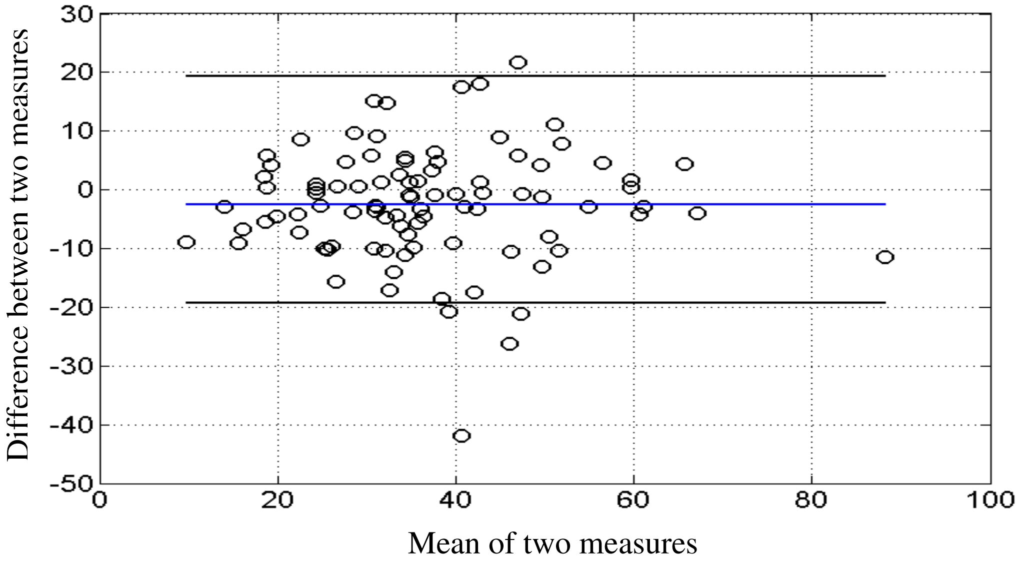

Figure 4.4: Bland-Altman analysis

In Bland-Altman the data is plotted by the difference between the measurements of the two methods for each subject on the *y*-axis against their mean on the *x*-axis. Useful information that can be derived from the Bland-Altman analysis is the 95% confidence limit or 1.96 SD of the differences between the two methods. The presentation of the 95% limits of agreement is for visual judgement of how well two methods of measurement agree. The smaller the range between these two limits the better is the agreement. Another important parameter that can be derived from the Bland-Altman plot is the mean bias. A negative bias tells that method A tends to overestimate against method B and for positive bias tells that method A tends to underestimate against method B.

4.3.3 Dice similarity coefficient

Dice similarity coefficient (DSC) is a measurement of spatial overlap used widely for comparing segmentation results (Dice, 1945). The DSC is defined as:

$$DSC(A,B)=\frac{2(A\cap B)}{A+B} \qquad 4\text{-}1$$

where $\cap$ represents the intersection of the two regions and $A+B$ represents the sum of the areas from the two methods. Dice similarity coefficient $(A,B)=1$ indicates a perfect overlap between A and B and $DSC(A,B)=0$ means no overlap between A and B. Zijdenbos *et al.* (Zijdenbos et al., 1994a) suggest that a Dice similarity coefficient >0.7 indicates good agreement.

4.3.4 Box plot

Box Plot (Mcgill et al., 1978), a useful graphical method for summarizing and comparing data from 2 or more samples. Figure 4.5 shows an example of a Box plot on two classes of data.

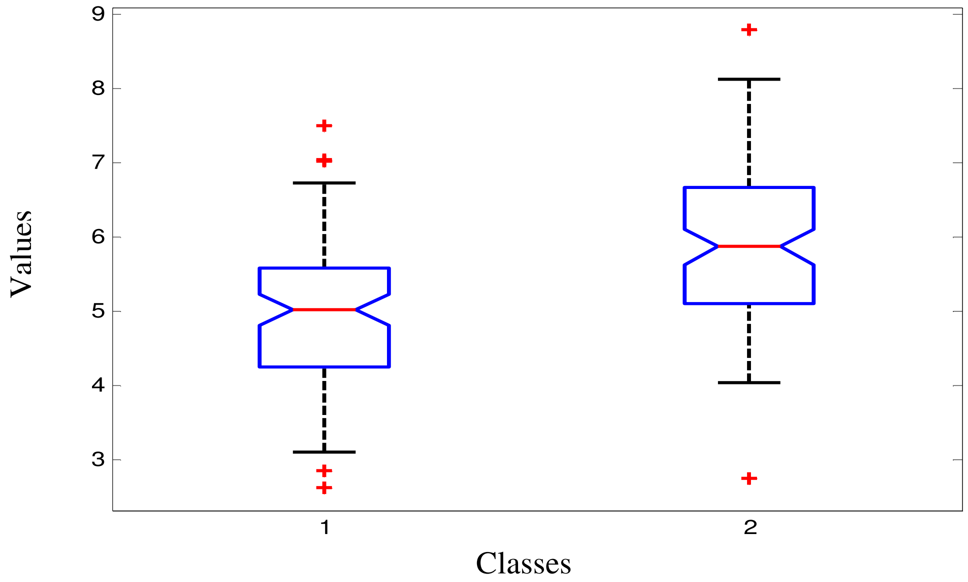

Figure 4.5: Box Plot

The box plot consists of: Vertical axis = response variable; Horizontal axis = classes' identification. The bottom dash is the data minimum; the bottom of the box is the estimated 25% point; the middle x in the box is the data median; the top of the box is the estimated 75% point; the top dash is the data maximum; and the red crosses representing the outliers of the sample data. Another parameter that can be interpreted from the Box plot is in term of the way the data sway. This can be seen by looking at the position of the median in the box. If the median line within the box is not equidistant from the hinges then the data is skewed.

4.4 Conclusion

In this chapter the real T_2-weighted CMR data collection was presented. The chapter describe the type of T_2-weighted CMR images being acquired. The chapter also describe objective evaluation indicators used to test the performance of the proposed algorithm.

CHAPTER 5

5. TWO DIMENSIONAL LEFT VENTRICLE SEGMENTATION FOR T_2 WEIGHTED CMR IMAGE

5.1 Introduction

In chapter 4 the collection of CMR data used in this thesis was described. The chapter also introduced quantitative index used to investigate the performance of the proposed method. In chapter 3 some popular techniques in image pre-processing, LV wall localization, edema segmentation and quantification and 3D visualization have been discussed. Since the majority of the work carried out deals with Cine type of CMR images. There is a need to develop automatic LV wall segmentation for edema quantification and 3D visualization on T_2 weighted CMR images.

Major challenges in automatic systems to segmenting LV are: the heterogeneities in the blood pool region, presence of papillary muscles in the LV wall cavity, weak edges around the epicardium of the LV, and the fact that the presences of edema in the myocardial tissues have higher signal intensity variation compared to normal myocardial tissue. Furthermore the precise location of the edema cannot be predicted which complicates the segmentation process.

This chapter presents a novel automatic LV wall segmentation algorithm using variational LSM with additional shape constraint.

This chapter is organized as follows. In Section 5.2 the overview of automatic LV wall segmentation algorithm is presented. Section 5.3 describes the image pre-processing technique based on anisotropic diffusion (Perona and Malik, 1990) and its advantages when applied to CMR images. Next in section 5.4 we present a novel fuzzy based technique for LV wall localization for the initial stage of LV wall segmentation. Section 5.5 describes the theory of LSM (Malladi et al., 1995) which is the basis of the proposed algorithm. Then a novel LV wall segmentation using LSM with additional shape constraint is proposed. In our work we used image information to provide additional shape constraint to solve the problem of weak edges on the epicardium of the LV wall. Section 5.6 presents the results and discussion obtained by applying the technique to real data collected from the Golden Jubilee National Hospital. Finally section 5.7 concludes the chapter.

5.2 Automatic LV Wall Segmentation Algorithm

An overview of the proposed automatic LV wall segmentation method is shown in Figure 5.1. Image pre-processing is used to create homogenous region within the LV blood pool region. The second process is to locate the position of the LV in the SA image automatically. This is an essential step to provide an accurate initialization for LV segmentation. However the problem in estimating the LV location is that the LV within the thoracic wall is highly variable, thus a simple assumption on LV location is unfeasible. In our implementation we propose the use of fuzzy based reasoning to locate the initial position for the segmentation of the LV wall. Subsequently endocardium segmentation is performed using the LSM proposed by Chunming (Chunming et al., 2005). The advantage of this LSM is that it eliminates the need to reinitialize the level set function to signed distance function as in traditional LSM. Once the endocardium has been segmented the averaged LV wall thickness in the septum region is assessed in order to constraint the epicardium boundary tracking. The constraint information is then used to create a new edge map for the LSM. Finally the new LSM with additional shape constraint is used to segment the epicardium. These process steps are described in detail in the next sections.

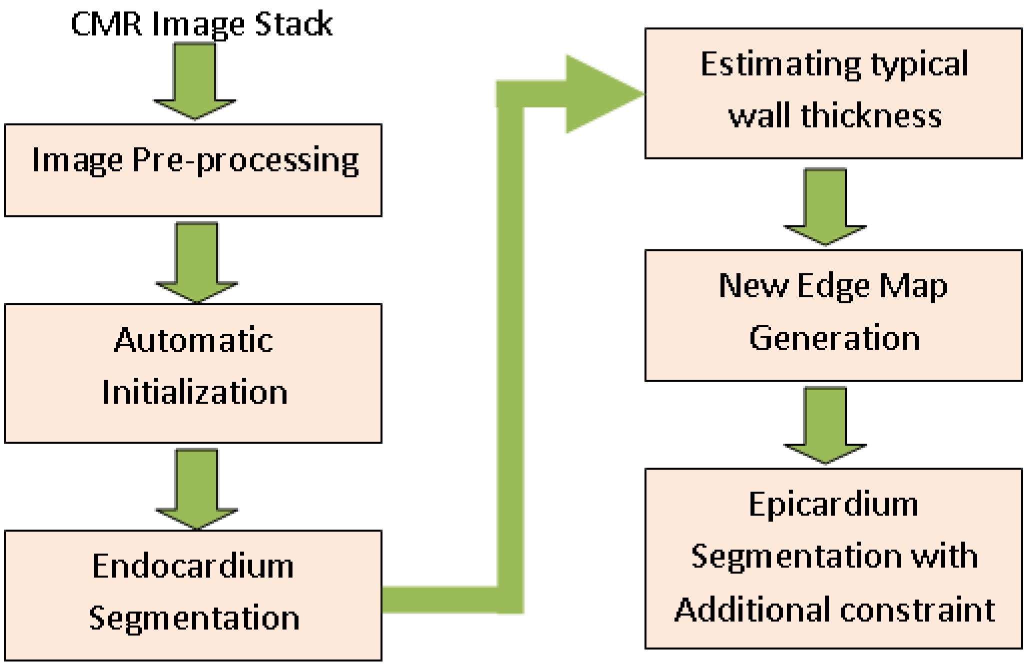

Figure 5.1: Automatic LV Wall Segmentation Algorithm Overview

5.3 Image Pre-processing

As mentioned in section 5.1 due to the presence of papillary muscle in the LV cavity, accurate segmentation may not result with segments stopping at the papillary muscles or weak boundaries rather than the desired LV wall boundary. Therefore the anisotropic diffusion method (Perona and Malik, 1990) is applied to remove heterogeneity within the blood pool region and also to smooth the LV wall region while preserving the strong boundary.

Perona and Malik proposed the concept of nonlinear diffusion with the selection of a variable diffusion parameter as a function of the gradient of the data:

$$\frac{\partial I}{\partial t} = div(c(x, y, t)\nabla I) = \nabla c \cdot \nabla I + c(x, y, t)\Delta I \qquad \text{5-1}$$

where Δ denotes the Laplacian, ∇ denotes the gradient, div is the divergence operator and $c(x, y, t)$ is the diffusion coefficient. $c(x, y, t)$ controls the rate of diffusion and is usually chosen as a function of the image gradient so as to preserve edges in the image, with the diffusion coefficient of:

$$c\|\nabla I\| = \frac{1}{1 + \left(\frac{\|\nabla I\|}{K}\right)^2} \quad 5\text{-}2$$

where K controls the sensitivity to edges. Figure 5.2 shows a CMR image before and after the reconstruction, where the dark area in the blood pool cavity is seen to be converted to the same intensity level to the blood surrounding it.

(a) (b)

Figure 5.2: (a) Original Image, (b) Filtered Image

5.4 Automatic LV Wall Localization

In automatic LV segmentation it is important to initially localize the LV in order to provide an initialization point for the level set process. In this paper we use the fuzzy based method that we proposed in (Kushsairy Kadir et al., 2010a) for finding the LV centre point (LVCP) of a T_2-weighted CMR image. The technique incorporates the knowledge of the LV position in a CMR image in a fuzzy way to classify a few candidate pixels points as guidance point to initialise the level set. The detection of the centre point is achieved using the knowledge from the observation of a typical SA CMR image. From the CMR image two typical characteristic of the LV are observed: (i) the LV is located a little to the right from the centre of the image plane, and (ii) the blood cavity of the LV appears as a bright area surrounded by a dark myocardial wall. This knowledge is then represented by fuzzy membership functions and the pixel candidates are acquired using a fuzzy logic operator. From the image information three corresponding fuzzy subsets can be represented:

1. Right sided fuzzy centre (RS_{FC})
2. Fuzzy vertical line (F_{VL})
3. Fuzzy horizontal line (F_{HL})

Figure 5.3(a) illustrates the degree of membership element of RS_{FC} where there is no element to the left of the image plane and membership value decreases as the pixel moves away from the centre. Figure 5.3(b) illustrates intensity profile for vertical scanning (F_{VL}) along x axis and horizontal scanning (F_{HL}) along y axis.

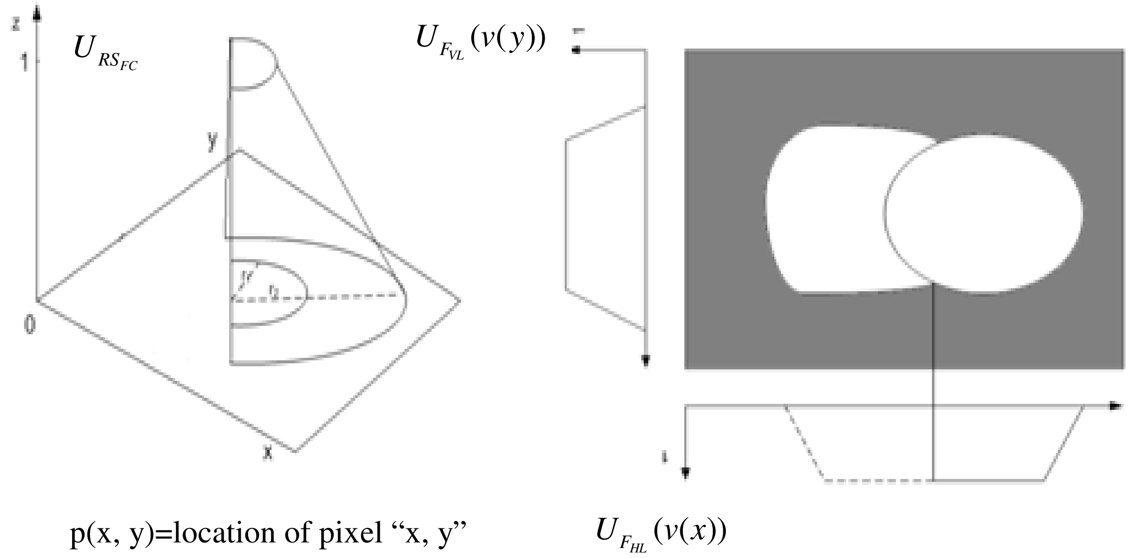

(a) (b)

Figure 5.3: (a) Centre proximity, (b) Intensity profile of the LV.

5.4.1 Spatial information

The process of locating the centre of the LV is performed on a reduced resolution image of (25 x 25) as shown in Figure 5.4(a) which was proposed by (S.K.Setarehdan and J.J.Soraghan, 1997). Figure 5.4(b) illustrates the fuzzy subset of RS_{FC} where the LV blood pool is a bright region which is slightly to the right of the image centre. Thus the potential region for LVCP is defined by a semi circular region (radius = 11) in the image plane. The scale of closeness of the image pixels to the centre of the image place is then represented by:

$$RS_{FC} = \left\{(i,j), \mu_{RF_{FC}}(i,j)\right\}, \quad i,j = 1\ldots25 \qquad 5\text{-}3$$

Highest membership value of unity is given to a region with (radius = 5) representing the region with higher potential and progressively decreasing membership values are used as the pixel distance increases from the right side of the semi circle.

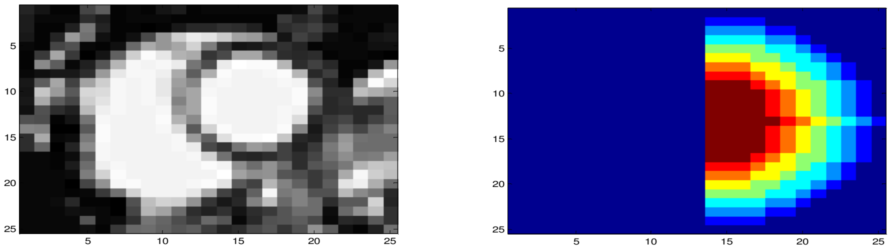

(a) (b)

Figure 5.4: (a) Reduced resolution image (25x25) and (b) Right sided fuzzy centre (RS_{FC})

5.4.2 Intensity information

The operation to generate Fuzzy Vertical and Fuzzy Horizontal rules are performed on the image which is reduced to a resolution of (50 x 50). In order to reduce the computation time significantly and obtain a satisfactory result as suggested by (S.K.Setarehdan and J.J.Soraghan, 1997). Figure 5.5(a) shows the reduced resolution image. Then a vertical scanning is performed by summing up all row pixels, Figure 5.5(b) shows the plot of the summation. Since from the spatial information we know that the LV is to the right of the image plane, thus only the intensity profile to the right is consider as seen in Figure 5.5(c). Then the maximum intensity value (x_c) is located as shown in Figure 5.5(d). Figure 5.5 (e) shows a FVL which is formed with 7 pixels width for a decimated image of (25 x 25). The membership function for FVL is given by (S.K.Setarehdan and J.J.Soraghan, 1997):

$$
\begin{aligned}
&FVL = \{(i,j), \mu_{VL}(i,j)\} \quad i,j = 1\ldots 25\\
&where,\\
&\mu_{VL}(i,j) = f_{VL}(i) = \begin{cases} 1-\dfrac{|i-x_c|}{n} & , \quad |i-x_c| \le 3 \\ \quad 0 & , \quad 3 < |i-x_c| \end{cases}\\
&j = 1\ldots 25 \;\; and \;\; n = number\ of\ fuzzy\ membership
\end{aligned}
\qquad 5\text{-}4
$$

The highest membership value of unity is given to the vertical centre point, progressively decreasing the membership values as distance increases from the centre. The lowest membership value of 0 is given to the pixels other than the 7 pixel width for the FVL.

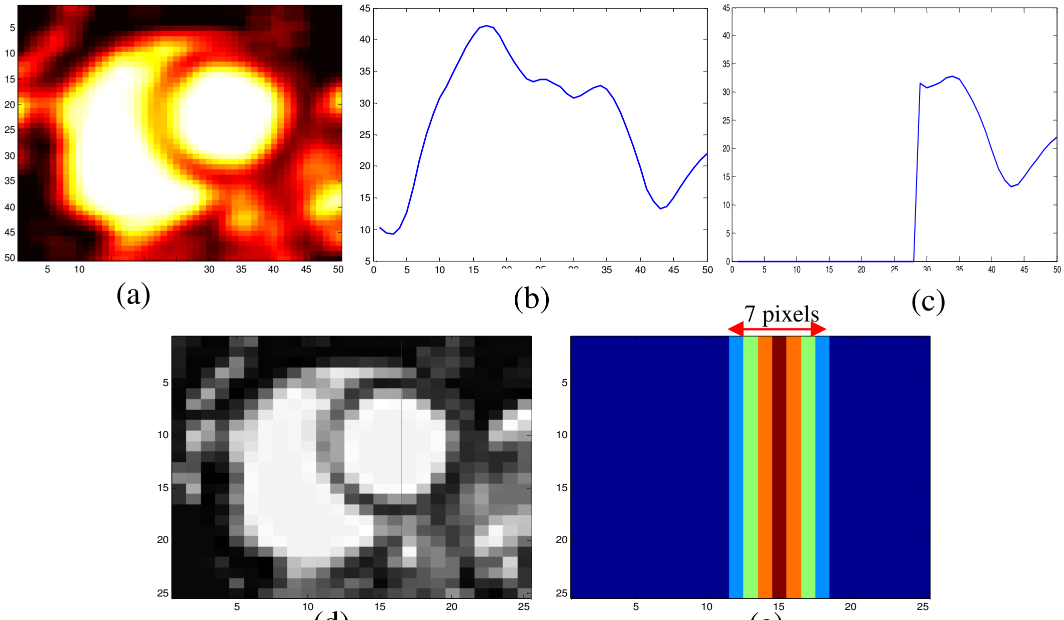

(a) (b) (c)

(d) (e)

Figure 5.5: (a) Reduced resolution image (50x50), (b) Vertical scanning, (c) Right sided vertical scanning, (d)vertical line at (25x25) and (e) Fuzzy Vertical Line (FVL)

The horizontal centre line along (y_c) is determined by multiplying the FVL with (25x25) image as shown in Figure 5.6(a). Horizontal scanning is performed by summing up all column pixels as shown in Figure 5.6 (b). Then a threshold is set at 0.95% of the maximum value, which is determined experimentally to reduce potential y_c points as shown in Figure 5.6(c). Then the first non-zero value ($y1$) and the last non-zero value ($y2$) are located and finally the y_c point is determined from

$\frac{y2-y1}{2}$ as shown in Figure 5.6 (d). Figure 5.6(e) shows a FHL which is formed with 9 pixels width for a reduced image of (25 x 25).

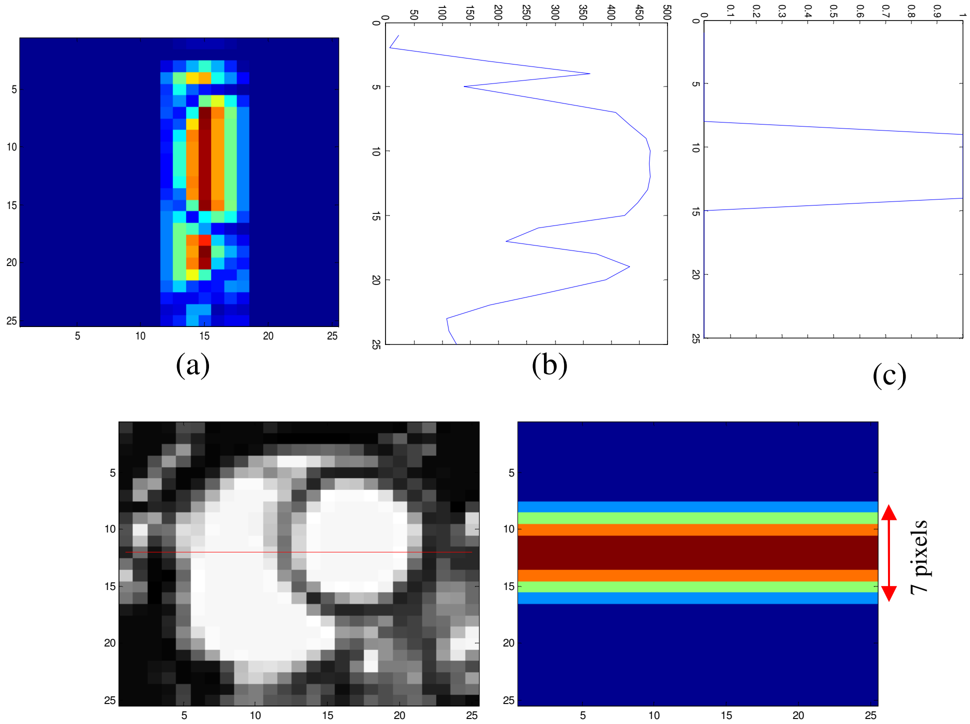

(a) (b) (c)

(d) (e)

Figure 5.6: (a) FVL*Reduced resolution image (25x25), (b) Vertical scanning, (c) Right sided vertical scanning, (d)vertical line at (25x25) and (e) Fuzzy Vertical Line (FVL)

The membership function for FHL is given by [SET, 1998]:

$$FHL = \{(i,j), \mu_{HL}(i,j)\} \quad i,j = 1\ldots 25$$

$$where,$$

$$\mu_{HL}(i,j) = f_{HL}(j) = \begin{cases} 1 & , \quad |j-y_c| \le 1 \\ 1.25 - \frac{|j-y_c|}{n} & , \quad 1 < |j-y_c| \le 4 \\ 0 & , \quad 4 \le |j-y_c| \end{cases}$$

$$i = 1\ldots 25 \;\; and \;\; n = number\ of\ fuzzy\ membership \qquad 5\text{-}5$$

The highest membership value of unity is given to the horizontal centre point and its immediate neighbours, progressively decreasing the membership values (for the 7 pixel width) on either side as distance increases from the centre. The membership value of 0 is given to the other pixel locations.

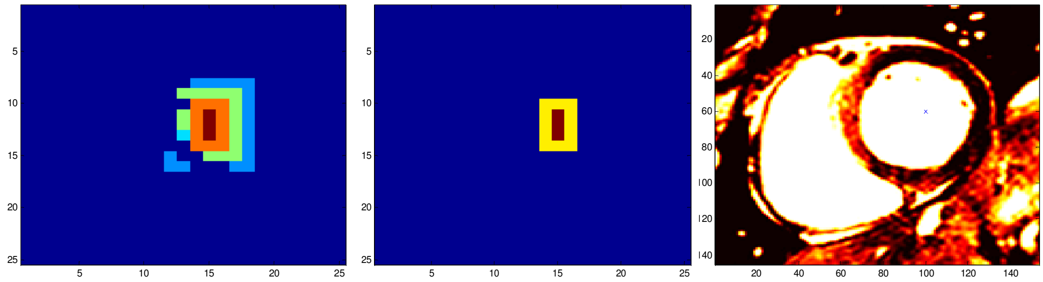

Figure 5.7: (a) $F_{\text{intersect}}$ (FI), (b) f_α and (c) Final centre point

Once the knowledge has been represented in a fuzzy way, the rules are then fed into the fuzzy inference engine by means of the fuzzy 'min' operator to select the minimum of the membership values for each element. It is given by:

$$\begin{aligned} &FI = RS_{FC} \cap FVL \cap FH \\ &\mu_{FI}(i,j) = \min\left(\mu_{RS_{FC}}(i,j), \mu_{FVL}(i,j), \mu_{FHL}(i,j)\right), \quad i,j = 1\ldots25 \end{aligned} \qquad \text{5-6}$$

Figure 5.7(a) illustrates the result of the min operator. Possible candidates for LVCP can be obtained by performing a fuzzy α-cut operation, which is a soft–thresholding method to choose the elements with values greater than the threshold 'α' (approximately). To preserve the relative importance of the pixels, the pixels corresponding to LVCP have membership values between 50% and 90% of the maximum value. The old membership values are translated into new membership values by using a continuous non-decreasing mapping function f_α. The membership values of the fuzzy α-cut of the fuzzy set FI_α is given by (Ahanathapillai, 2010):

$$\mu_{FI\alpha} = f_\alpha(\mu_{FI}(i,j)), \quad i,j = 1\ldots25 \qquad \text{5-7}$$

Figure 5.7(b) illustrates the result of the FI_α operation. The final pixel point is determined by computing the geometric centre of the non-zero $F_{\alpha cut}$. Finally Figure 5.7(c) illustrates the final centre point on the original image.

5.5 LV Wall Segmentation using LSM with Additional Shape Constraint (LSMwASC)

5.5.1 Level set methods (LSM)

The level set method was first presented by Osher and Sethian (Osher and Sethian, 1988) for front propagation, being applied to models of ocean waves and burning flames. Malladi (Malladi et al., 1995) used it for medical imaging purposes.

The central idea is to apply a function $\phi(t,x,y)$ to the space the interface inhabits, where (x,y) is a point in that space, t is the time. The function is initialized at $t = 0$, and then a scheme is used to approximate the value of $\phi(t,x,y)$ over small time increments.

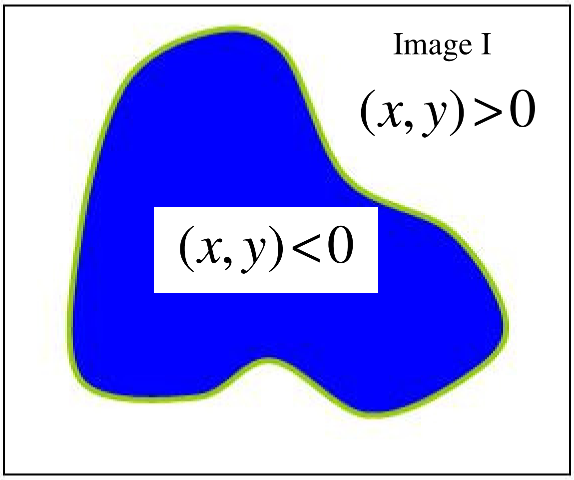

Figure 5.8: Close curve representation of Levet set method

In the implementation a close curve is first placed on an image plane as shown in Figure 5.8. The next step is to initialize the value of $\phi(t,x,y)$ at each point of the image plane. The function $\phi(t,x,y)$ is defined as follows. A point (x,y) in the image plane is given as:

$$\phi(t,x,y) = \pm d \qquad 5\text{-}8$$

which describes the closeness of the point to the boundary (distance function), where (x,y) is the position in the image plane, t is the time and d is the distance between the position (x, y) and the zero level set. The positive sign is used if (x, y) is outside the closed curve; the negative sign is used if (x, y) is inside the closed curve as shown in Figure 5.8, which is also known as signed distance function. Figure 5.9 shows how a closed curve (in this case a circle) can be embedded in a surface.

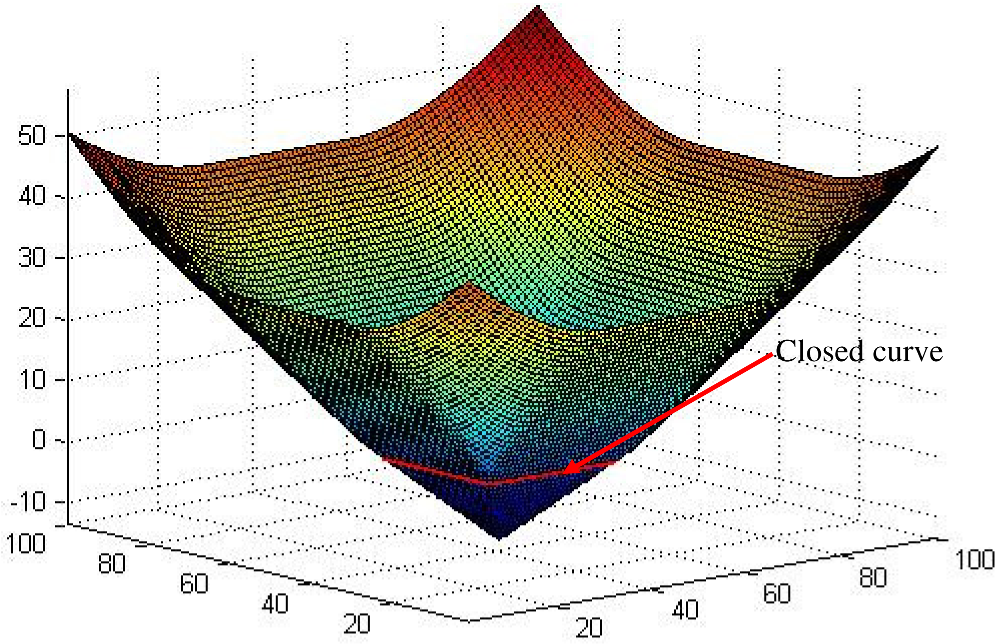

Figure 5.9: Sketch illustrating a circle embedded within a surface

Imagine that this curve/surface moves in its normal direction with a known speed function *F*. The objective is to track the motion of this interface as it evolves on the interface in its normal direction. This speed function *F* can depend on a variety of factors, such as:

$$F = F(L, G) \tag{5-9}$$

where

- L, Local Properties of the curve which are determined by local geometric information, such as curvature and normal direction.
- G, Global Properties of the front, such as image intensity gradient.

An issue with the traditional level set method is that the function $\phi(t,x,y)$ needs to be periodically re-initialised to be a signed distance function to reduce numerical error due to sharpening or flattening effects during the evolution, which is computationally costly. In order to overcome this problem we followed the variational level set method work by Chunming (Chunming et al., 2005) as:

$$\frac{d\phi}{dt} = \underbrace{\mu[\triangle\phi - div(\frac{\nabla\phi}{|\nabla\phi|}]}_{F_{\text{int}}} + \underbrace{\lambda\delta(\phi)div\left(g\frac{\nabla\phi}{|\nabla\phi|}\right) + \nu g\delta(\phi)}_{F_{ext}} \qquad 5\text{-}10$$

where $\mu[\triangle\phi - div(\frac{\nabla\phi}{|\nabla\phi|}]$ is a penalizing term used to maintain the sign distance function of ϕ , $\triangle$ is the Laplacian operator, and $\mu > 0$. The second term in the right hand side of (5.10) corresponds to the gradient flows of the energy functional of weighted length of the zero level curve where $\lambda > 0$ and the third term corresponds to weighted area term where ν can be negative or positive depending on the relative position of the initial contour of the object of interest. Those terms are responsible of driving the zero level curve towards the object boundaries. g is the edge indicator function used to stop the evolution of the level set function at desired boundaries. The edge indicator function is given by:

$$g = \frac{1}{1+|\nabla(G_\sigma * I)|^2} \qquad 5\text{-}11$$

where I is the image data, G_σ is the Gaussian kernel with standard deviation σ and * is the convolution operator. Equations 5.9 to 5.11 forms the basic system of the level set methods used in this work.

5.5.2 Endocardium segmentation procedure

The process to segment the LV wall starts by segmenting the endocardium as illustrated in Figure 5.10.

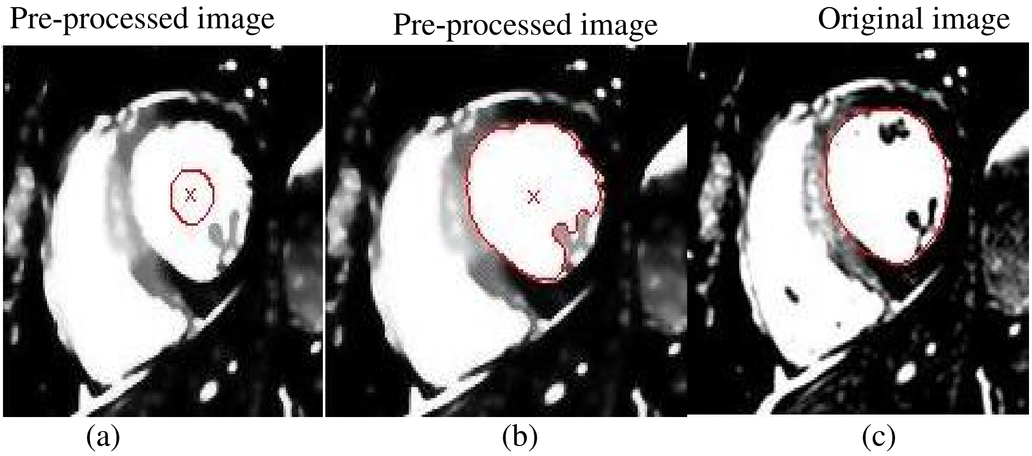

Figure 5.10: (a) Level set initial contour by Fuzzy centre detection (b) detected Endocardium boundary (c) Endocardium boundary on original image

The initial function ϕ_0 is defined as:

$$\phi(x, y) = \begin{cases} -cons & (x, y) \in \Omega_0 - \partial\Omega_0 \\ 0 & (x, y) \in \partial\Omega_0 \\ cons & (x, y) \in \Omega - \partial\Omega_0 \end{cases} \qquad 5\text{-}12$$

where Ω_0 is the sub-image in the image domain Ω, $\partial\Omega_0$ represents the boundary points and $cons$ is a positive constant. The initialization of ϕ_0 can be implemented by creating a mask from the initialization point discussed in section 5.4. The steps for endocardium segmentation include:

i. As indicated in Figure 5.10(a) the initialization and segmentation of the endocardium is carried out on the pre-processed image. The initial LSM ϕ_0 within the LV cavity uses the detected fuzzy centre point as shown in Figure 5.10(a).

ii. The level set function ϕ evolves on the pre-processed image according to equation 5.10, which drives $\partial\Omega_0$ to the endocardium boundary $\partial\Omega_{ENDO}$. The resulting contour is mapped onto the pre-processed image as shown in Figure 5.10(b).

iii. Papillary muscles in the study should be excluded from the LV wall. The convex hull algorithm (Preparata and Hong, 1977) is applied to the final segmentation of the endocardium $\partial\Omega_{Endo}$ to remove the papillary muscles which are especially noticeable from mid ventricle to apical slices as shown in Figure 5.10(c) mapped onto the original image

5.5.3 Epicardium segmentation procedure

Segmentation of epicardium begins with the results of endocardium segmentation as in Figure 5.10(c). The boundary of the endocardium $\partial\Omega_{ENDO}$ is used as the initial contour for the level set function of epicardium segmentation. As shown in Figure 5.11(a), due to the poor contrast between epicardium and surrounding tissue, especially in the anterior region, the direct application of LSM evolves beyond the known real boundary. This is called the leaking problem. Furthermore, segmenting T_2-weighted CMR images in the presence of edema tissue which characterised by a higher intensity than for normal myocardial tissue can result in the LSM trapped at the border of the edema instead of moving towards the epicardium boundary. To overcome these problems the intensity information from the image where the LV cavity and the RV have the highest intensity value compared to the normal LV wall is used. The average intensity value of the LV blood pool can be calculated which, in turn, corresponds to the highest intensity value of the image. Then any value below the value of the blood pool region can be converted into a normal wall region with a designated value. Although this process will help the level set function to ignore the edema, it will make the leaking problem worse.

In order to reduce the overall leaking effects additional constraints are required to successfully delineate epicardium boundary from the presence of edema. Firstly, a new constraint for epicardium segmentation is introduced based on the typical thickness of the myocardial, T_{ave} .

The steps for estimating T_{ave} are as follows:

i. The centroid of the segmented endocardium, $\partial\Omega_{ENDO}$, Figure 5.10(b) is used to form equally distributed radial lines from centre point of LV cavity shown by blue lines in Figure 5.11(b).

ii. The intersection between the radial lines and $\partial\Omega_{ENDO}$ are denoted as P_{endo}. By searching along these radial lines within a certain distance, a set of points are defined as P_{search}. The searching distance needs to be initialized large enough to cover the LV wall region.

iii. The image intensity at lines between P_{endo} and the maximum of P_{search} are assembled into a two dimensional matrix M_{radial} column by column as shown in Figure 5.11(c).

iv. Because the signal intensity of the LV wall and surrounding tissue are lower, and the signal intensity of RV cavity is much higher than other regions, by applying thresholding to M_{radial}, the RV cavity can be detected as the largest and brightest region, as illustrated in Figure 5.11(c). The region over RV cavity is considered to be Septum.

v. The thickness for each radial line in septum region is calculated and T_{ave} is calculated as the mean value for the whole Septum region.

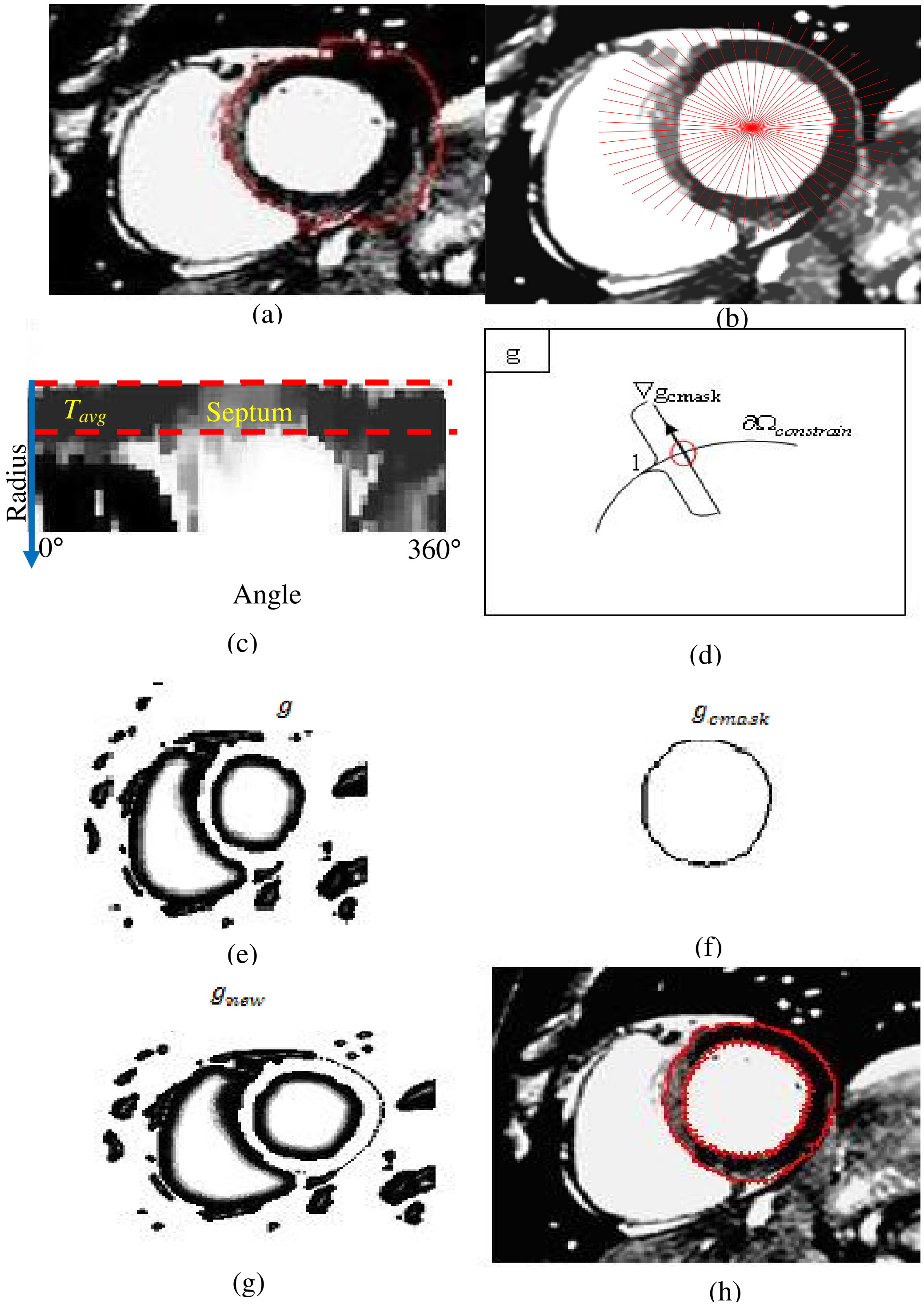

Figure 5.11: (a) detected epicardium boundary without constraint, (b) radial line constructions from the endocardium boundary, (c) graphical illustration of M_{radial} ,(d) Measuring the significant pixels in g (e) Original edge map $\boldsymbol{g}$ (f) Constraint edge map g_{cmask} (g) the newly constructed edge map for epicardium segmentation g_{new} ,(h) segmented endocardium and epicardium boundaries using the LSMwASC.

Secondly a constraint map g_{cmask} is created as follows. Dilating $\partial\Omega_{ENDO}$ outward by T_{ave}, creates $\partial\Omega_{constrain}$. The constraint map g_{cmask} is defined as:

$$g_{cmask} = \begin{cases} 0 & (x, y) \in \partial\Omega_{constraint} \\ 1 & (x, y) \in \Omega - \partial\Omega_{constraint} \end{cases} \qquad 5\text{-}13$$

Thirdly a binary factor f_l is derived that will be used to control the region to which the constraint map, should be applied. Figure 5.11 (d) illustrates a constraint map, and a normal vector to this boundary at a particular point. Integrating g given in equation 5.11, along with this normal over a searching distance l gives a measure of significant pixels that exists around a particular point

$$I_b = \int_{-\frac{l}{2}}^{\frac{l}{2}} g(\bar{r}) * \bar{n} dr \qquad 5\text{-}14$$

where $\bar{n} = \nabla g_{cmask}$, l is the searching distance in pixel passing through the constraint boundary along the normal direction $\bar{n}$. The value of l should be chosen so that the search distance contains the region of LV wall and surrounding tissues but excludes endocardium boundary. A binary function $F_\sigma(t)$ is defined as:

$$F_\sigma(t) = \begin{cases} 1 & if \quad t \le 1/l \\ 1 & if \quad t > 1/l \end{cases} \qquad 5\text{-}15$$

The binary factor f_l is defined as:

$$f_l = E_{indicator} E_{mask} \qquad 5\text{-}16$$

where

$$E_{indicator} = F_\sigma(1 - \frac{I_b}{l}),\; E_{mask} = F_\sigma g_{cmask}$$

and a modified mask g_c can now be defined as:

$$g_c = (1 - f_l) * k + f_l g_{cmask} \qquad 5\text{-}17$$

where,

k= binary mask of ones

If there is no significant edge information in g, then $E_{indicator}$ will be 1, and $g_c = g_{cmask}$ indicating the constraint will be applied to that region. If there is edge information in g, then $E_{indicator}$ will be 0, therefore $g_c = 1$ indicating no constraint will be needed for that region. Finally the new edge map is formed as:

$$g_{new} = g + g_c - 1 \tag{5-18}$$

g_{new} in (5.18) will be in the range of [0 1], which is similar to equation 5.11. The epicardium border will be segmented again with constrained g_{new}, rather than g. Figure 5.11(e) shows the original edge map g used by the LSM to segment the endocardium border while Figure 5.11(f) shows the constraint edge map g_{cmask} and Figure 5.11(g) shows the final edge map g_{new}. The procedure for epicardium segmentation is similar as in endocardium segmentation except for edge map construction. The final segmentation results are illustrated in Figure 5.11(h). It is noted that the overestimation of epicardium in the low contrast regions has been significantly reduced.

5.6 Experimental Results

This section presents the performance analysis of the automatic LV segmentation algorithm using LSMwASC by applying it to real CMR images. In the experiment CMR images from thirty patients who recently experienced myocardial infarction are used. An experienced clinician (IV1) was invited for manual segmentation of LV wall in order to assess the performance of LV wall segmentation using the proposed LSMwASC approach. The manual segmentations from IV1 were used as gold standard for agreement measurement of LV wall boundaries.

5.6.1 LV localization

The success of the automatic system depends on whether the localization algorithm is able to point in the blood pool of the LV. All the tested data-sets have successful results, which mean the point is located within the blood pool region of the LV.

Figure 5.12 shows the result of LV localization of different patients for basal slice, middle slice and apical slice where the centre points are shown on the pre-processed images.

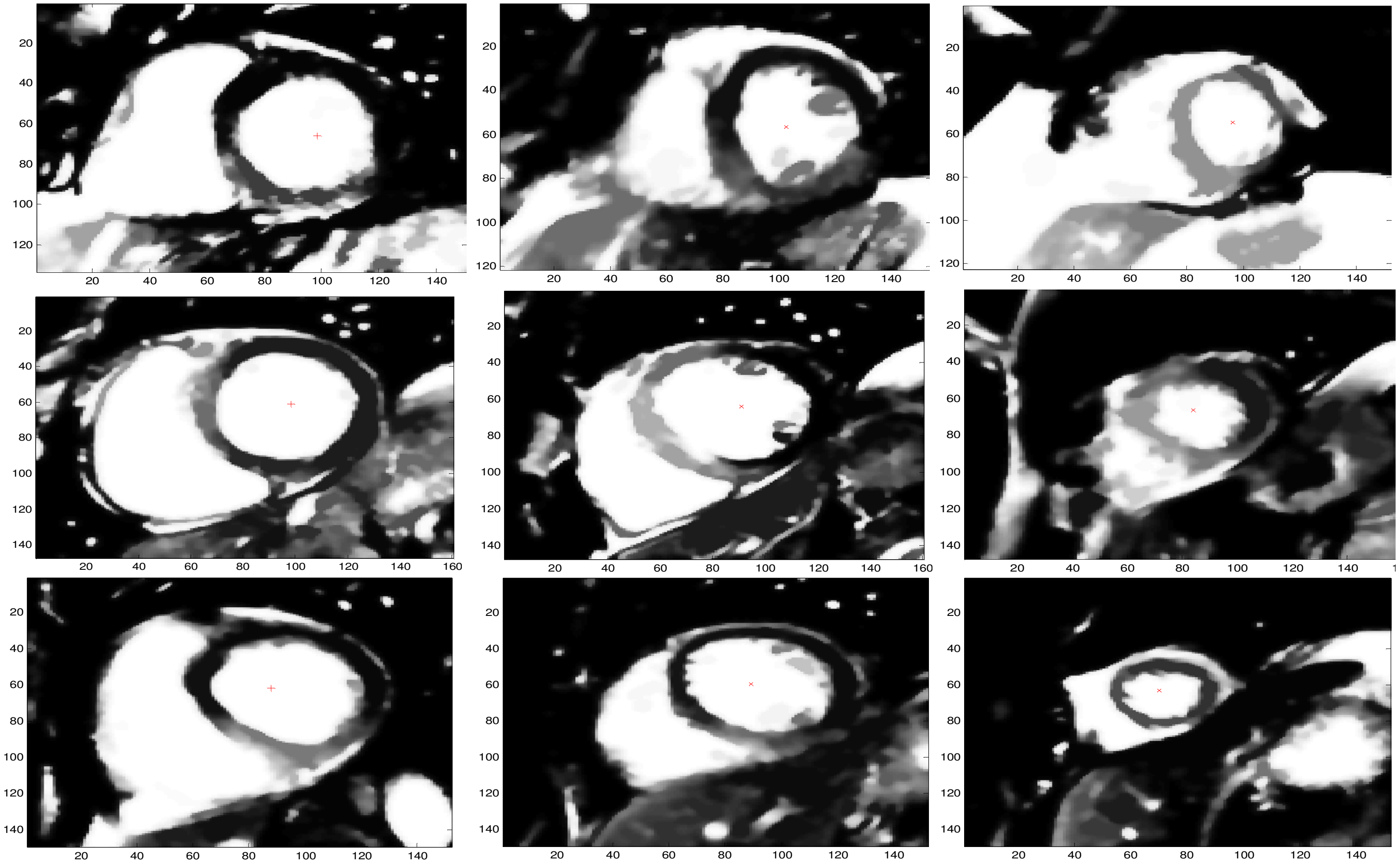

(a) Basal (b) Middle (c) Apical

Figure 5.12: LV localization for three patients

The algorithm is not able to consistently locate the exact centre of the LV because of the variation of image intensity and the shape of the LV especially from the middle slice to apical slice. This is shown in the results on Figure 5.12(a), (b) and (c). Although the centre is not located successfully, the centre is good enough for initialization of the LSMwASC.

5.6.2 LV wall segmentation

5.6.2.1 Parameter selection

When implementing the proposed LSM with additional shape constraint, the time step can be chosen significantly larger than with traditional methods, in order to maintain stable level set evolution. The time step dt and μ from (5.10) should satisfy $dt * \mu < \frac{1}{4}$ (Chunming et al., 2005). In our system the following parameter settings were selected experimentally:- time step $dt = 5$, $\mu = 0.2/dt$, $\lambda = 5$, and $\nu = -3$ for (5.10). In the initialization (5.12) of ϕ_0, the value of $cons$ in (5.12) is chosen to be 4. The iteration numbers are chosen based on the LV wall thickness T_{ave} before level set evolution. The LV wall thickness only needs to be estimated once for one MRI slice of a patient as other MRI slices will use the same value. The iteration number for endocardium segmentation is $10 * T_{ave}$, and $3 * T_{ave}$ for epicardium segmentation. When applying constraints in order to stop the level set evolution, a distance $l = 0.2 * T_{ave}$ is chosen for defining the searching region. All these figures were determined experimentally.

5.6.2.2 Comparison of proposed method with Chunming et al

The segmentation result on a basal slice from the CMR image is shown in Figure 5.13. Qualitatively LSMwASC performed much better when compare to Li et al. The segmentation in Li et al goes beyond the epicardium, which is due to weak edges around the epicardium. In LSMwASC the segmentation stop at epicardium boundary with the help of the additional constraint that prevents the level set to move beyond the thickness of the septum.

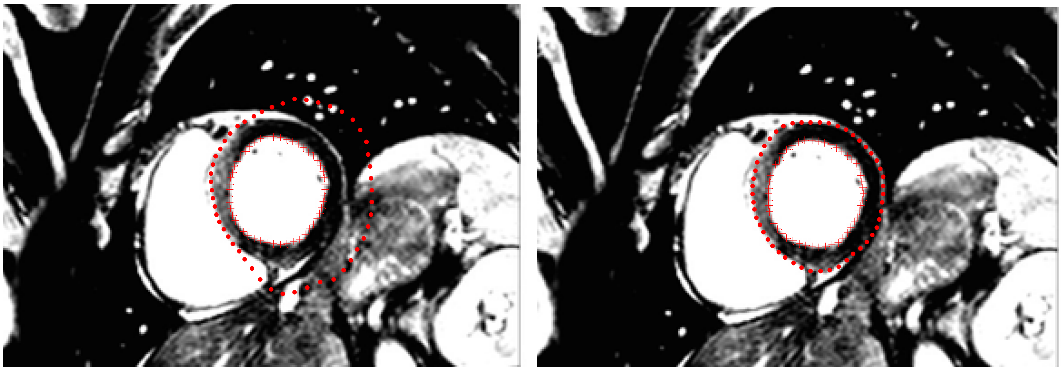

(a) Chungming et al (b) LSMwASC

Figure 5.13: Segmentation result; (a) Li et al, and (b) LSMwASC

5.6.2.3 Qualitative assessment of LV segmentation

The automatic segmentation method is evaluated by comparison with manual segmentations by cardiologists. Figure 5.14 shows the LV boundary segmentation by LSMwASC from base to apex on 6 slices, superimposed with manual segmentation. Qualitatively, the detected LV wall by LSM appears very similar between manual and LSMwASC segmentation, though highly heterogeneous intensity profile can influence the accuracy of LSMwASC, which is due to the existence of edema region.

Figure 5.14(c) plots the endocardium and epicardium boundaries from the automatic segmentation method (identified by “x”, “o”) against manual segmentation method (identified by “x”, “o”) in sample images from basal slice to apical slice respectively. The mean perpendicular distance (MPD) between two boundaries contours was calculated for paired LV boundaries (Petitjean and Dacher, 2011) is used to measure the accuracy of the automatic and manual methods. The average MPD for endocardium boundaries between the manual and automatic segmentations is 0.86 mm and for the epicardium the MPD is 1.4mm. Larger over-estimation is expected for epicardium segmentation, which can be explained by the less contrast information between epicardium and surrounded tissues and the existence of edema on the LV wall.

Further analysis showed that the mean perpendicular distance for 172 slices between the automatic approach and the manual segmented left ventricular boundaries was

1.05±0.4mm for the endocardial boundary and 1.56±0.68mm for the epicardial boundary. The distance was larger on the epicardial wall than on the endocardial wall due to the poorer contrast between epicardium and surrounding tissue. Thus overall the mean perpendicular distance from our approach was comparable to those from other studies on left ventricular wall segmentation accuracy, which is in the range 1-2mm. The average Dice similarity coefficient of the left ventricular wall region was 0.86±0.05 for the 172 slices, suggesting good accuracy for left ventricular wall segmentation with our approach.

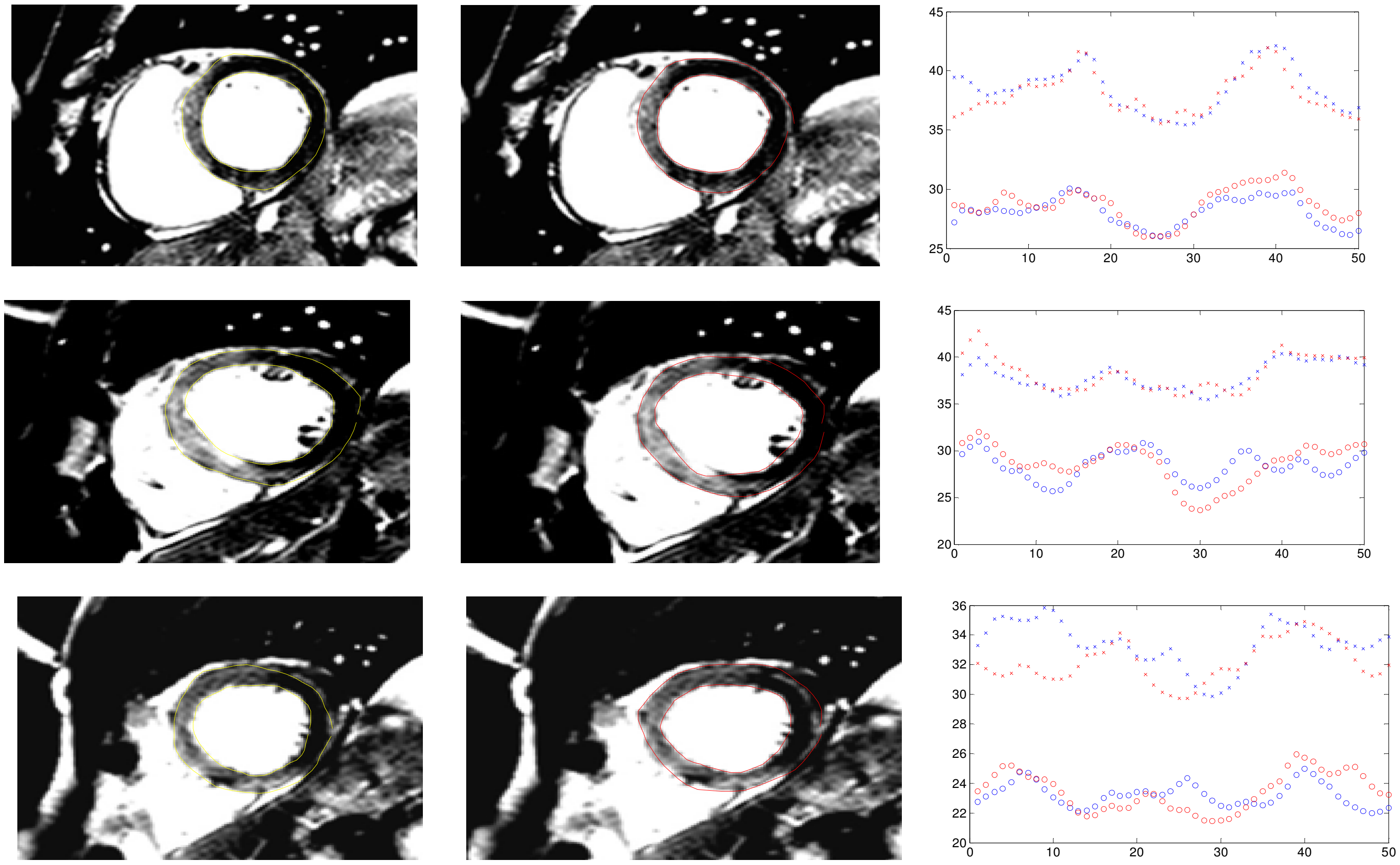

(a) (b) (c)

Figure 5.14: Segmentation result from a single patient from basal, middle and apex (a) Manual Segmentation, (b) Automatic segmentation, and (c) Segmentation difference where (o = endoManual, o = endoAuto, x epiManual, x = epiAuto)

5.6.2.4 Agreement analysis of LV wall area

The correlation analysis between the automatic segmentation and manual segmentation shows they are highly correlated in terms of LV wall area, where $r = 0.868$ as in Figure 5.15 between the manual and automatic, Bland Altman analysis Figure 5.16 shows there is no consistent bias as a function of the LV wall area, with a mean bias of <-23mm^2 between manual segmentation and automatic segmentation, suggesting the automatic segmentation method tends to overestimate LV wall area slightly.

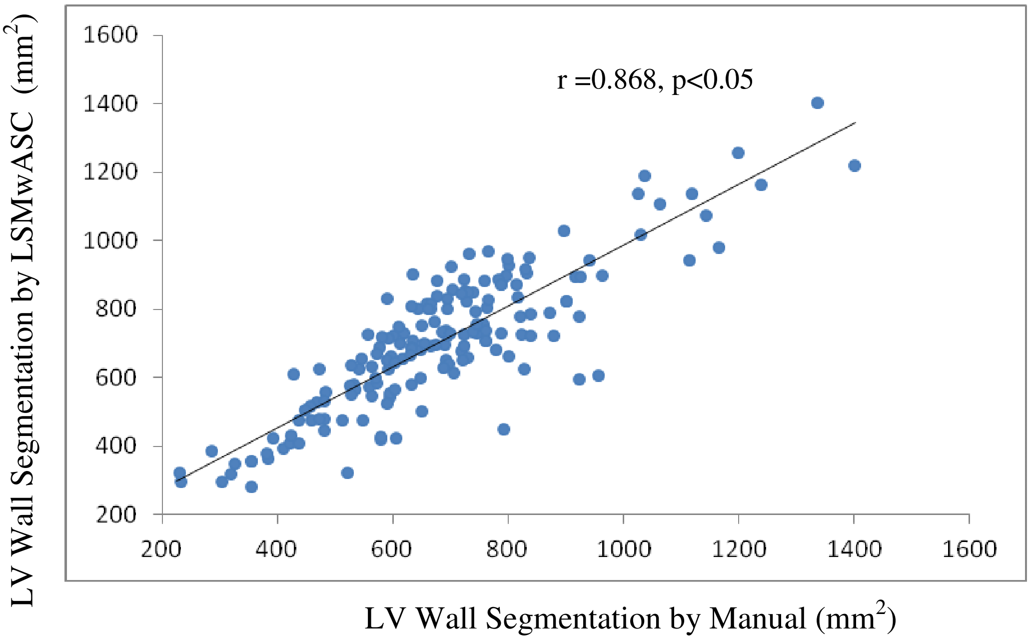

Figure 5.15: Correlation Analysis for 172 slices from 30 patients

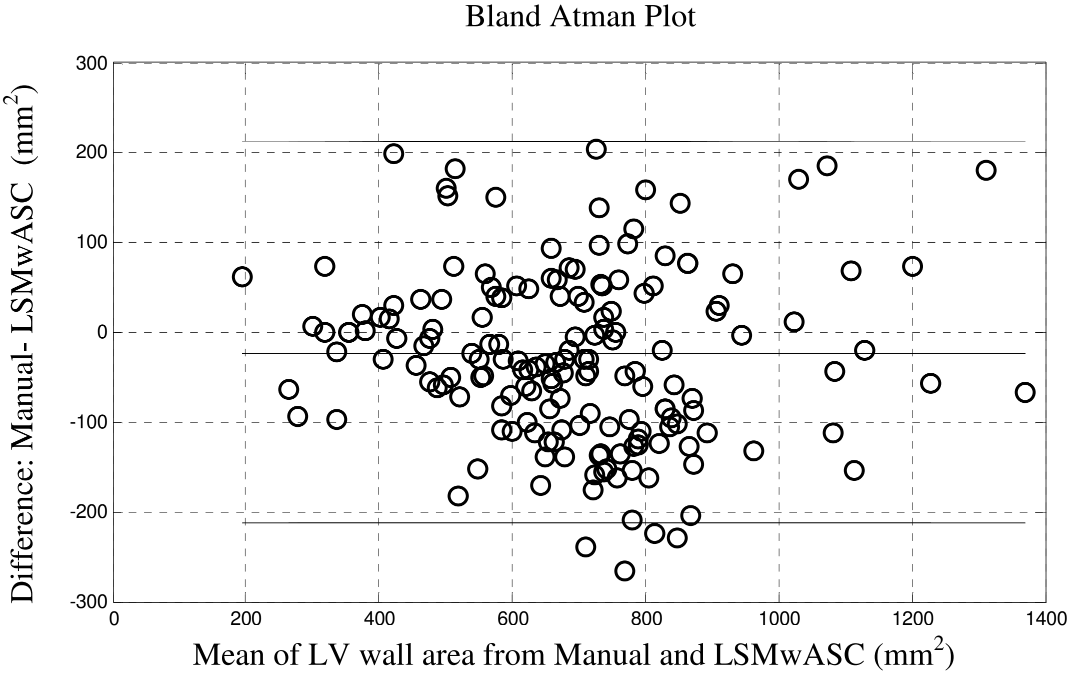

Figure 5.16: Bland Altman Analysis for 172 slices from 30 patients

5.6.2.5 Robust analysis of automatic segmentation method

As the test data are divided into two dataset this provides the opportunity to test the robustness of the algorithm when a new data set is used. Figure 5.17 shows the correlation result of first dataset of CMR images being used. When the correlation result is compared to the correlation result of the second dataset as shown in Figure 5.18 of the CMR images, we can see the reliability in the result where r = 0.895 for the result of the first dataset and r = 0.814 for the second dataset. Two Bland-Altman analyses are performed as shown in Figure 5.19 and Figure 5.20, where both results show no consistent bias as a function of LV wall area, with a mean bias of <-25mm^2 between manual segmentation and automatic segmentation for both datasets.

The experiment shows that the potential adaptability of the proposed LSMwASC when a new dataset is used. This shows the possibility of the LSMwASC to be used in clinical environments.

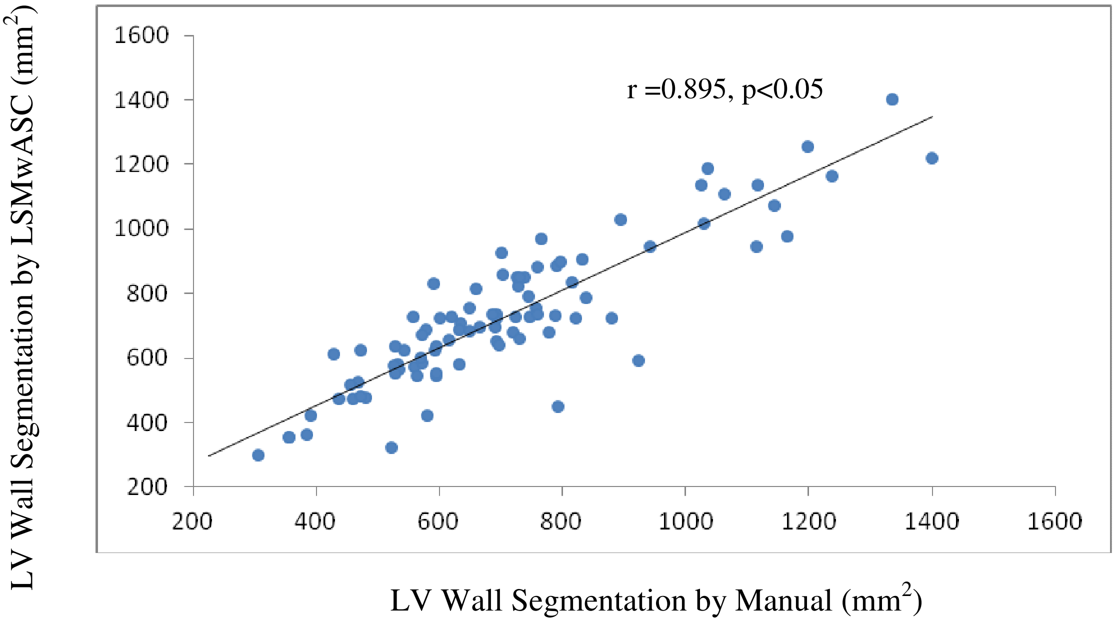

Figure 5.17: Correlation Analysis for First Dataset (90 slices from 15 patients)

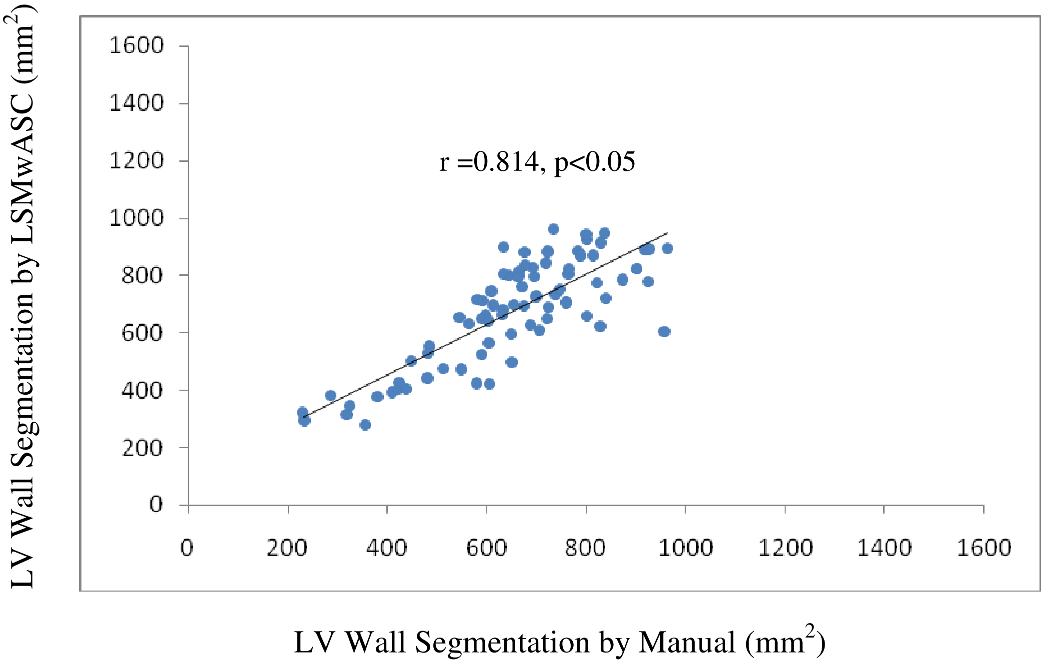

Figure 5.18: Correlation Analysis for Second Dataset (82 slices from 15 patients)

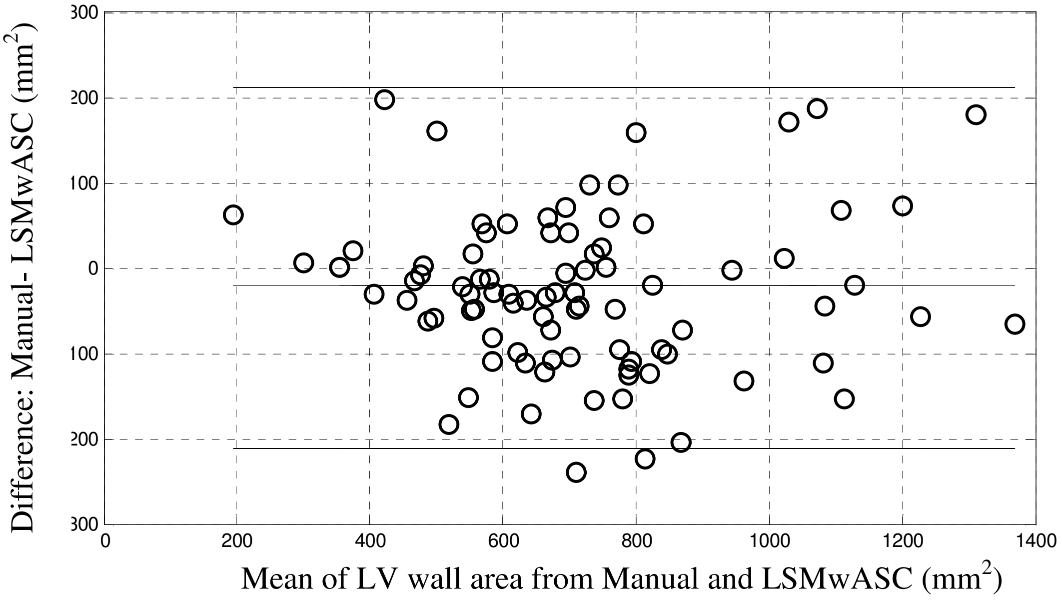

Figure 5.19: Bland Altman Analysis for First Dataset (90 slices from 15 patients)

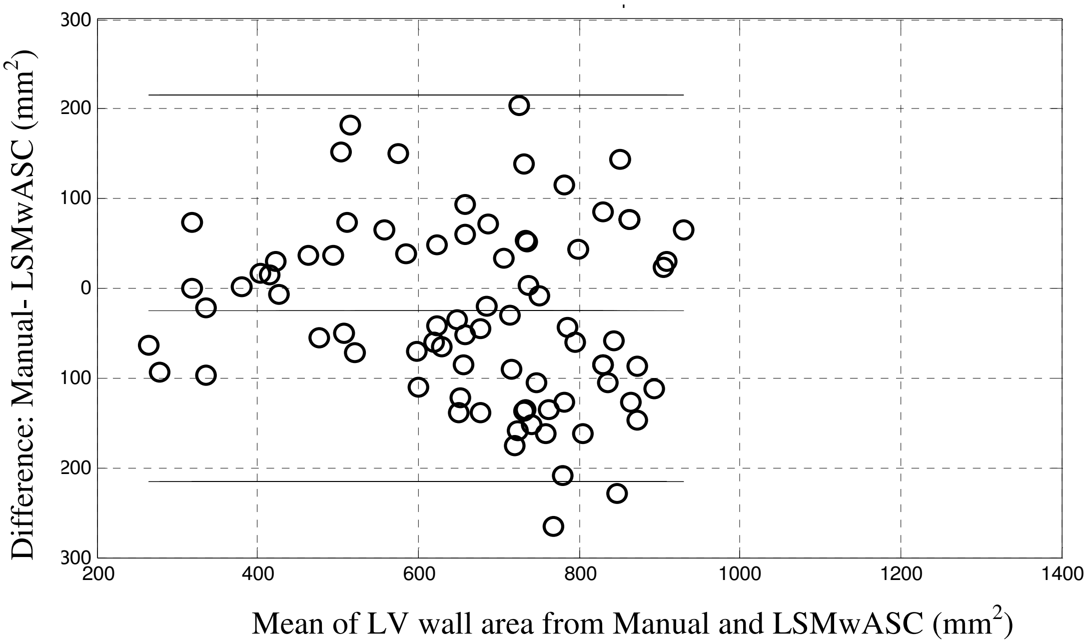

Figure 5.20: Bland Altman Analysis for Second Dataset (82 slices from 15 patients)

5.7 Conclusion

In this chapter, a novel automatic LV wall segmentation method has been presented to segment the LV wall on a T_2-weighted CMR image. The method applied a new

LV localization technique to provide initialization seed for the segmentation of the LV wall. Then LSM has been efficiently implemented with an additional shape constraint to segment the LV endocardium and epicardium.

Performance analysis of this algorithm has been tested on real CMR images. The results are encouraging and suggest that this automatic LV wall segmentation method can be used to help the clinician in speeding up the LV wall segmentation for diagnosing purposes and also as a first stage for automatic edema quantification and 3D visualization.

CHAPTER 6

6. AUTOMATIC EDEMA SEGMENTATION AND QUANTIFICATION

6.1 Introduction

In the previous chapter we introduced the segmentation of the LV wall which is the first step to automatically quantify the edema within the LV wall region. This chapter will present two new algorithms for the segmentation and quantification of edema from T_2-weighted CMR images.

Two Standard Deviation (2SD) methods (Fieno et al., 2000, Setser et al., 2003, Green et al., 2009, Berry et al., 2010, Payne et al., 2011) that are based on statistical criteria have been used widely for the quantification of edema. The disadvantages with conventional 2SD is that they require user interaction first to manually select the LV wall and then the user is also required to select the hyperenhanced region and the normal region for the algorithm to work.

The Hybrid Thresholding Edema Sizing Algorithm (HTOSA) is a fully automatic edema quantification method where the threshold is automatically set based on image intensity histograms, thus removing the requirement for user interaction. It was found that the magnetic resonance image intensity can be modelled by a Rician distribution, which can be approximated by a Rayleigh distribution when intensity values are close to zero, and tends to a Gaussian distribution when values are high (Gudbjartsson and Patz, 1995a). Thus we propose an Automatic Statistical Mixture Model (ASMM) which combines the two distributions for edema segmentation and quantification.

The remainder of this chapter is organized as follows. Section 6.2 introduces the HTOSA algorithm in segmenting and quantifying the edema. In section 6.3 ASMM is presented and discuss of in detail. In Section 6.4 through statistical analysis, we compare the two methods with conventional 2SD and FCM (Baron et al., 2008) from the testing of real CMR images. Section 6.5 concludes the chapter.

6.2 Hybrid Thresholding Edema Sizing Algorithm (HTOSA)

Figure 6.1 illustrates graphically how the Hybrid Thresholding Edema Sizing Algorithm (HTOSA) applied to a series of pre-determined processes to automatically calculate intensity thresholds, performs classification of normal and hyperenhanced region and excludes spurious small positive bright objects on the myocardial wall.

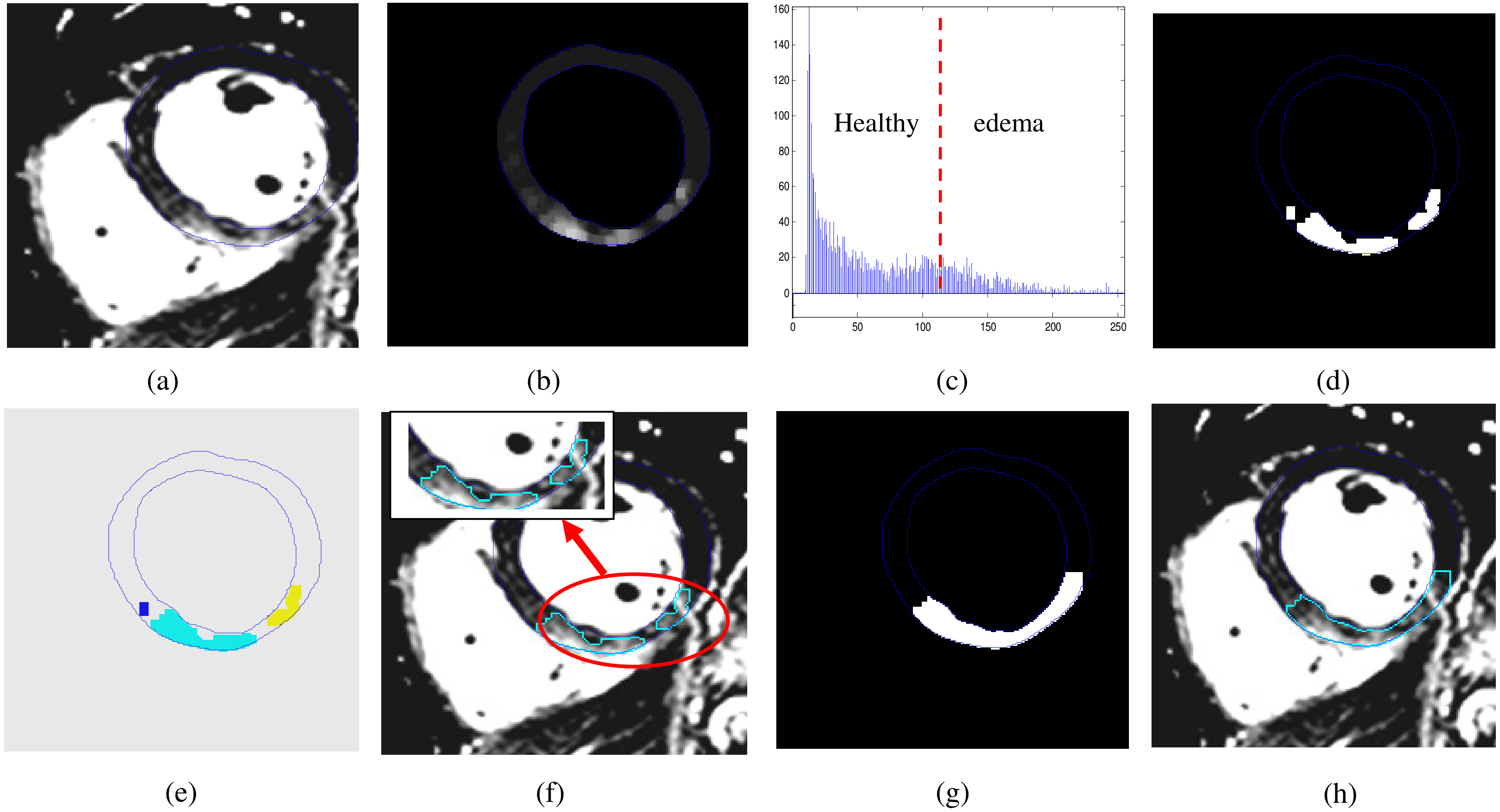

Figure 6.1: Graphical illustration of HTOSA

6.2.1 Image morphological operation

In Figure 6.1(a) the LV wall area is selected from the template of LV wall segmentation. On the LV wall structure the presence of small bright areas in the LV wall increases the difficulty of accurately classifying edema tissue. To reduce the false positive level, morphological filtering is employed that uses an opening operation with a disk shape structuring element to remove small spurious bright regions as in Figure 6.1(b). All bright region having a radius of less than 5 pixels are removed from the myocardial wall. The myocardial wall is then left with bigger bright regions which are most probably edema areas.

6.2.2 2 standard deviation (SD) thresholding

Once the region of interest has been selected, the next step is to calculate the threshold value which determines edema or non-edema. Subsequently an intensity histogram is generated as shown in Figure 6.1(c).

The mean and SD of the normal tissue are first estimated by using the lower part (>50%) of the intensity histogram (Hsu et al., 2006) as illustrated in Figure 6.2. The threshold value is then calculated as 2standard deviation (SD) above the mean. Pixels darker than the threshold are then excluded for further analysis as shown in Figure 6.1(d).

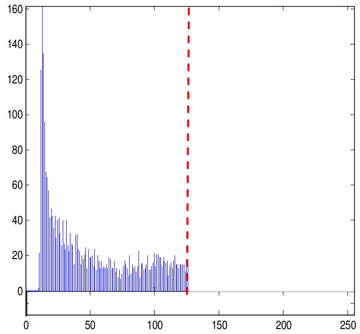

Figure 6.2: Calculating 2SD threshold; histogram >50% of the LV

6.2.3 Microvascular obstruction (MVO) inclusion

Once the threshold has been applied then the remaining region is labelled as shown in Figure 6.1(e) and areas below 50 pixels are removed from the next stage of processing. The remaining potential edema region will be left on the LV wall as in Figure 6.1(f). Then the LV wall is checked for micro-vascular obstruction (MVO). If MVO is present an iterative dilation is then performed to include micro-vascular obstruction (MVO) within the edema region. The steps for iterative dilation are:

```
if Edema area > 1
    counter=1
        for counter = 1:max iteration
                Image dilate=dilate(Image initial)
        end
    Image final= image dilate< image myocardial wall
else
    do nothing
end
```

In Figure 6.1(f) initial edema contour where the algorithm failed to take into account the dark pixel region in between the two edema areas. The iterative dilation is performed as in Figure 6.1(g) to connect the two regions together and finally in Figure 6.1(h) the final edema contour is shown.

6.3 Automatic Statistical Mixture Model (ASMM) for Edema Segmentation and Quantification

A high level overview of the automated edema segmentation and quantification algorithm is shown in Figure 6.3. First CMR image stack is obtained. Then the LV wall region is segmented and the LV ROI mask is created. The automated segmentation and quantification can then be performed. The system consists of Statistical Mixture Model (SMM) thresholding and post-processing step which includes Morphological filtering and Region Feature Analysis for MVO inclusion. These stages in the algorithm are discussed in detail in the following sections.

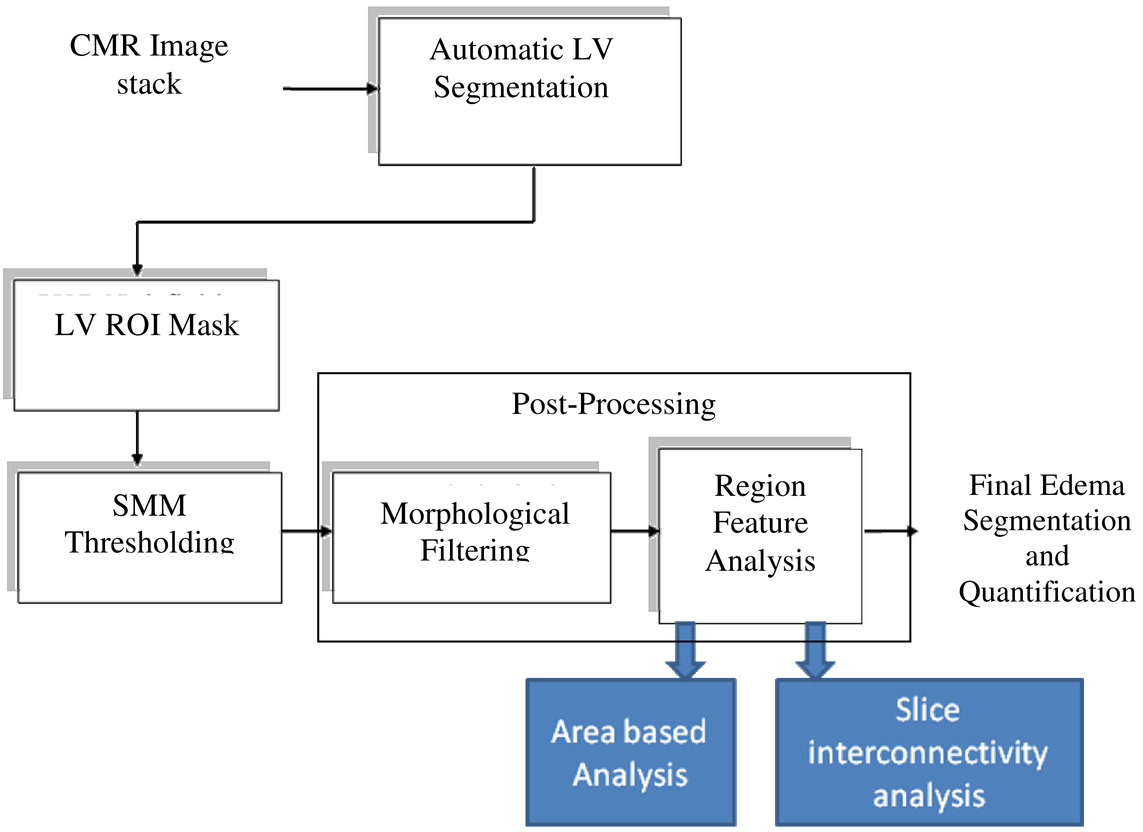

Figure 6.3: Edema Segmentation and Quantification Algorithm

6.3.1 Automatic LV wall segmentation

The LV wall boundary is segmented by the Level Set Method as explained in Chapter 4. This technique comprises of:

- An Automatic LV Wall localization (as describe in section 5.4)
- A Level Set Method with Additional Shape Constraint (LSMwASC) to segment the endocardium and epicardium of the LV wall (as describe in section 5.5).

Once the LV boundaries are segmented, the information can be used to create the LV region of interest (ROI) for the segmentation and quantification of the edema.

6.3.2 Statistical mixture model

In an axial image obtained with T_2-weighted MRI, as shown in Figure 6.4(a), the normal tissue appears dark while the edema tissue appears bright.

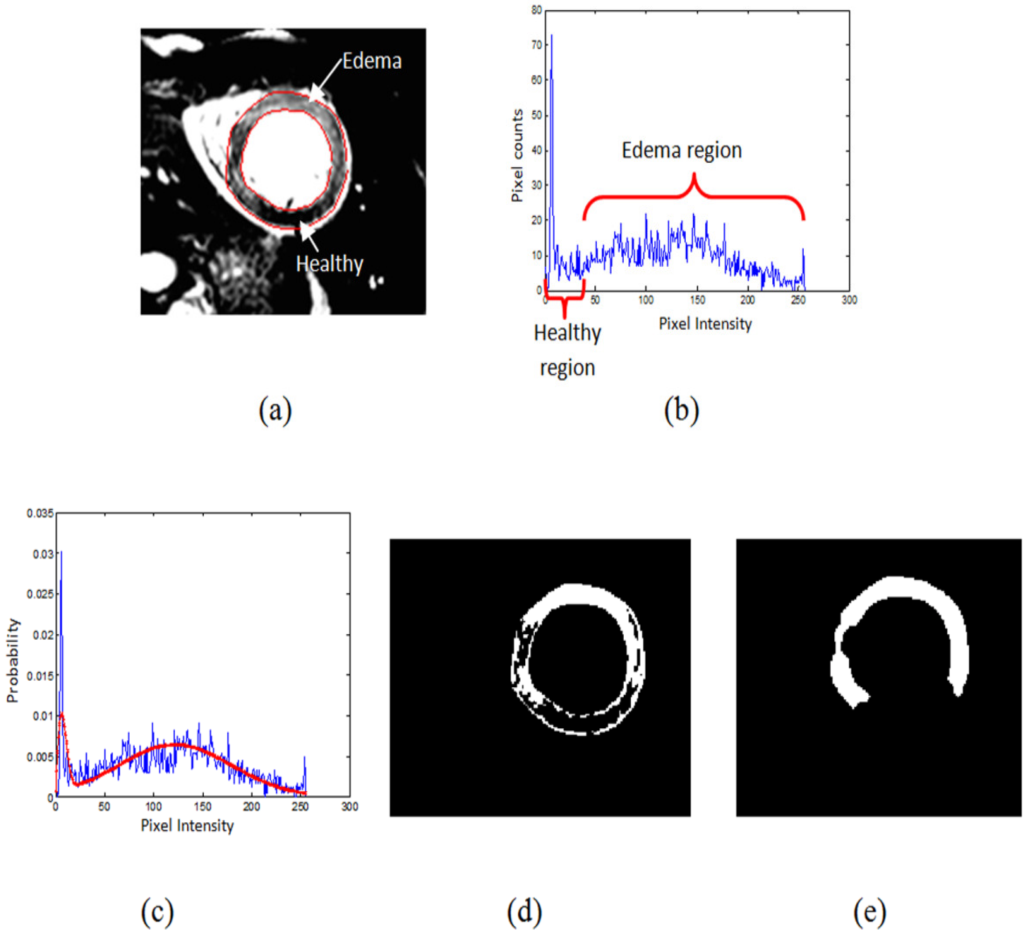

Figure 6.4: (a) Edema Imaging with LV Wall Boundary, (b) LV Wall Intensity Distribution, (c) The fitting of Rayleigh-Gaussian Mixture Model, (d) Thresholding process, (e) Morphological Filtering

Figure 6.4(b) shows the corresponding histogram of the image. In the presence of noise, the magnetic resonance image intensity is governed by a Rician distribution, which can be approximated by a Rayleigh distribution when intensity values are close to zero, and tends to a Gaussian distribution when values are high (Gudbjartsson and Patz, 1995a). Therefore it is possible to represent the normal and pathological tissues by using Rayleigh and Gaussian distributions with a percentage error of approximately 3.5% and 5% respectively (Aquaro, 2010, Chung, 1999). In order to fit a Rayleigh-Gaussian mixture to the image histogram for the hyperintense region of interest in the left ventricular wall, the intensity distribution function f_{myoc} for myocardium is defined as follows (Elagouni et al., 2010) :

$$f_{myoc}(I) = a_n \cdot f_n(I + \alpha_{shift}, \sigma_n) + a_e \cdot f_e(I, \mu_e, \sigma_e) \qquad \text{6-1}$$

$$f_n(I, \sigma_n) = \frac{I}{\sigma_n^2} e^{-\frac{I^2}{2\sigma_n^2}}, I \geq 0 \qquad \text{6-2}$$

$$f_e(I, \mu_e, \sigma_e) = \frac{1}{\sqrt{2\pi\sigma_e^2}} e^{-\frac{(I-\mu_e)^2}{2\sigma_e^2}} \qquad \text{6-3}$$

Equation (6.1) is the Rayleigh-Gaussian mixture model while equations (6.2) and (6.3) represent the Rayleigh and Gaussian distributions respectively. a_n and a_e are the weighting parameters for the two models; σ_n is the Rayleigh distribution parameter; μ_e and σ_e are the mean and standard deviation of the Gaussian distribution; I stands for myocardium intensity in left ventricular wall. α_{shift} represents the intensity shift during the MRI acquisition and the intensity adjustments which resulted from the procedure to make the healthy myocardium as dark as possible for maximizing contrast and the identification of bright edematous myocardium during the MRI acquisition and image screening. The estimation of the distribution parameters is achieved by maximizing the likelihood according to the myocardium intensity histogram with an Expectation Maximization algorithm (EM) (Dempster AP, 1977). In Figure 6.4(a), the left ventricular wall intensity distribution is seen to fit well with the Rayleigh-Gaussian mixture model. Once the fitting has been done, the distributions are then exploited to generate threshold value, which defines normal or edema tissues. The operation to generate the threshold values is:

1) Calculate the mean of the Rayleigh distribution is

$$u_n = \sigma_n \sqrt{\frac{\pi}{2}} \tag{6-4}$$

2) A fuzzy membership map I_{map} is then defined according to u_n and μ_e as:

$$I_{map} = \begin{cases} 0, & I \le u_n \\ \dfrac{I - u_n}{u_e - u_n}, & u_n < I < u_e \\ 1, & I \ge u_e \end{cases} \tag{6-5}$$

For each pixel, if intensity value I is less than u_n, then the pixel belongs to healthy myocardium, and $I_{map} = 0$; if I is greater than u_e, then belonging to edema tissue, and $I_{map} = 1$; I_{map} varies linearly from u_n to u_e.

In this study, a membership value of $I_{map} \ge 0.7$ was defined as the threshold value for the region with edema. The value of 0.7 was chosen by experimental validation which matched manual edema delineations as discuss in section 6.4.5.

6.3.3 Post-processing

6.3.3.1 Morphological operation

After thresholding, segmented regions of myocardial edema were performed with an alternative sequential morphological filtering which is a robust approach to preserve topology (Couprie and Bertrand, 2004). Sequential morphological filtering includes the following three steps:

i) a morphological closing operation with a small kernel (disk shape with size of 2 pixels) for removing the noise and false positives;

ii) an opening process with the same kernel as in the first step;

iii) a closing process with a bigger kernel (disk shape with size of 5 pixels) was applied to connect isolated regions if close enough.

6.3.3.2 Region feature analysis

Area based analysis: However due to imaging intensity variations, small bright regions may occur in a normal myocardium. Bright areas such as these or others are due to inaccurate left ventricular wall boundary segmentation, as shown in Figure 6.5 (c). The segmented regions in Figure 6.5(c) were labelled using 8-neighbor connectivity analysis and the largest hyper-intense region was considered to be the main area of injury. As in Figure 6.5(c), except for the main edema region, three other regions in the side opposite to the main edema region are identified. Therefore additional analysis is required to check if these regions should be considered to be edema according to their relative size and the arc distance to the main edema region. The arc distance from one of these regions to the main edema region is defined in degrees according to the left ventricular cavity centre, as shown in Figure 6.5(c). In line with the approaches used for segmentation in previous studies (Hsu et al., 2006, Johnstone et al., 2011), our area based analysis procedure is:

- The region is considered to be edema if the area of the region is greater than two fifths of the main edema region.
- The region is considered to be edema if the area of the region is one fifth to two fifths of the main edema region, and the arc distance from the region to the main edema region is less than 20°;
- The region is taken to be healthy myocardium if the area of the region is less than one fifth of the main edema region, and the arc distance from the region to the main edema region is greater than 10 degrees.

Figure 6.5(d) shows an example of the final result of the edema region (enclosed by the red line) after the area feature analysis based on the edema image in Figure 6.5(a), superimposed with manual segmentation (enclosed by the blue line).

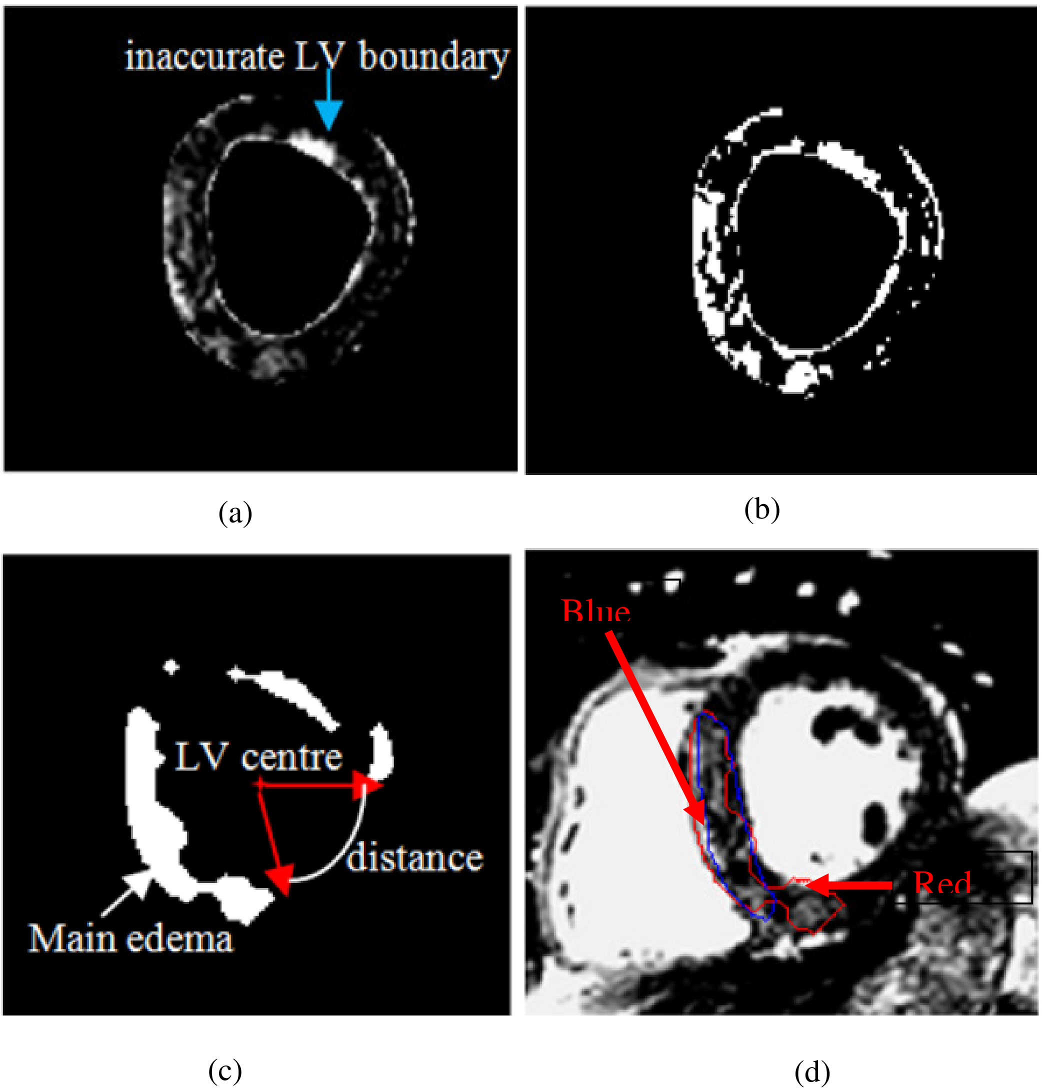

(a) (b)

(c) (d)

Figure 6.5: (a) The LV Wall segmentation; (b) Edema Delineation after Thresholding; (c) Edema Delineation after Morphological Filtering; (d) Final Edema Delineation after Edema Region Feature Analysis (enclosed by red line) Superimposed by the Manual Delineation (the blue line).

Slice interconnectivity analysis: In manual segmentation of the edema, MVO is included into part of the edema region. If the clinician is in doubt about the MVO region, the clinician will refer to the previous slice to verify whether the MVO is present in the current slice. This motivates us to implement the technique automatically. We introduce a decision making process by checking on the slice before the current slice to check whether the area is a microvascular obstruction (MVO) or normal. The process is as follows:

1. Convert the image into a polar image
2. Calculate the distance between edema regions

Figure 6.6(a) show a Cartesian image, the image is then transformed into polar images as shown in Figure 6.6(b) and Figure 6.6(c). From the test data two conditions are found when the image is converted into polar image:

- Case 1: Where the start point (M1) and the end point (M4) of edema regions does not touched the start of the of the sampling point from Cartesian image to polar image the condition is shown in Figure 6.7
- Case 2 where the body of edema regions touched the start point and end point of the sampling points from Cartesian image to polar image as shown in Figure 6.8 where MI to M2 touched the starting point.

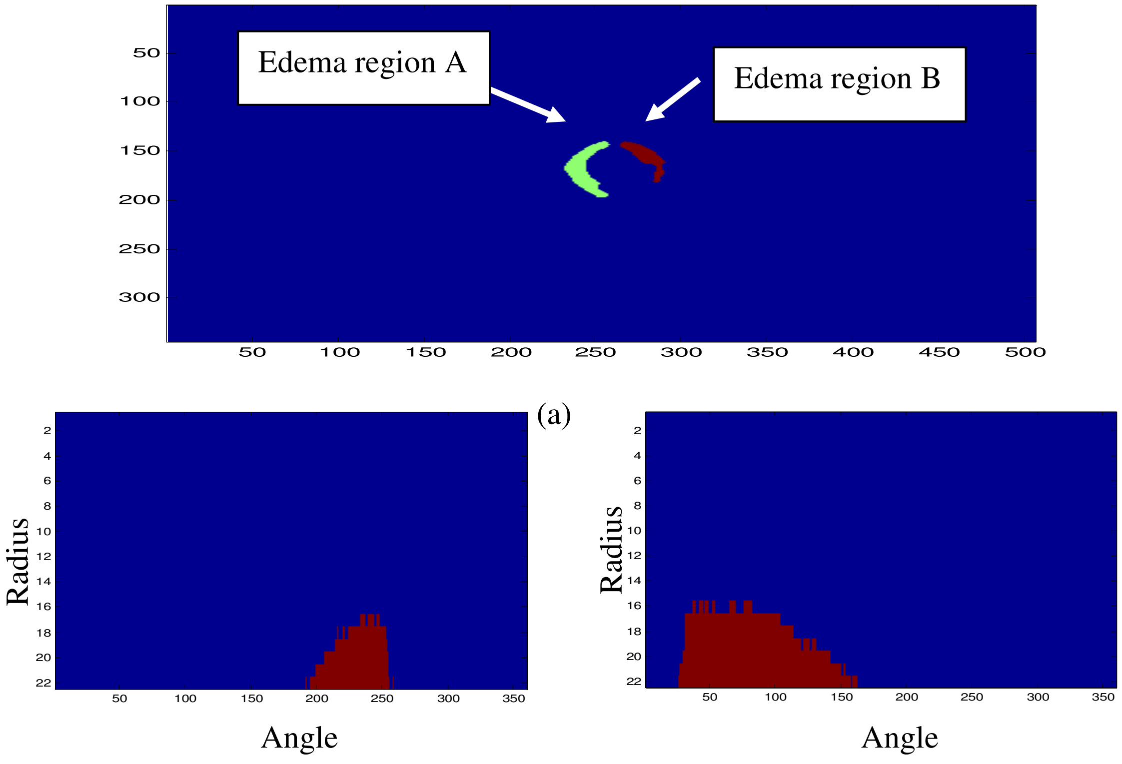

(a)

(b)

(c)

Figure 6.6: Conversion from a cartesian image to a polar image; (a) Binary image, (b) and (c) polar images

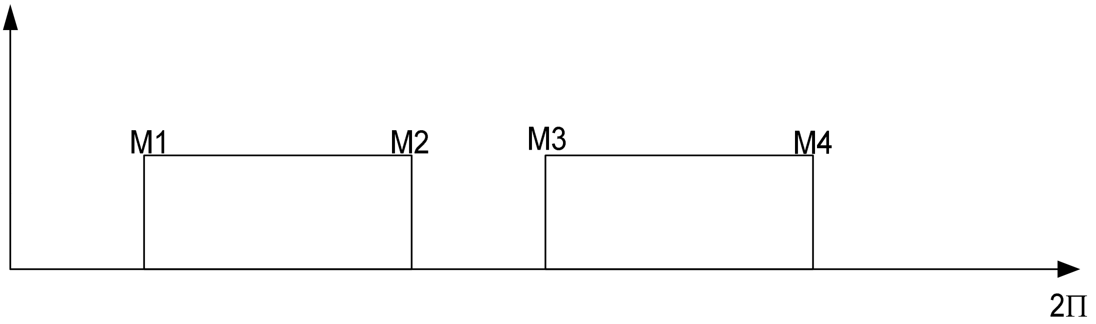

Figure 6.7: Radial search rule for case 1

$$d_1 = M_3 - M_2 \qquad d_2 = (2\pi - M_4) + M_1$$

Thus

$$d_{c1} = \min(d_1, d_2) \tag{6-6}$$

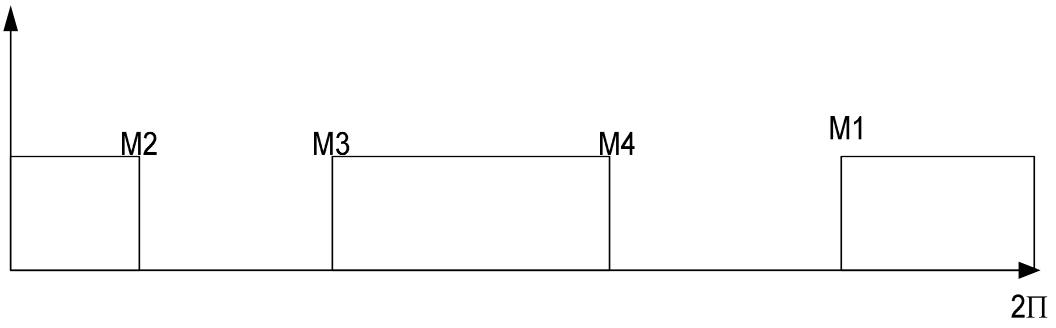

Figure 6.8: Radial search rule for case 2

$$d_3 = M_3 - M_2 \qquad d_4 = M_1 - M_4$$

Thus

$$d_{c2} = \min(d_3, d_4) \tag{6-7}$$

The main idea of this process is to determine the distance between the two edema bodies and use the information to adapt the structuring element for a morphological closing operation as shown in Figure 6.9.

```
Case 1
    • Calculate Ms=start of edema from previous slice and Me=end of edema from previous slice
    • Loop
    • If M2>Ms&M3<Me
    • Merge the two region using morphological closing with strel $d_{c1}$
    • else
    • end loop
```

```
Case 2
    • Calculate Ms=start of edema from previous slice and Me=end of edema from previous slice
    • Loop
    • If M4>Ms&M1<Me
    • Merge the two region using morphological closing with strel $d_{c2}$
    • else
    • end loop
```

Figure 6.9: pseudo code

The process starts by checking the previous SA image slice. The start location (Ms) and the end of edema location (Me) are marked. Then the edema locations (M2) and (M3) for case 1 or (M4) and (M1) for case 2 on the current SA image slice are checked. Once the MVO has been determined a morphological closing is performed with an adaptive structuring element the size of d_{c1} or the size of d_{c2}. Figure 6.10(a) shows the automatic contouring with two edema regions whereas the clinician considers this as one big edema area. Figure 6.10(b) shows the result of slice connectivity algorithm. It can be seen from this figure that the two edema regions have been merged.

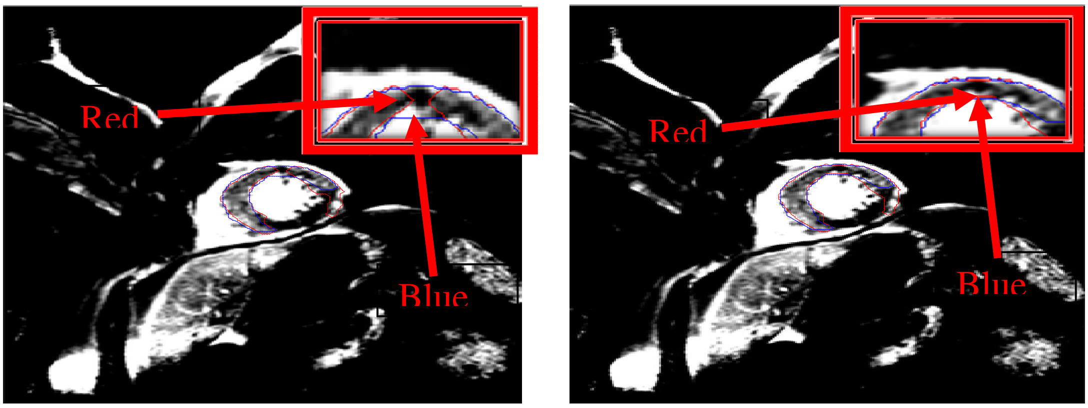

Figure 6.10: (a) Before slice connectivity analysis, (b) After slice connectivity analysis; (blue) manual contouring, (red) automatic contouring

6.4 Experimental Result

In this section the experimental results for the algorithms are presented. The two algorithms HTOSA and ASMM are compared with conventional 2SD method and FCM method. Since there is no standard measurement to compare the performance of the algorithms, a clinician is invited to manually segment the edema region and this segmentation is used as the gold standard.

6.4.1 Qualitative validation

Figure 6.11(a, b, c) shows example results of the four methods on basal, mid ventricle and apical locations superimposed on the manual edema segmentation, respectively. Qualitatively the detected edema areas between the four methods appear very similar.

Figure 6.11 a(v), b(v), and c(v) show the edema difference between the automatic methods and manual results. From the results it can be seen that the performance of the ASMM is consistently better compared to the other methods with mean difference of 1.586± 0.37%, 2SD of 9.49± 2.13%, FCM of 5.2± 7.61% and HTOSA of 9.08± 2.60%.

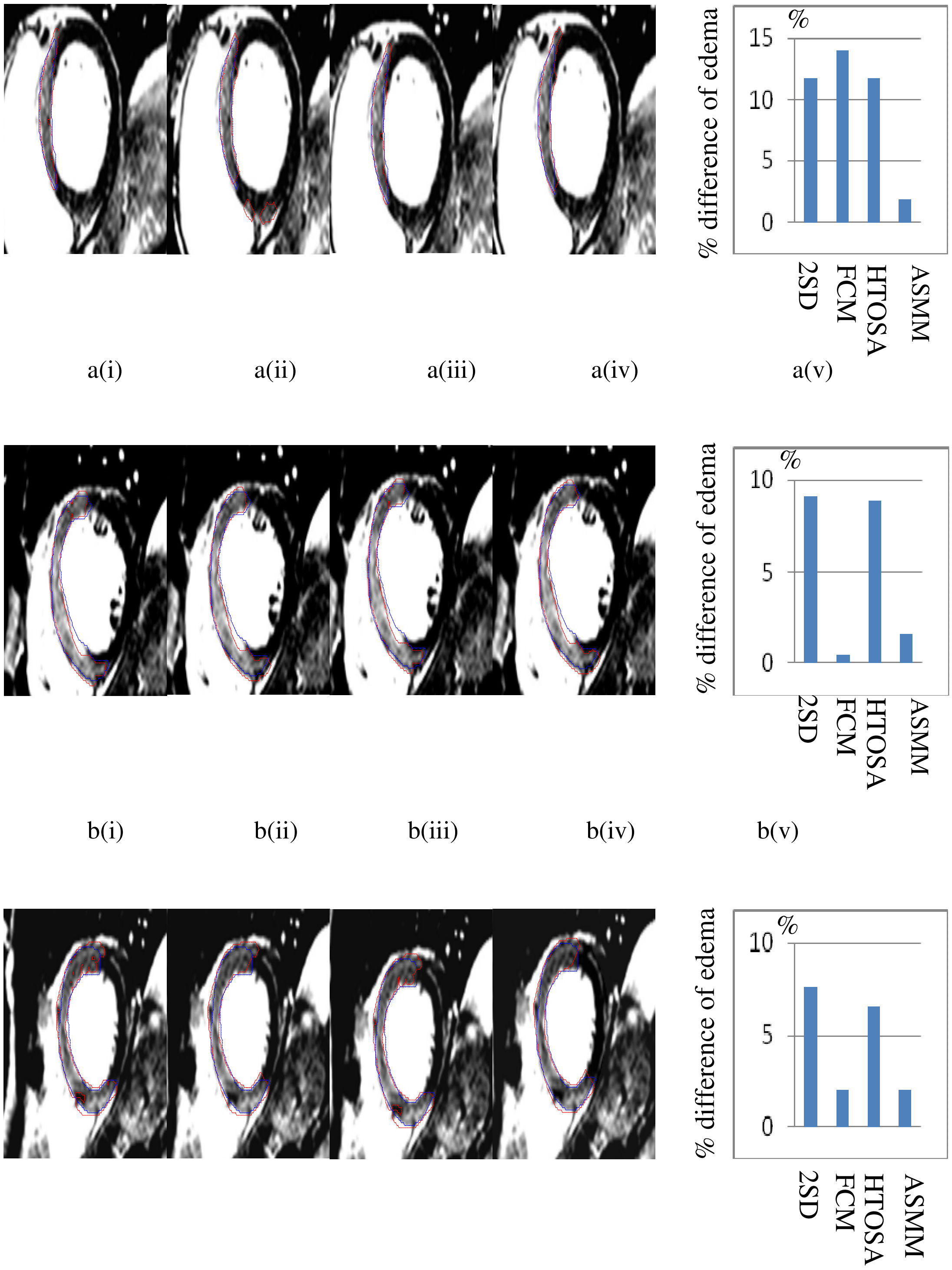

a(i) a(ii) a(iii) a(iv) a(v)

b(i) b(ii) b(iii) b(iv) b(v)

c(i) c(ii) c(iii) c(iv) c(v)

Figure 6.11: Example Segmentation of Edema Area on Three Slices (a) Basal, (b) Mid-ventricle and (c) Apical by (i) 2SD, (ii) FCM, (iii) HTOSA and (iv) ASMM; (v) % Difference for the Four Methods; (blue) Manual and (red) Automatic

6.4.2 Agreement analysis

This section presents quantitative experimental results and discussion on the performance of ASMM and HTOSA compared with the conventional 2SD and FCM methods. Manual segmentation by a clinician is used as gold standard to compare the performance of the four algorithms. Table 6-1 represents the linear correlation analysis among the four automatic methods and the manual result. ASMM has the highest linear relationship ($r=0.75$, $p<0.05$) among the four methods. The HTOSA has values ($r=0.70$, $p<0.05$) and the FCM has values ($r=0.69$, $p<0.05$). The 2SD is the poorest method with values ($r=0.66$, $p<0.05$). Bland-Altman analysis is performed to measures the mean bias and the agreement between two segmentation methods by using the average of two measures (A, *manual method and B, automatic methods)*. Figure 6.12 which shows Bland-Altman analysis for Manual-ASMM with a negative bias of (-3%), Figure 6.13 shows Bland-Altman analysis for Manual-HTOSA with a negative bias of (-8%), Figure 6.14 shows Bland-Altman analysis for Manual-2SD with a negative bias of (-8%) and Figure 6.15 shows Bland-Altman analysis for Manual-FCM with a negative bias of (-5%).

Another measure to determine the performance of the proposed method is DSC, which is used to measure the degree of overlapping between the manual segmentation and the four methods. The DSC is schematically summarized with a box plot as shown in Figure 6.16, which shows that ASMM gave highest DSC value of overlapping with an average value of 0.70 ± 0.11, DSC= 0.64 ± 0.13 for HTOSA, DSC= 0.68 ± 0.12 for FCM, and DSC= 0.61 ± 0.15 for 2SD.

Table 6-1: Correlation Analysis for Edema Quantification

	Manual	2SD	FCM	HTOSA	ASMM
Manual		r =0.66	r =0.69	r =0.70	r =0.75
2SD	r =0.66		r =0.91	r =0.86	r =0.62
FCM	r =0.69	r =0.91		r =0.82	r =0.77
HTOSA	r =0.70	r =0.86	r =0.82		r =0.66
ASMM	r =0.75	r =0.62	r =0.77	r =0.66	

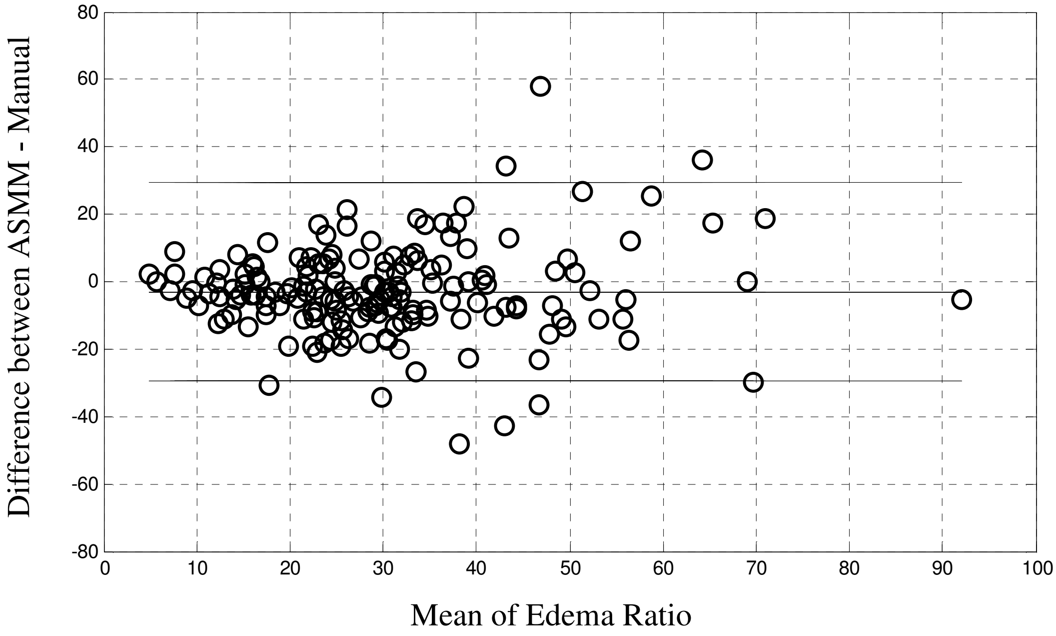

Figure 6.12: Bland-Altman Analysis of Manual- ASMM

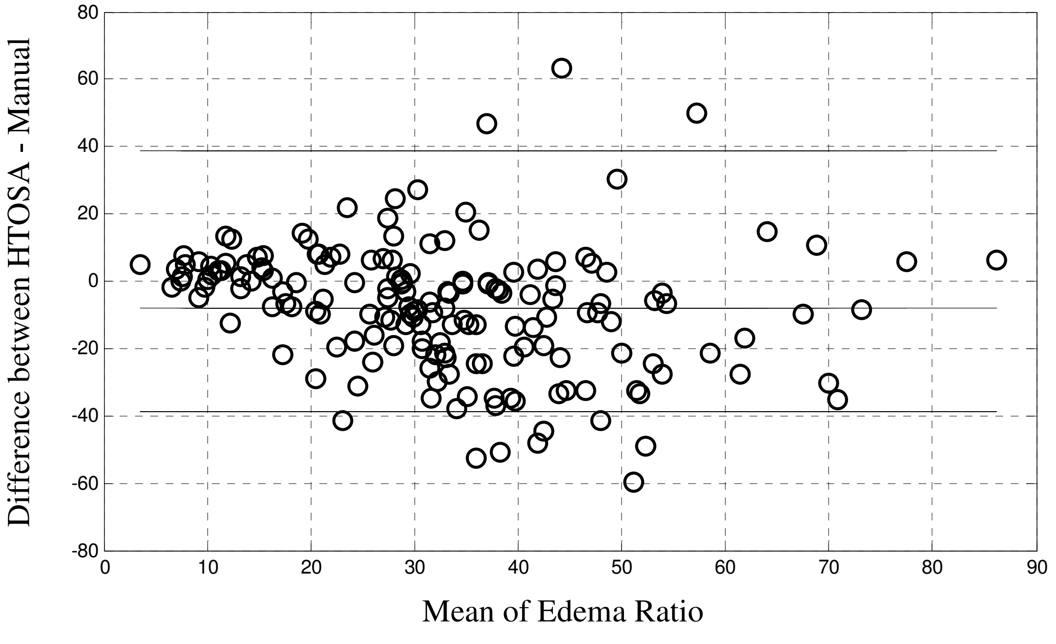

Figure 6.13: Bland-Altman Analysis of Manual- HTOSA

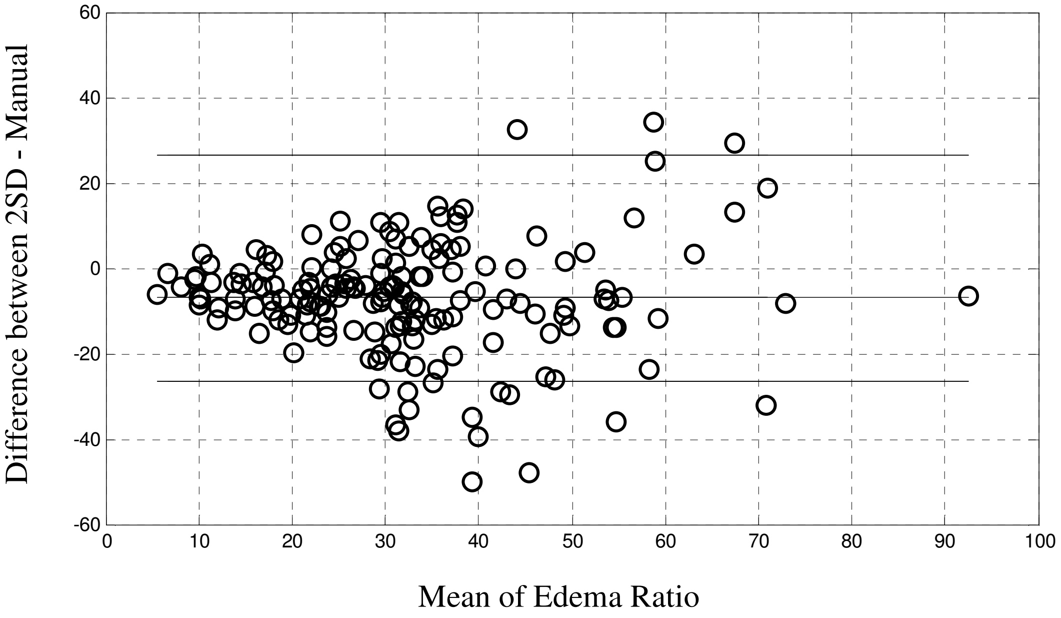

Figure 6.14: Bland-Altman Analysis of Manual-2SD

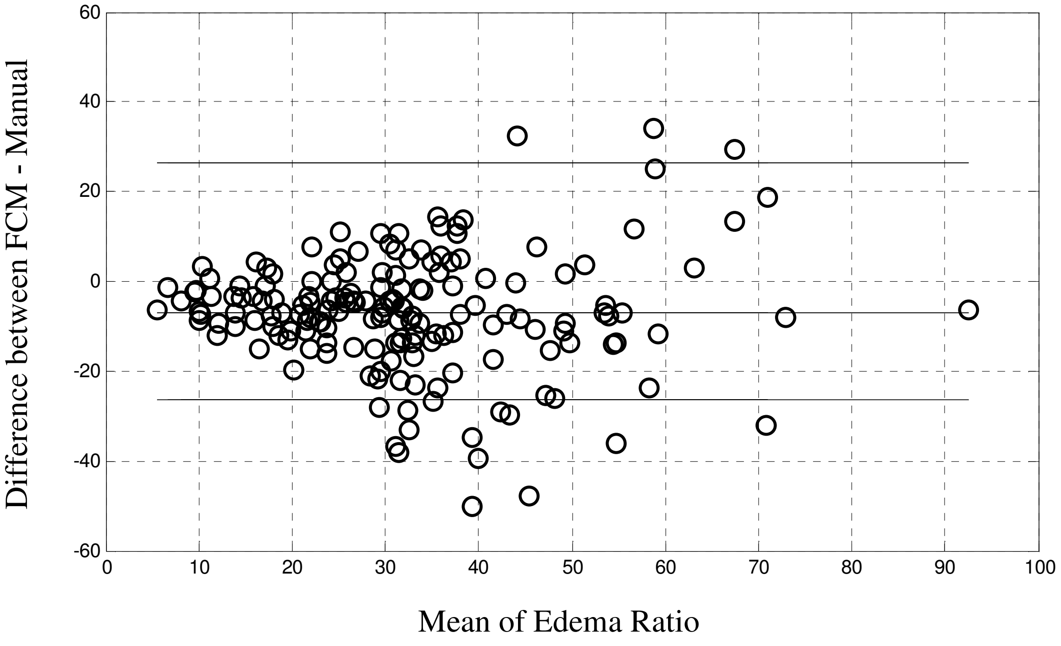

Figure 6.15: Bland-Altman Analysis of Manual- FCM

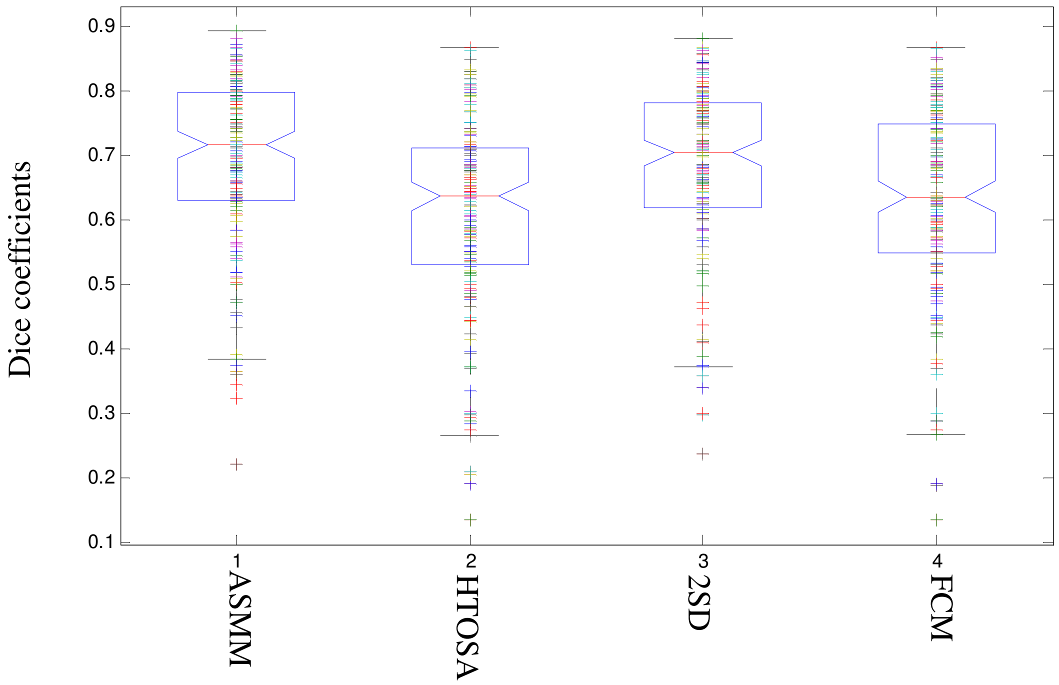

Figure 6.16: Box plot for DSC for, ASMM, HTOSA, 2SD, and FCM

In general it was found that the four methods have demonstrated the ability to quantify the edema in the entire test images with varying degrees of accuracy when compared to the gold standard. From the experiments it can be seen that the ASMM has the best correlation (0.752) relative to the manual segmentation when compared to the other three methods. The results from HTOSA did not significantly differ when compare to ASMM (0.705). This results are due to the characteristic of dark CMR signal in T_2-weighted image which is not Gaussian distributed (Gudbjartsson and Patz, 1995b) such as used in 2SD and HTOSA when compared to ASMM where Rician distribution is used and thus provides a better representation of the dark CMR signal.

In term of DSC, according to Zijdenbos's (Zijdenbos et al., 1994) , a DSC greater than 0.7 indicates a good agreement between the two measurements. The Dice similarlity coefficient, derived from a reliablity measurement known as the kappa statistic, provides a value that can be used for similarity comparison, and reflects both size and localization agreement between the two different measurements, such as pixel-by-pixel basis in this study. From the result it can be said that ASMM

(DSC= 0.73) and HTOSA method (HTOSA= 0.68) have good agreement with the manual segmentation. The results presented in Figure 6.16 where the DSC is plotted on a box plot for ASMM and since 50% of the data are within the box and the value of the lower hinge of the box is 0.63 it can be said that nearly 50% of the edema segmentation using ASMM fall above the minimum accepted DSC value which is 0.7. Bland-Altman analysis shows the four algorithms analysed in this experiment demonstrate low mean bias when compared with manual thresholding which mean the four algorithms tend to overestimate the percentage of edema within the LV wall.

The experimental results indicate that ASMM, based on characteristic features of the histograms of LV myocardium from T_2-weighted CMR images, has better accuracy for clinical edema quantification with highest linear correlation coefficient, least agreement limit, and greatest DSC among the 4 automatic approaches. Since ASMM is simple to use and generic it can be used with images obtained from scanners from different vendors. Therefore the method has potential to be used clinically in automatic area-at-risk assessment in acute MI patients.

6.4.3 Reproducibility

This section presents quantitative experimental results and discussion on the performance of ASMM using a first and a second datasets. The idea of this experiment is to look into the reproducibility of the algorithm when a new data set is used. The reproducibility of the algorithm is consistent for the two datasets which have only a small variation in-term of the correlation results. The correlation result from the first data set (r=0.77±0.03) is comparable to the correlation result of the second dataset (r=0.72± 0.03). Then a Dice similarity coefficient was performed on the two datasets and the result further suggest that the ASMM has potential to be adapted to new data set as illustrated in Table 6.2.

Table 6-2: Comparison of dice similarity coefficient of two datasets

	Dice similarity	
	Dataset 1	Dataset 2
mean	0.70±0.03	0.69±0.07

The experiment shows the consistency of the ASMM when presented with new dataset, which infers that ASMM can potentially be implemented to new datasets with no modification in term of its parameter.

6.4.4 Speed

The objective of developing the automatic system is to reduce the processing time of segmenting and quantifying the edema for each patient. We compare the time taken for the automatic method to process for one patient with the manual method performed by clinician. The average processing time for one patient was 40±6 seconds on a DELL laptop (2.40GHz Inter Core i5 CPU, 4GB memory), which is much faster than manual edema delineation, (range from 360 to 420 seconds) for an experienced cardiologist.

6.4.5 Threshold value for ASMM

A parameter study of the thresholding operation for automatic edema delineation was performed by varying the threshold value for I_{map} from 0.6 to 0.9 (equation 6.5), the results are summarized in Table 6-3. Generally the thresholding values of 0.7 and 0.8 give better results than for 0.6 and 0.9. When the threshold value increases, the edema decreases and vice versa.

Table 6-3: Parameter study on the thresholding operation (15 patients)

Thresholding value	Edema extent	Difference related to manual	Dice similarity coefficient (manual)
0.6	31±9%	6±5%	0.73±0.06
0.7	28±8%	4±3%	0.74±0.06
0.8	25±7%	4±4%	0.73±0.07
0.9	21±6%	6±5%	0.7±0.08

6.5 Conclusion

In this chapter two novel edema quantification algorithms have been presented. The first algorithm is the ASMM which used the Rician distribution which better represents a dark CMR signals. Second algorithm is the HTOSA which used Gaussian distribution to represent the CMR signal.

From the experiments it was found that the ASMM performed better when compare to the HTOSA, thus the ASMM is the method of choice for edema quantification in this work and therefore it has potential to be used clinically in automatic area-at-risk assessment in acute MI patients.

CHAPTER 7

7. GLASGOW HEART: AN INTEGRATED PLATFORM FOR CARDIAC RESEARCH

7.1 Introduction

Figure 7.1 shows an overview of the Glasgow Heart an integrative platform for LV research that contains the work presented in this thesis as a subset. The MRI facility and pathology provide the MRI machine and patients for the study. Next the signal processing unit provides automatic tools for the segmentation and quantification of the LV wall as presented in chapter 5, the segmentation and quantification of edema as presented in chapter 6 and 3D quantification and visualization of the edema on LV wall. The work of the mathematical group is to bring the imaging process to computational modelling such as biomechanical study, structural study and functional study.

This chapter presents new 3D LV wall reconstruction that project edema region segmented on 2D onto a 3D surface, allowing for a much better visualization of the shape and location of the edema. The remainder of the chapter is structured as follow. Section 7.2 shows system overview of the proposed algorithm. In section 7.3 we present details of 3D visualization and quantification of edema without apex information. Section 7.4 3D visualization and quantification of edema with apex information is presented. Section 7.5 provides the result of the visualization and comparison with 3D result from manual segmentation. Finally, conclusions are presented in section 7.6.

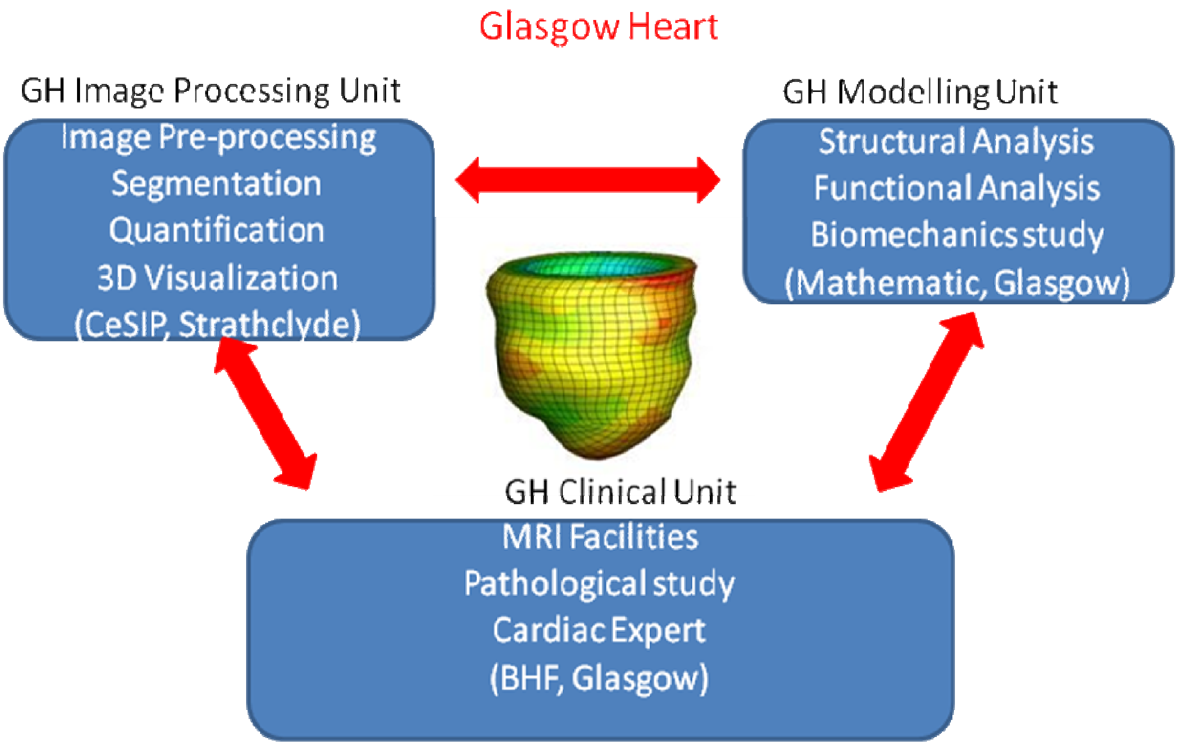

Figure 7.1: Glasgow Heart Integrative Platform for LV Research

7.2 System Overview

Figure 7.2 shows an overview of the proposed 3D visualization and quantification algorithm. First when a stack of patient CMR image is obtained, the image pre-processing is performed and the LV boundary is segmented. Then the boundary of the edema is segmented. The information of the two segments is then used as an input to visualize and to quantify by the algorithm.

The segmentation of LV wall and edema boundary are done on JPEG image, therefore to get the information on the slice location and slice thickness the segmentation result is projected back onto the original DICOM T_2-weighted CMR image. Once the information is projected to the DICOM image the location of the slice and thickness between slice is used to interpolate and to generate 3D image.

Here we proposed two approaches in visualizing the 3D image. The first approach is to automatically generate 3D image after the interpolation. In the first approach the information on the most apical slice is not included, since it is very difficult to automatically segment this slice. In the second approach we include the information on the most apical slice. This is done by manually segmenting the Long axis (LA) image. Then the information from the SA image is projected to the LA image and vice versa. These stages in the algorithm are discussed in detail in the following sections.

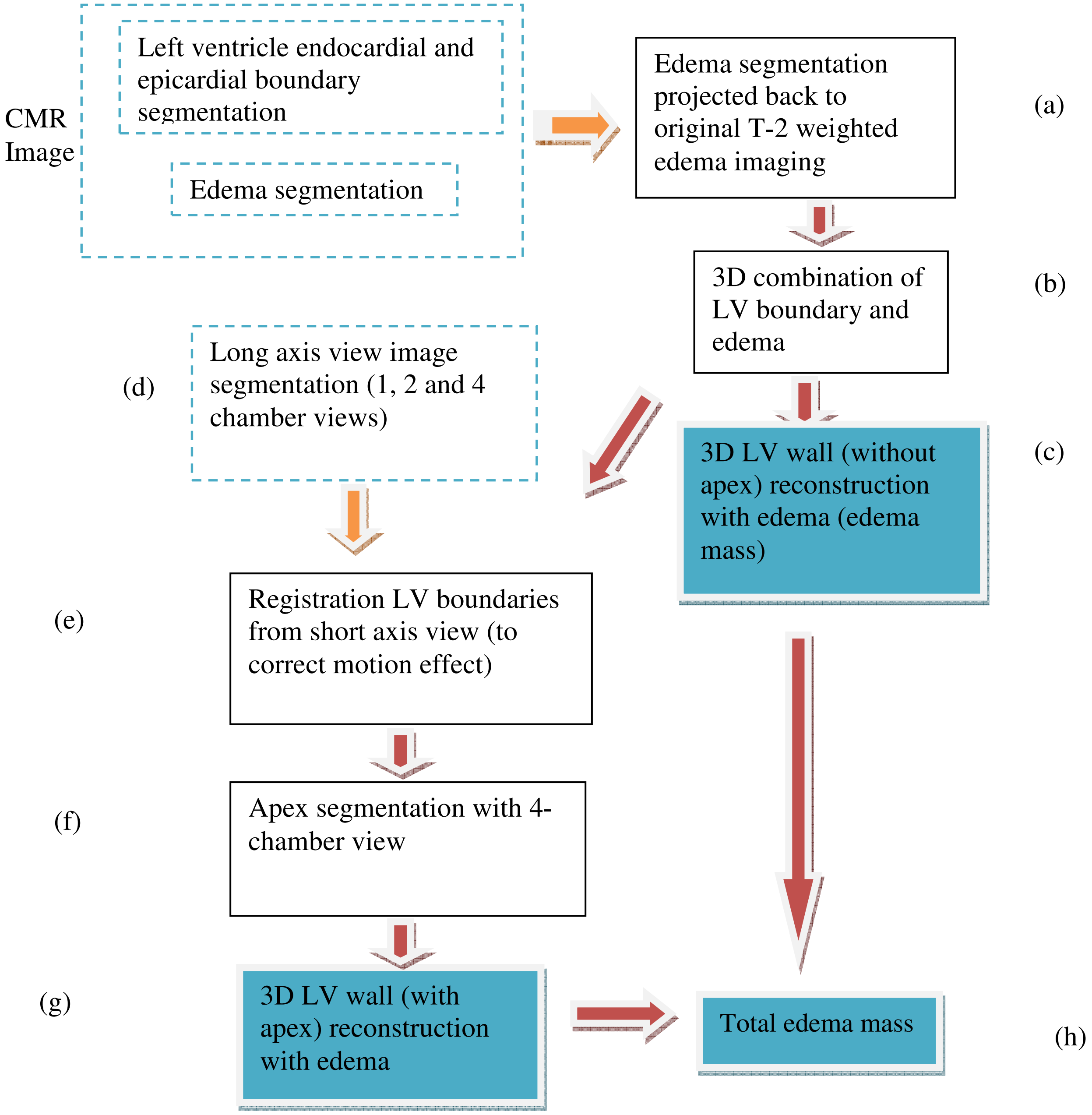

Figure 7.2: 3D Visualization and Quantification Overview

7.2.1 LV wall segmentation

The first step for 3D edema quantification and visualization is to separate the LV wall from the rest of the CMR image. The method takes multi-slice T_2-weighted CMR images (an MRI data stack) from the basal to the apex of the heart. It comprises 3 main stages, firstly the image is pre-processed to remove heterogeneity within the blood pool region and also to smooth the LV wall region while preserving the strong boundary using anisotropic diffusion (Perona and Malik, 1990) . Then a fuzzy method between inter-slice and intra-slice is used for guiding the centre point detection in each slice for automatic initialization (Kushsairy Kadir et al., 2010a). Finally the LV wall is segmented using the method presented in chapter 5 of the thesis.

7.2.2 Edema segmentation

Once the LV wall has been segmented, we used an automatic statistical mixture model (ASMM) to segment the edema region from the rest of the LV wall. In this technique we fit Rayleigh distribution and Gaussian distribution to the normal tissue signal intensity which tend to be low and edema signal intensity which tends to be high. Then the mean of the two models can be obtained and the threshold value is determined using fuzzy based rules. Then we performed a post processing stage to remove any false edema region and also to include microvascular obstruction (MVO) as part of the edema region. More details of this approach are presented in chapter 6 of the thesis.

7.2.3 LV geometry reconstruction

Figure 7.3 shows the process of generating 3D model from 2D images. In Figure 7.3(a) the slice location and thickness between slice are determined from the DICOM image header. In our implementation the information between the slice is interpolated by using Trilinear interpolation (Farin, 1997). Trilinear interpolation is a process of linearly interpolating points within a 3-D box given values at the vertices of the box, and it is most commonly used for interpolation within cells of a volumetric dataset. Figure 7.3(b) shows a 3D image after the interpolation. In Figure 7.3(c) shows that the 3D image is made of small cubic image.

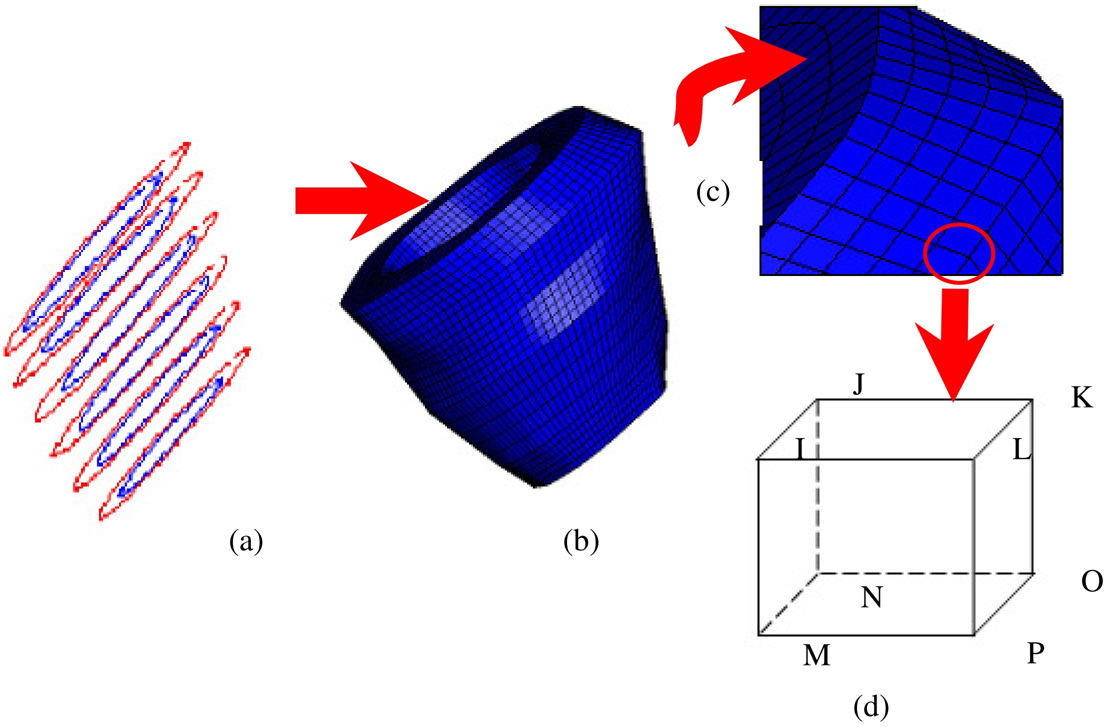

(a) (b) (d)

Figure 7.3: 3D Visualization (a) slice position, (b) interpolated 3D image, (c) zooming of 3D image and (d) each small cubic cell

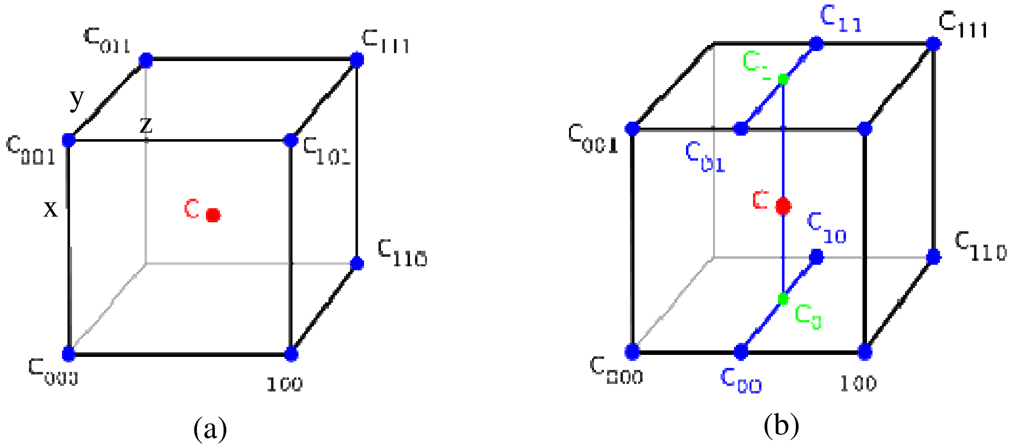

(a) (b)

Figure 7.4: (a) Eight corners point, (b) 3D Trilinear interpolation (Bourke, 1999)

Trilinear interpolation process can be summarized as a process of performing three consecutive linear interpolations along three coordinate axes: x, y, and z, respectively. Figure 7.4(a) shows small cubic cell and with the lower left base vertex as the origin. The coordinate values at each vertex are denoted as *C*000, *C*100, *C*010,

. . .. *C*111. Let *xd*, *yd*, and *zd* be the differences between the target of *x, y,* and *z* related to the cubic lattice [*x*], [*y*], and [*z*]. The actual error values at eight corners of the cubic lattice given by *V*000, *V*100, *V*010, . . ., *V*111, which are in three axes:

$$\begin{aligned} xd &= x - [x] \\ yd &= y - [y] \\ zd &= z - [z] \end{aligned} \qquad 7\text{-}1$$

First we perform the linear-error interpolation along the *z*-axis (by pushing the front face of the cube to the back), which is

$$\begin{aligned} V00 &= V000\,(1 - zd) + V100\,zd \\ V10 &= V010\,(1 - zd) + V110\,zd \\ V01 &= V001\,(1 - zd) + V101\,zd \\ V11 &= V011\,(1 - zd) + V111\,zd \end{aligned} \qquad 7\text{-}2$$

Next, we interpolate these error values along the *y*-axis while pushing the top edge to the bottom giving:

$$\begin{aligned} V0 &= V00\,(1 - yd) + V10\,yd \\ V1 &= V01\,(1 - yd) + V11\,yd \end{aligned} \qquad 7\text{-}3$$

Finally, we interpolate these error values along the *x*-axis (walking through a line), which provides us with a predicted error value for the target point:

$$tp = V0\,(1 - xd) + V1xd \qquad 7\text{-}4$$

Figure 7.4(b) illustrates the above operations. First, we perform linear interpolation between C000 and C100 to find V00, C001 and C101 to find V01, C011 and C111 to find V11, and C010 and C110 to find V10. Then, we perform interpolation between C00 and C10 to find V0, C01 and C11 to find V1. Finally, we calculate the error value C via linear interpolation of C0 and C1. In actual fact trilinear interpolation is a three successive linear interpolation or two bilinear interpolations combined with a linear interpolation.

7.3 3D Visualization of Edema without Apex Information

The first approach of a 3D visualization proposed in the thesis is a fully automatic technique. Figure 7.5 illustrates the block diagram of the system. First the information on LV boundary and edema boundary is used as the input. Next the information from the JPEG is projected onto the DICOM image. Then the information on LV boundary and edema boundary is merged together. Finally a 3D model is reconstructed for visualization and quantification.

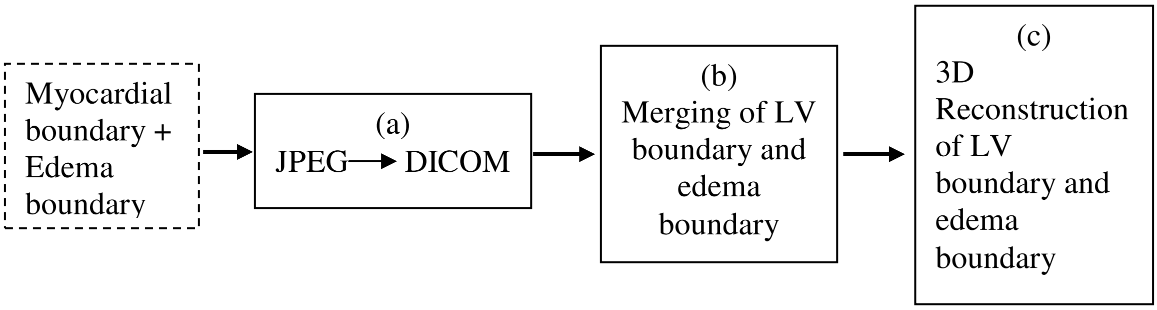

Figure 7.5: Fully automatic 3D visualization system without apex information

7.3.1 Edema segmentation projected back to original T_2-weighted edema imaging

Edema delineation is based on exported JPG images, therefore the segmented edema needs to be projected back to original T_2-weighted MRI images. Figure 7.6(a, b) illustrates a DICOM image and corresponding JPG image exported from Siemens software after gray-scale intensity adjustment for edema showing. Due to the difference size of the JPEG image and the DICOM image, therefore a resize procedure is needed in order to project the segmentation result from JPEG images back to original DICOM images.

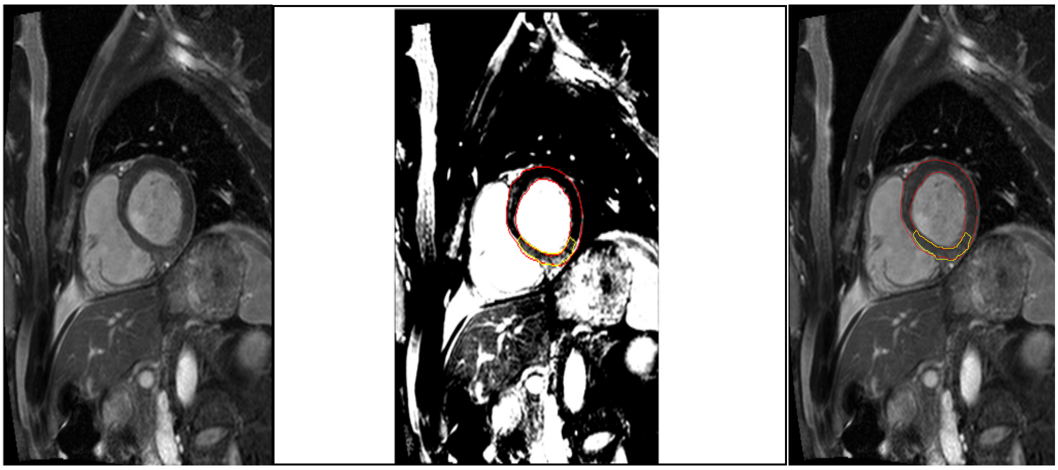

(a) (b) (c)

Figure 7.6: (a) A DICOM image of LV wall with T_2 Weighted MRI, (b) the corresponding JPG image, (c) DICOM image with LV boundary and edema boundary

7.3.2 3D combination of LV boundary and edema segmentation

Figure 7.7(a) shows the LV short axis slices in 3D context with LV wall boundaries from Manual segmentation. Figure 7.7(b) shows the LV wall boundary with contoured edema region from basal location to Apex.

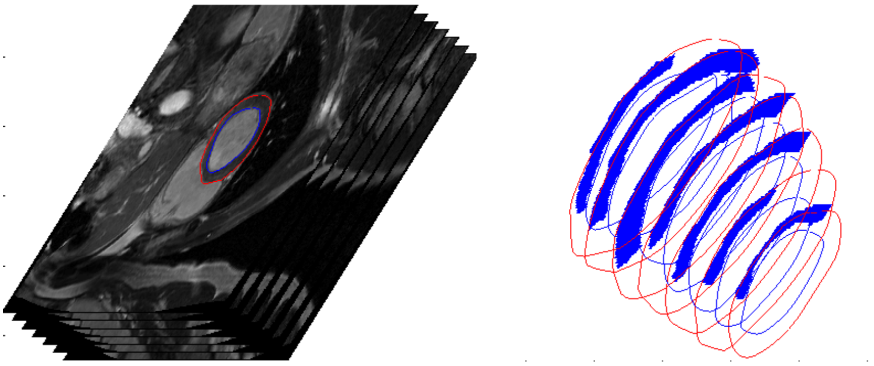

(a) (b)

Figure 7.7: (a) 3D display of MRI images, (b) segmentation results of LV wall and edema

7.3.3 3D LV wall (without apex) reconstruction with edema (edema mass)

Figure 7.8(a) shows the endocardial and epicardial boundaries with 3 more curves inserted between endocardial and epicardial boundaries, the red dots stand for the locations associated with edema presence. A location was considered to be associated with edema if a 3 by 3 region with the location in the centre totally lies in edema region. Figure 7.8(b) shows the reconstructed LV geometry only from short axis images, and there is no Apex. In total there are four layers of mesh elements across LV wall from endocardium to epicardium.

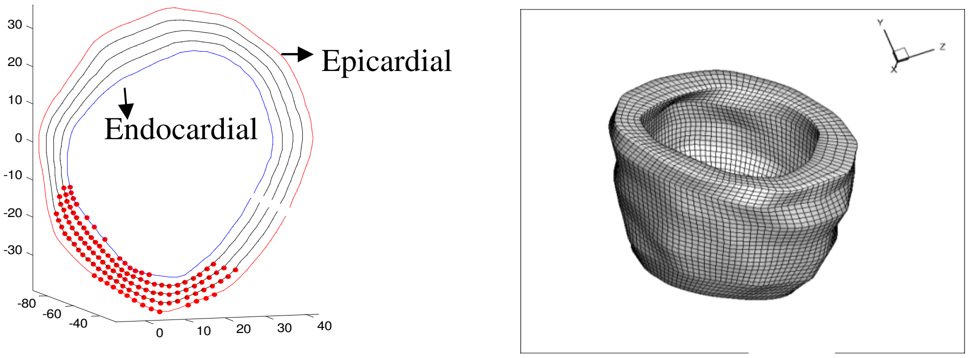

(a) (b)

Figure 7.8: (a) LV boundaries with inserted curves between endocardial and epicardial boundaries, (b) reconstructed LV geometry

Figure 7.9(a, b) shows the edema distribution with 2 different views. The colour scheme stands for the ratio of edema at regions surrounding each node location (value 1 stands for 100% edema, 0 stands for healthy region). Figure 7.9(c) shows edema distribution on a slice section expanding from base to apex. From Figure 7.9, the transmural distribution of edema is also available for screening. In this case the myocardium density is 1.05g/mL, the total mass of the LV without apex is 110g and the edema mass is 28g which represents 25.5% of the total LV wall volume.

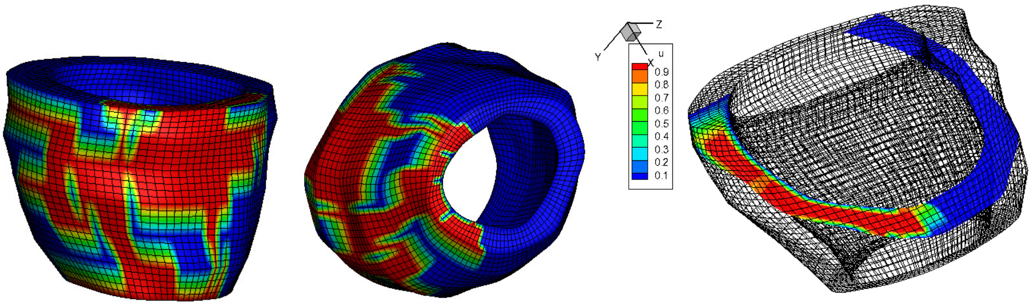

(a) (b) (c)

Figure 7.9: (a) and (b) Edema Distribution in Reconstructed 3D LV Geometry with Different Views, (c) Cross-section View

7.4 3D Visualization of Edema with Apex Information

The second approach in the proposed system is to include the information of the apex into the 3D image. The most apex slice is difficult to be segmented automatically. Hence to include the slice, we manually segment the LA view of the LV and the SA slice can then be projected to LA view. Figure 7.10 illustrates the block diagram of the proposed 3D visualization and quantification with apex information.

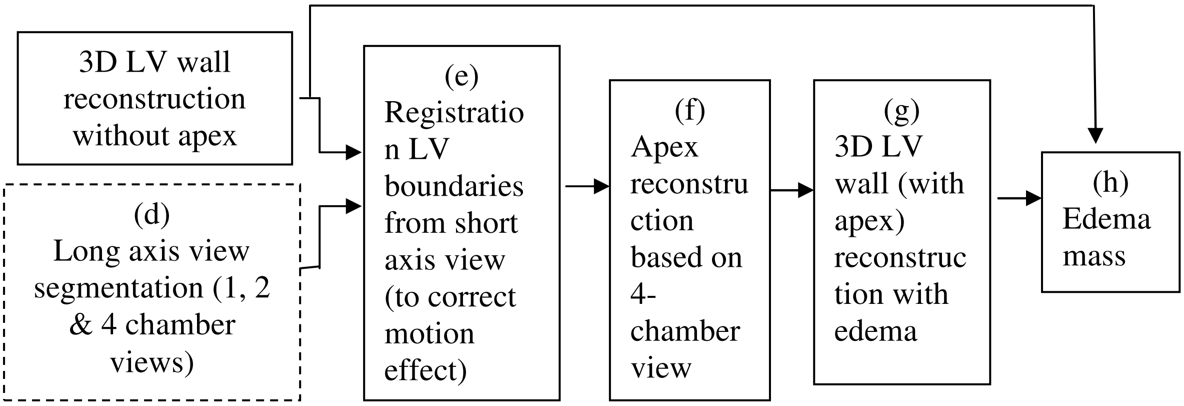

Figure 7.10: 3D Visualization System with Apex Information

7.4.1 Long Axis view image segmentation (1, 2 and 4 chamber views)

In order to reconstruct the apex region, long axis images are needed. Here manual segmentation of the apex in the long axis slice of 4-chamber view was performed. Figure 7.11 shows 3 different views of the long axis images, since the LV wall boundary has been segmented in short axis slices, therefore each short axis slice location can be decided from the MRI scan parameters, and the boundaries in each short axis also can be projected in the long axis views as in Figure 7.11, in which the red and blue points are from boundaries in short axis slices. However due to the motion affects, the segmented boundaries in short axis slices do not always lie in the correct LV boundaries in the long axis views, especially in the 2-chamber view (Figure 7.11). Therefore a rigid motion correction was applied for short axis images as follows:

(a) manually adjust those boundary points in the long axis views to the right locations;

(b) project the adjusted boundary points back to each short axis slices, there will be 6 points along endocardium and 6 points along epicardium decided from the long axis views for each axis slice;

(c) a closed spline passing through all the 6 points on the endocardium was constructed, and the centre point of the constructed region bounded by the closed spline was calculated, C_{LAEndo};

(d) move the LV boundary (BC_{SA}) segmented based on the short axis slice by the equation: $BC_{SA}=BC_{SA}+ (C_{SAEndo} - C_{LAEndo})$, C_{SAEndo} stands for the centre point of the region bounded by endocardial boundary segmented from short axis slices.

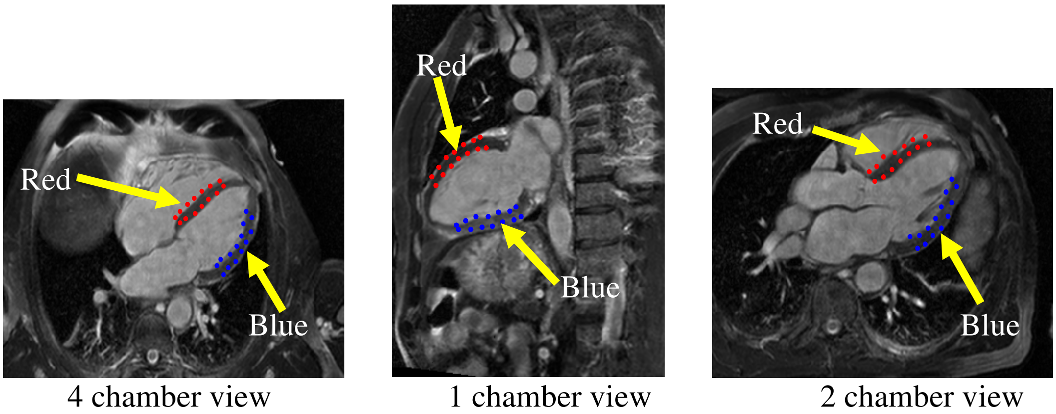

4 chamber view 1 chamber view 2 chamber view

Figure 7.11: LA Views with Segmented Boundaries from SA Slices

7.4.2 Registration LV boundaries from short axis view

Figure 7.12 shows the alignment of LV boundaries (blue dash lines) from short axis views to the centre of the long axis view boundaries (yellow curves) for motion correction, the final aligned LV boundaries are presented with red colour.

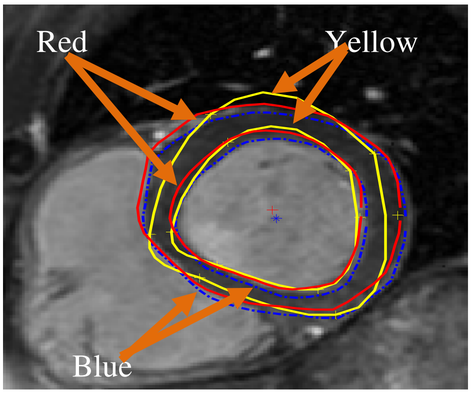

Figure 7.12: Alignment of SA Boundaries with LA Boundaries

7.4.3 Apex segmentation with 4-chamber view

Manual segmentation of Apex is shown in Figure 7.13(a) with existed boundary points from short axis slices. Figure 7.13(b) shows the reconstructed boundary curves with apex from the 4 chamber view.

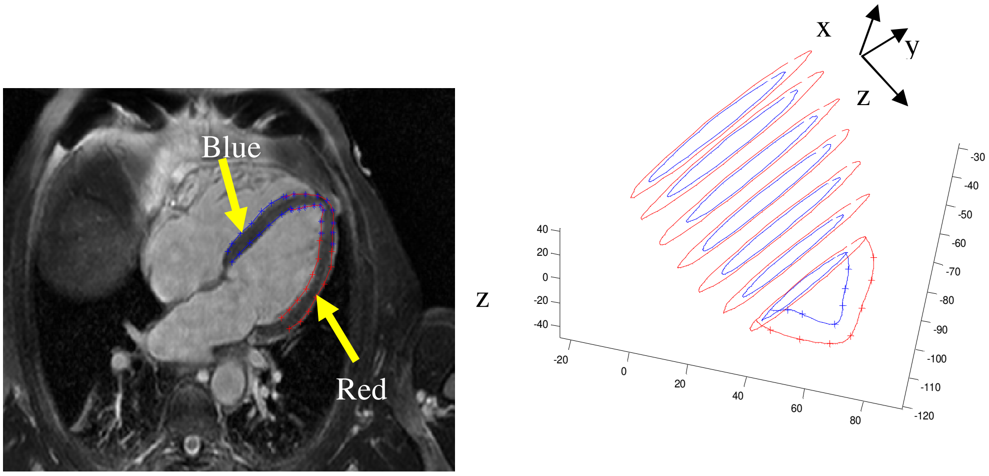

(a) (b)

Figure 7.13: (a) Apex segmentation, (b) Reconstructed Boundary Curves with Apex from the 4Chamber View

7.4.4 3D LV wall (with apex) reconstruction with edema

Currently the apex is only reconstructed from 4-chamber view long axis slices, while there are two different views from one chamber view and two chamber view, which need to be implemented in the future for integrating the 3 long axis views for apex reconstruction. The edema distribution in apex has not been reconstructed due to the limited data from long axis views. Figure 7.14 is the reconstruction result. The total mass of LV wall is 127g, and total edema mass without apex is 28g, and the apex mass is 17g.

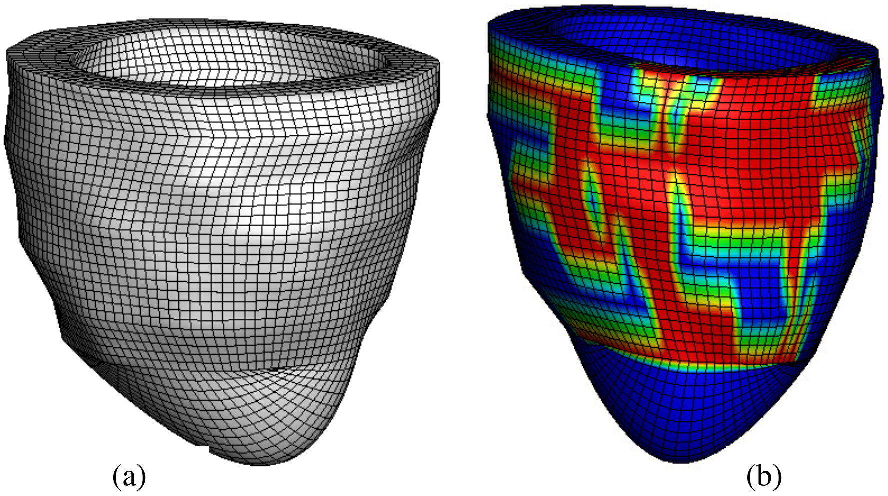
(a) (b)

Figure 7.14: (a) LV Geometry with Apex; (b) Edema Distribution in LV Wall except for Apex Region

7.5 Experimental Results

This section presents the experimental results of the 3D visualization and quantification system. The 3D results from the automatic segmentation method are compared with the 3D results from the manual segmentation method. Both 3D images with and without apex are shown for visual inspection. Quantitative results in term of edematous volume are presented here to show that the automatic method gave comparable outcome to the manual method in an improved time duration.

7.5.1 Qualitative results of Automatic method versus Manual method

Qualitative results are presented here. The 3D images from 3 patients are selected for comparison (patient1, patient2, patient3) with the manual method. Figure 7.15 to Figure 7.20 show the results from 3 patients.

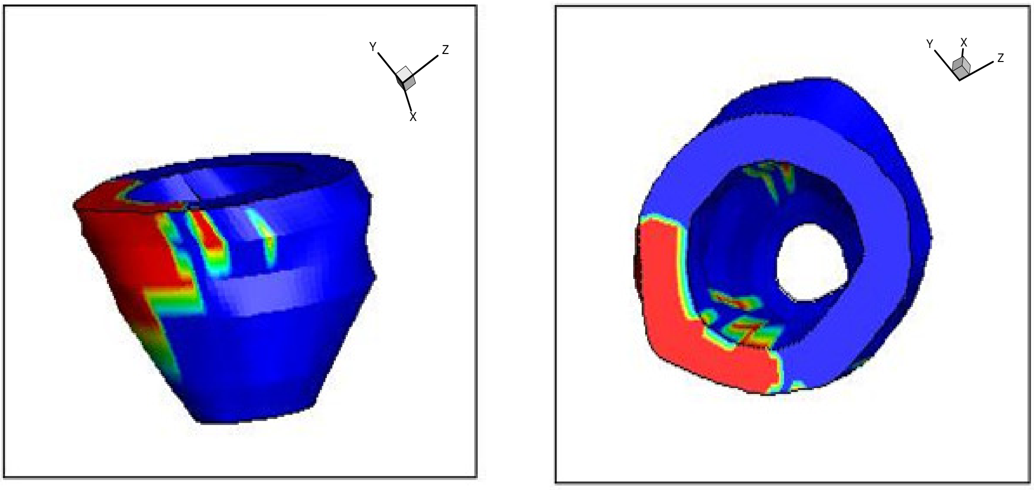

(a) (b)

Figure 7.15: Edema Distribution (patient 1) using Automatic Method; (a) side view (b) top view

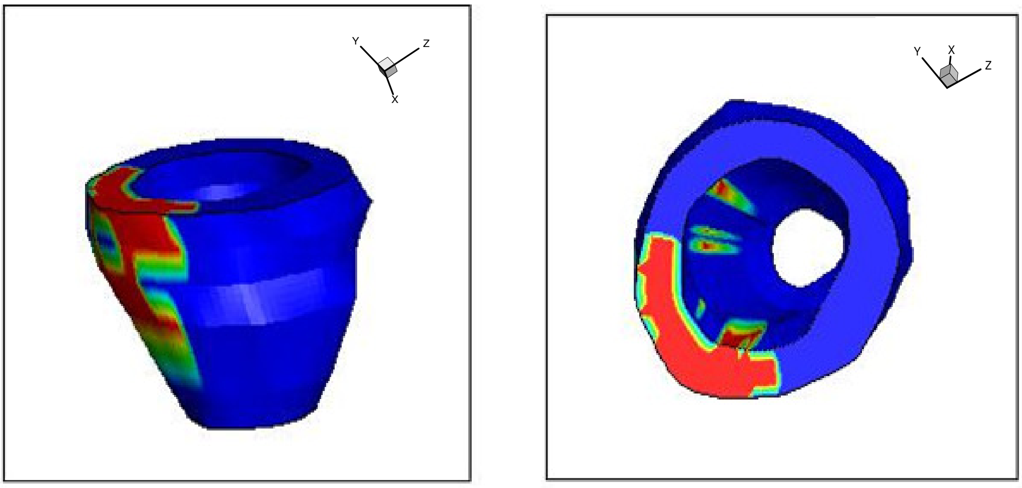

(a) (b)

Figure 7.16: Edema Distribution (patient 1) using Manual Method; (a) side view (b) top view

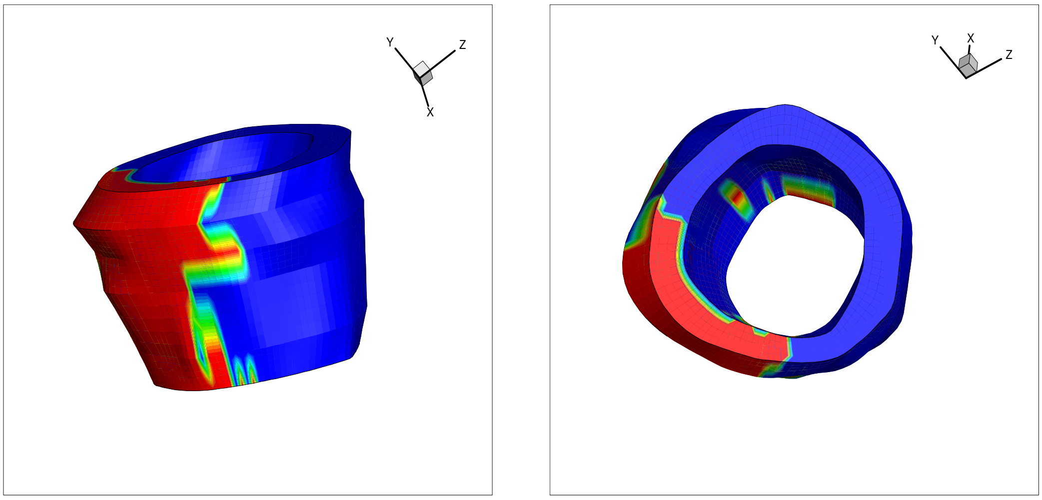

(a) (b)

Figure 7.17: Edema Distribution (patient 2) using Automatic Method; (a) side view (b) top view

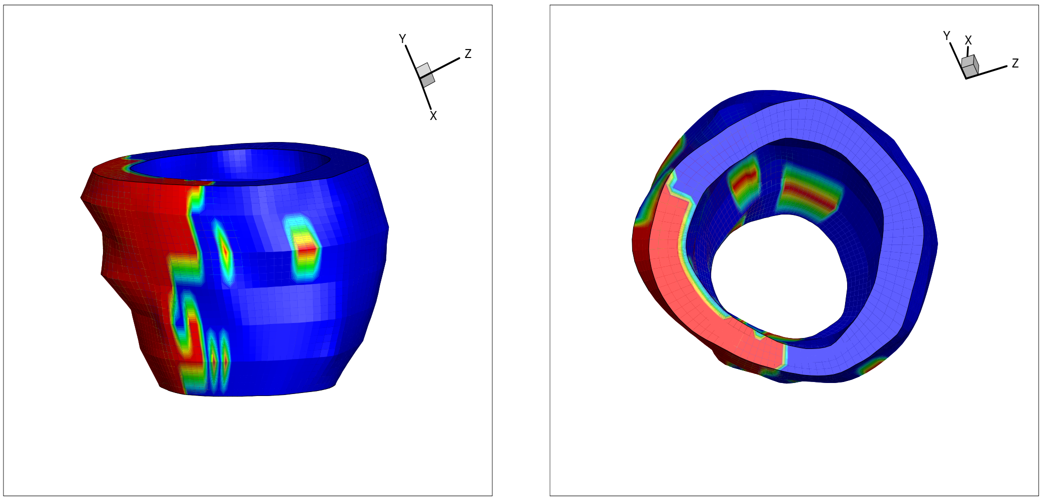

(a) (b)

Figure 7.18: Edema Distribution (patient 2) using Manual Method; (a) side view (b) top view

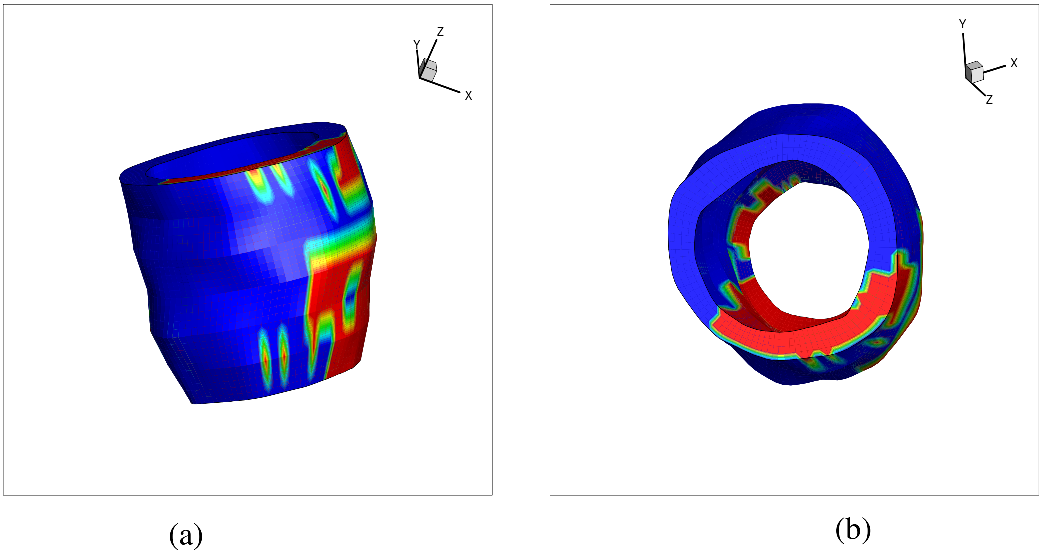

(a) (b)

Figure 7.19: Edema Distribution (patient 3) using Automatic Method; (a) side view (b) top view

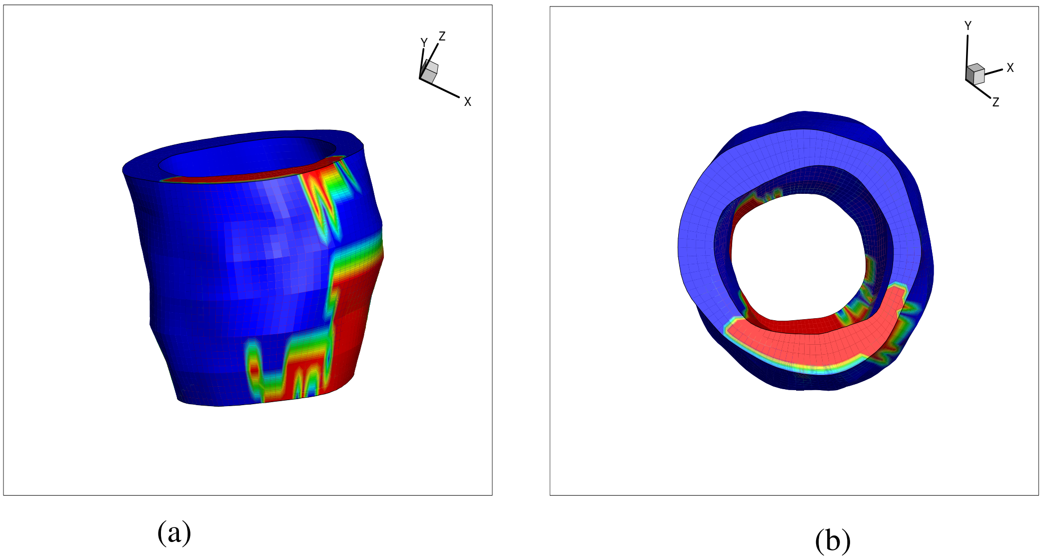

(a) (b)

Figure 7.20: Edema Distribution (patient 3) using Manual Method; (a) side view (b) top view

Qualitatively, the 3D images generated from the automatic scheme closely matched with the 3D images generated from the manual scheme with the volumetric extent of the edema from both methods highly correlated with dice similarity coefficients of 0.72±0.06 for patient one, 0.76 ±0.05 for patient two and 0.74±0.06 for patient three, suggesting good accuracy between the two methods.

7.5.2 3D visualization with Apex

The 3D views from two patients are shown in this section. The inclusion of apex provides a better representation of the LV which further enhances clinician understanding on the extension of edema within the LV wall.

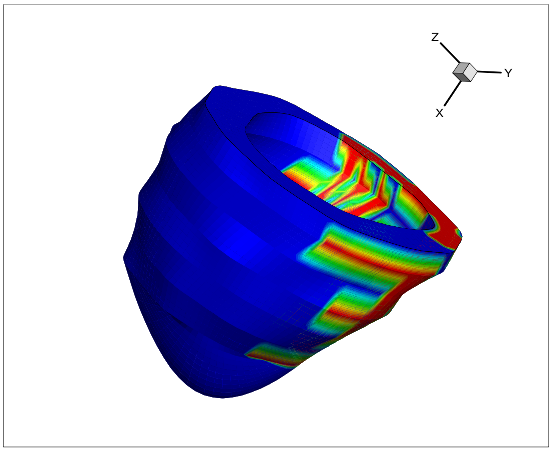

(a)

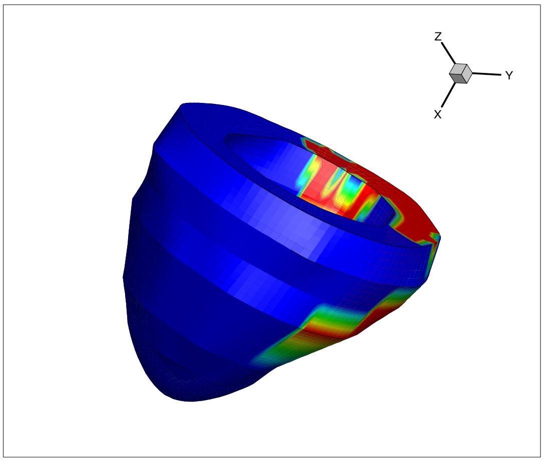

(b)

Figure 7.21: Edema Distribution from 2 patients on 3D LV Wall

In our method the inclusion of the apex is only for visual enhancement, since the apex is manually segmented from LA view of the CMR image.

7.5.3 Performance analysis of automatic segmentation method versus manual segmentation method

Statistical analysis is presented in this section. The main objective of this experiment is to provide objective measure of significant advantage of the proposed method in helping the clinician investigate the edema volume from the patient.

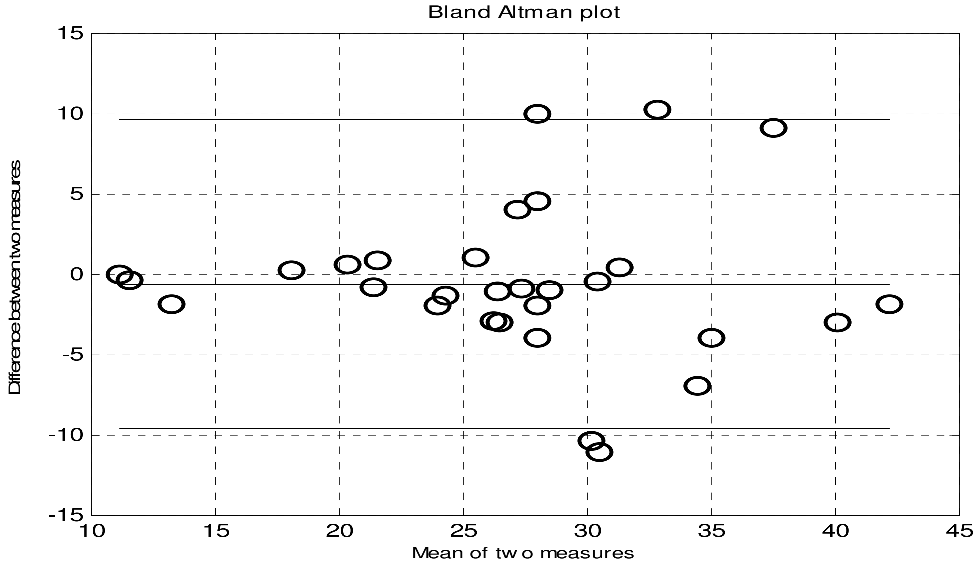

Figure 7.22: Bland-Altman plot of Edema Mass Extent between Manual results and the Automatic approach

Figure 7.22 illustrates the Bland-Altman analysis of the volumetric extent of edema (% of left ventricle) between the manual and our automatic results. The mean bias for edema extent related to the whole left ventricular mass is -1.9% suggesting the automatic method tends to overestimate the edema volume slightly.

In Table 7-1 the comparison results of volumetric extent of edema for each patient among the automatic method and manual method are summarised. The table further suggest that the automatic method tends to overestimate the manual method; this is shown by the mean mass volume from the manual method which is 27±9% as compared to automatic method which is 29±8%. The result of the dice similarity index between the two methods is 0.75±0.08, which suggest good overlap between the automatic method and the manual method.

Table 7-1: Edema Volume Comparison for 30 patients

	Manual	Automatic	Dice similarity coefficient based on volume overlap (mean ± SD)
% edema mass Volume (mean ± SD)	27±9%	29±8%	0.75±0.08

7.6 Conclusion

This chapter presented an integrative approach for 3D visualization and quantification of edema. The key contributions are 1) automatically segment the LV wall and quantify the extent of edema within the LV wall, 2) generating 3D LV wall showing the extend and location of edema for enhancing clinician diagnosis. The present results are encouraging with good overlapping between automatic method and the manual methods. From the result it shows that the proposed 3D visualization has potential for clinical application.

CHAPTER 8

8. CONCLUSION AND FUTURE WORK

8.1 Conclusion

This thesis investigated the various stages involved in the LV image analysis from T_2-weighted images. The main focus of this research was to develop automatic edema segmentation and quantification with a 3D visualization system. A new integrated approach for edema segmentation, quantification and visualization was developed, including the left ventricle boundary detection, edema segmentation and quantification and 3D visualization were presented in this thesis.

Automatic segmentation of LV wall is a challenging problem but is an essential part in any analysis technique either for physiological study or pathological study. Our proposed method to solve this problem is by using LSM to segment the endocardium and epicardium of the LV. We approach the problem systematically by first using a fuzzy based decision technique to automatically locate the centre of the blood pool of the LV. This point is used to initialize LSM to segment the endocardium. To overcome the effect of the papillary muscle we applied a convex hull algorithm to remove concavity of the blood pool especially around the mid-ventricle slice. Once the endocardium has been segmented, the epicardium needs to be segmented. The segmentation of epicardium presented a different set of problems such as weak edges and the presence of edema tissues which have high signal intensity compared to normal myocardial tissue, which might traps the LSM on the edge of the edema instead of the edge of the epicardium. To overcome the effect of edema we calculate average intensity value of the LV blood pool. Then any value below the value of the blood pool region can be converted into a normal wall region with a designated value. Although this helps to decrease the effect of the edema, it will magnify the effect of weak edges in the image. In our approach to segmentation of the epicardium, we introduced an additional shape constrain to the LSM. This constrain is created by using the information around the septum region to estimate typical myocardial thickness. Then a new LSM method using the additional shape constrain called LSMwASC is used to segment the epicardium.

Two novel edema segmentation algorithms, hybrid thresholding edema sizing algorithm (HTOSA) and automatic statistical mixture model (ASMM) have been developed to segment and quantify edema from the LV wall. In HTOSA we automatically set the threshold value based on the image intensity histogram. The advantages of this method is that it is totally automatic, thus we remove user input and in its capability to include microvascular obstruction as part of the edema. In ASMM we utilize the characteristic of the MRI signal that is modelled by Rician distribution. Then we use Rayleigh distribution to model the normal tissues and Gaussian distribution to model the edema tissues. Then the edema region is determined by merging the two distributions together.

Finally, the work of this thesis represents part of Glasgow Heart (GH) which is an integrated platform for Cardiac Research. The GHSPU (GH Signal Processing Unit) in the platform has incorporated the novel segmentation of edema from each slice and the consequent transformation into 3D images. The advantages of this platform lies in its ability to quantify edema in terms of volume edema mass compared to the total LV volume and also in its ability to increase clinician capability to diagnose edema by looking not only on the quantitative value, but also the spatial position and extent of edema within the LV wall.

8.2 Future Works

Although the proposed automatic edema segmentation and quantification with 3D visualization system was shown to perform well several improvements that could enhance the system, which are now described: The following areas are of interest for potential further investigation.

1) Removing the post-processing stage of the endocardium segmentation: in the implementation in this thesis. We performed the post processing to remove

the effect of papillary muscles from the blood pool region. A constraint based on an elliptical model can be adapted to remove the papillary muscles since the shape of the blood pool is similar to an elliptical shape.

2) Apply the algorithm to LE image for segmentation and quantification region of infarct: to get comprehensive study on viability of heart after MI, the infarct region which represents dead myocardial tissues need to be segmented and quantified. Once the edema region and infarcted region has been segmented and quantified we can develop a viability assessment model for a heart attack patient.

3) Evaluation on larger data set: The proposed method was tested on a CMR data set with 30 subjects. In order to get a better evaluation it is desirable to test the proposed method with a larger data set.

Author Publication

Conference

1. K Kadir, A Payne, J.J. Soraghan, C Berry, Automatic Quantification of Oedema from T_2 Weighted CMR image using Hybrid Thresholding Oedema Sizing Algorithm (HTOSA), Computing in Cardiology, 2010
2. Kushsairy Kadir, Hao Gao, Alex Payne, John Soraghan and Collin Berry," Variational Level Set Method with Shape Constraint and Application to Edema Cardiac Magnetic Resonance Image," *DSP 2011*, Corfu, Greece, July 2011.
3. Kushsairy Kadir*, Hao Gao, Alex Payne, John Soraghan, *Senior Member, IEEE*, and Colin Berry," Automatic Quantification and 3D Visualization of Edema in Cardiac MRI", EMBC 2011, Boston, US,2011
4. H Gao, K Kadir, A Payne, C Berry, J Soraghan, X Lou," CMRI Based 3D Left Ventricle Motion Analysis on Patients with Acute Myocardial Infarction", EMBC 2011, Boston, US,2011

Book chapter

1. K. Kadir, A. Payne, J. Soraghan, and C. Berry, "Automatic Left Ventricle Segmentation in T_2 Weighted CMR Images," in *Image Processing and Communications Challenges 2*. vol. 84, ed: Springer Berlin / Heidelberg, pp. 247-254.

Journal submitted

1. Kushsairy Kadir, Hao Gao, Alex Payne, John Soraghan and Collin Berry," LV Wall Segmentation using Variational Level Set Method (LSM) with Additional Shape Constrain for Edema Quantification", Computerized Medical Imaging and Graphics
2. Kushsairy Kadir, Hao Gao, John Soraghan and Collin Berry," Automatic Edema Quantification from T_2 Weighted MRI: Algorithm and Assessment", Computer in Biology and Medicine

Journal in preparation

1. H. Gao, K. Kadir, A. Payne, J. Soraghan Member, IEEE and C. Berry,” Automatic Quantification of Myocardial Edema in Patients with Acute Myocardial Infarction Using Bright Blood T_2 Weighted MRI”, IEEE transaction on Biomedical Engineering.
2. Kushsairy Kadir, Hao Gao, John Soraghan and Collin Berry,” 3-D Quantification and Visualization of Edema using T_2 Weighted CMR Image’, IEEE Trans on Information Technology in Biomedicine.

References

Heart Attack (Myocardial Infarction) [Online]. Available: http://www.medicinenet.com/heart_attack/article.htm [Accessed 12 September 2011].

Abdel-Aty, H., Cocker, M., Meek, C., Tyberg, J. & Friedrich, M. 2009. Edema as a very early marker for acute myocardial ischemia: a cardiovascular magnetic resonance study. *J Am Coll Cardiol,* 53**,** 1194 - 1201.

Abdi, H. & Williams, L. J. 2010. Principal component analysis. *Wiley Interdisciplinary Reviews: Computational Statistics,* 2**,** 433-459.

Ahanathapillai, V. 2010. *Image Processing Techniques for Automated Diagnosis of Wall Motion Abnormality in Echocardiography Sequences.* PhD, University of Strathclyde.

Alanallur, A. 2009. Available: http://www.slideshare.net/arunmtek/artifacts-in-mri [Accessed 13 October 2011].

Albert C. C.S., Alison J N., Statistical 3D using a Rician Distribution. *Medical Image Computing and Computer-Assisted Intervention – MICCAI 1999.* Springer Berlin / Heidelberg.

Aletras, A., Kellman, P., Derbyshire, J. & Arai, A. 2008. ACUT2E TSE-SSFP: a hybrid method for T2-weighted imaging of edema in the heart. *Magn Reson Med,* 59**,** 229 - 235.

Altman, D. G. & Bland, J. M. 1983. Measurement in Medicine: The Analysis of Method Comparison Studies. *Journal of the Royal Statistical Society. Series D (The Statistician),* 32**,** 307-317.

Amado, L. C., Gerber, B. L., Gupta, S. N., Rettmann, D. W., Szarf, G., Schock, R., Nasir, K., Kraitchman, D. L. & Lima, J. a. C. 2004. Accurate and objective infarct sizing by contrast-enhanced magnetic resonance imaging in a canine myocardial infarction model. *J Am Coll Cardiol,* 44**,** 2383-2389.

Aquaro,G., Positano, V.,Pingitore, A. S., Elisabetta D B., Gianluca F., Francesco S., Massimo P. L. 2010. Quantitative analysis of late gadolinium enhancement in hypertrophic cardiomyopathy. Journal of Cardiovascular Magnetic Resonance, 12, 12-21

Azhari, H., Buchalter, M., Sideman, S., Shapiro, E. & Beyar, R. 1992. A conical model to describe the nonuniformity of the left ventricular twisting motion. *Annals of Biomedical Engineering,* 20**,** 149-165.

Azhari, H., Oliker, S., Rogers, W. J., Weiss, J. L. & Shapiro, E. P. 1996. Three-dimensional mapping of acute ischemic regions using artificial neural networks and tagged MRI. *Biomedical Engineering, IEEE Transactions on,* 43**,** 619-626.

Azhari, H., Sideman, S., Weiss, J. L., Shapiro, E. P., Weisfeldt, M. L., Graves, W. L., Rogers, W. J. & Beyar, R. 1990. Three-dimensional mapping of acute ischemic regions using MRI: wall thickening versus motion analysis. *American Journal of Physiology - Heart and Circulatory Physiology,* 259**,** H1492-H1503.

Bales, A. C. & Sorrentino, M. J. 1997. Causes of congestive heart failure: Prompt diagnosis may affect prognosis. *Postgraduate Medicine symposium.*

Ballinger, R. 1996. *MRI Artifacts* [Online]. Available: www.mritutor.org/lectures/artifacts508.ppt [Accessed 7th May 2011].

Baron, N., Kachenoura, N., Beygui, F., Cluze, P., Grenier, P., Herment, A. & Frouin, F. Year. Quantification of myocardial edema and necrosis during acute myocardial infarction. *In:* Computers in Cardiology, 2008, 14-17 Sept. 2008. 781-784.

Ben Ayed, I., Shuo, L. & Ross, I. 2009. Embedding Overlap Priors in Variational Left Ventricle Tracking. *Medical Imaging, IEEE Transactions on,* 28**,** 1902-1913.

Berry, C., Kellman, P., Mancini, C., Chen, M. Y., Bandettini, W. P., Lowrey, T., Hsu, L.-Y., Aletras, A. H. & Arai, A. E. 2010. Magnetic Resonance Imaging

Delineates the Ischemic Area at Risk and Myocardial Salvage in Patients With Acute Myocardial Infarction / Clinical Perspective. *Circulation: Cardiovascular Imaging,* 3**,** 527-535.

Bland, J. M. & Altman, D. G. 1999. Measuring agreement in method comparison studies. *Statistical Methods in Medical Research,* 8**,** 135-160.

Bolson, E. L., Sheehan, F. H., Legget, M. E., Jin, H., Mcdonald, J. A., Sampson, P. D., Martin, R. W., Bashein, G. & Otto, C. M. Year. Applying the CenterSurface model to 3-D reconstructions of the left ventricle for regional function analysis. *In:* Computers in Cardiology 1995, 10-13 Sep 1995. 63-66.

Bourke, P. 1999. *Interpolation methods* [Online]. Available: http://paulbourke.net/miscellaneous/interpolation/ [Accessed 2010].

Buller, V. G. M., Van Der Geest, R. J., Kool, M. D. & Reiber, J. H. C. Year. Accurate three-dimensional wall thickness measurement from multi-slice short-axis MR imaging. *In:* Computers in Cardiology 1995, 10-13 Sep 1995. 245-248.

Carlsson, M., Ubachs, J. F. A., Hedstrom, E., Heiberg, E., Jovinge, S. & Arheden, H. 2009. Myocardium at Risk After Acute Infarction in Humans on Cardiac Magnetic Resonance: Quantitative Assessment During Follow-Up and Validation With Single-Photon Emission Computed Tomography. *Journal of the American College of Cardiology: Cardiovascular Imaging,* 2**,** 569-576.

Chunming, L., Chenyang, X., Changfeng, G. & Fox, M. D. Year. Level set evolution without re-initialization: a new variational formulation. *In:* Computer Vision and Pattern Recognition, 2005. CVPR 2005. IEEE Computer Society Conference on, 20-25 June 2005. 430-436 vol. 1.

Ciofolo, C., Fradkin, M., Mory, B., Hautvast, G. & Breeuwer, M. Year. Automatic myocardium segmentation in late-enhancement MRI. *In:* Biomedical Imaging: From Nano to Macro, 2008. ISBI 2008. 5th IEEE International Symposium on, 14-17 May 2008. 225-228.

Cocosco, C. A., Netsch, T., Sénégas, J., Bystrov, D., Niessen, W. J. & Viergever, M. A. 2004. Automatic cardiac region-of-interest computation in cine 3D structural MRI. *International Congress Series,* 1268**,** 1126-1131.

Cocosco, C. A., Niessen, W. J., Netsch, T., Vonken, E.-J. P. A., Lund, G., Stork, A. & Viergever, M. A. 2008. Automatic image-driven segmentation of the ventricles in cardiac cine MRI. *Journal of Magnetic Resonance Imaging,* 28**,** 366-374.

Colantonio, S., Moroni, D. & Salvetti, O. Year. MRI left ventricle segmentation and reconstruction for the study of the heart dynamics. *In:* Signal Processing and Information Technology, 2005. Proceedings of the Fifth IEEE International Symposium on, 21-21 Dec. 2005. 213-218.

Constantinides, C., Chenoune, Y., Mousseaux, E., Roullot, E. & Frouin, F. Year. Automated heart localization for the segmentation of the ventricular cavities on cine magnetic resonance images. *In:* Computers in Cardiology, 2010, 26-29 Sept. 2010. 911-914.

Cootes, T. F., Edwards, G. J. & Taylor, C. J. 2001. Active appearance models. *Pattern Analysis and Machine Intelligence, IEEE Transactions on,* 23**,** 681-685.

Cootes, T. F., J.Taylor, C., Cooper, D. H. & Graham, J. 1995. Active shape models-their training and application. *Comput. Vsi. Image Understanding,* 61**,** 38-59.

Couprie, M. & Bertrand, G. 2004. Topology preserving alternating sequential filter for smoothing two-dimensional and three-dimensional objects. *J. Electron. Imaging,* 13**,** 720.

Dempster, A. P., Laird, N. M. & Rubin, D. B. 1977. Maximum Likelihood from Incomplete Data via the EM Algorithm. *Journal of the Royal Statistical Society. Series B (Methodological),* 39**,** 1-38.

Dempster Ap, L. N., Rubin Db 1977. Maximum likelihood from incomplete data via the EM algorithm. *JOURNAL OF THE ROYAL STATISTICAL SOCIETY, SERIES B* 39**,** 1-38.

Dice, L. R. 1945. Measures of the Amount of Ecologic Association Between Species. *Ecology,* 26**,** 297-302.

Dikici, E., O'donnell, T., Setser, R. & White, R. 2004. Quantification of Delayed Enhancement MR Images. *In:* Barillot, C., Haynor, D. & Hellier, P. (eds.) *Medical Image Computing and Computer-Assisted Intervention – MICCAI 2004.* Springer Berlin / Heidelberg.

El Berbari, R., Bloch, I., Redheuil, A., Angelini, E., Mousseaux, E., Frouin, F. & Herment, A. 2007. Automated Segmentation of the Left Ventricle Including Papillary Muscles in Cardiac Magnetic Resonance Images. *In:* Sachse, F. & Seemann, G. (eds.) *Functional Imaging and Modeling of the Heart.* Springer Berlin / Heidelberg.

Elagouni, K., Ciofolo-Veit, C. & Mory, B. Year. Automatic segmentation of pathological tissues in cardiac MRI. *In:* Biomedical Imaging: From Nano to Macro, 2010 IEEE International Symposium on, 14-17 April 2010. 472-475.

F. Catté, P.L. Lions, J.M. Morel & Coll, T. 1992. Image Selective Smoothing and Edge Detection by Nonlinear Diffusion. *SIAM Journal on Numerical Analysis,* 29(1)**,** 182-193.

Farin, G. 1997. *Curves and Surfaces for Computer Aided Geometric Design—A Practical Guide,* New York, Academic Press.

Fieno, D. S., Kim, R. J., Chen, E.-L., Lomasney, J. W., Klocke, F. J. & Judd, R. M. 2000. Contrast-enhanced magnetic resonance imaging of myocardium at risk : Distinction between reversible and irreversible injury throughout infarct healing. *Journal of the American College of Cardiology,* 36**,** 1985-1991.

Frangi, A. F., Niessen, W. J. & Viergever, M. A. 2001. Three-dimensional modeling for functional analysis of cardiac images, a review. *Medical Imaging, IEEE Transactions on,* 20**,** 2-5.

Frangi, A. F., Rueckert, D., Schnabel, J. A. & Niessen, W. J. 2002. Automatic construction of multiple-object three-dimensional statistical shape models:

application to cardiac modeling. *Medical Imaging, IEEE Transactions on,* 21**,** 1151-1166.

Fritscher, K., Grünerbl, A. & Schubert, R. 2007. 3D image segmentation using combined shape-intensity prior models. *International Journal of Computer Assisted Radiology and Surgery,* 1**,** 341-350.

G. J. Tortora & Derrickson, B. H. 2005. *Principle of Anatomy and Physiology*, Wiley.

Gelberg, H., Brundage, B., Glantz, S. & Parmley, W. 1979. Quantitative left ventricular wall motion analysis: a comparison of area, chord and radial methods. *Circulation,* 59**,** 991-1000.

Gerig, G., Kubler, O., Kikinis, R. & Jolesz, F. A. 1992. Nonlinear anisotropic filtering of MRI data. *Medical Imaging, IEEE Transactions on,* 11**,** 221-232.

Gering, D. 2003. Automatic Segmentation of Cardiac MRI. *In:* Ellis, R. & Peters, T. (eds.) *Medical Image Computing and Computer-Assisted Intervention - MICCAI 2003.* Springer Berlin / Heidelberg.

Giri, S., Chung, Y.-C., Merchant, A., Mihai, G., Rajagopalan, S., Raman, S. & Simonetti, O. 2009. T2 quantification for improved detection of myocardial edema. *Journal of Cardiovascular Magnetic Resonance,* 11**,** 56.

Green, J. D., Clarke, J. R., Flewitt, J. A. & Friedrich, M. G. 2009. Single-shot steady-state free precession can detect myocardial edema in patients: A feasibility study. *Journal of Magnetic Resonance Imaging,* 30**,** 690-695.

Gudbjartsson, H. & Patz, S. 1995a. The Rician distribution of noisy MRI data. *Magnetic resonance in medicine : official journal of the Society of Magnetic Resonance in Medicine / Society of Magnetic Resonance in Medicine,* 34**,** 910-4.

Gudbjartsson, H. & Patz, S. 1995b. The rician distribution of noisy mri data. *Magnetic Resonance in Medicine,* 34**,** 910-914.

Hae-Yeoun, L., Codella, N. C. F., Cham, M. D., Weinsaft, J. W. & Yi, W. 2010. Automatic Left Ventricle Segmentation Using Iterative Thresholding and an Active Contour Model With Adaptation on Short-Axis Cardiac MRI. *Biomedical Engineering, IEEE Transactions on,* 57**,** 905-913.

Hautvast, G. L. T. F., Breeuwer, M., Lobregt, S., Vilanova, A. & Gerritsen, F. A. 2005. Automatic cardiac contour propagation in short axis cardiac MR images. *International Congress Series,* 1281**,** 351-356.

Heiberg, E., Ugander, M., Engblom, H., Götberg, M., Olivecrona, G. K., Erlinge, D. & Arheden, H. 2008. Automated Quantification of Myocardial Infarction from MR Images by Accounting for Partial Volume Effects: Animal, Phantom, and Human Study1. *Radiology,* 246**,** 581-588.

Hennemuth, A., Seeger, A., Friman, O., Miller, S., Klumpp, B., Oeltze, S. & Peitgen, H. O. 2008. A Comprehensive Approach to the Analysis of Contrast Enhanced Cardiac MR Images. *Medical Imaging, IEEE Transactions on,* 27**,** 1592-1610.

Herman, G. T., Zheng, J. & Bucholtz, C. A. 1992. Shape-based interpolation. *Computer Graphics and Applications, IEEE,* 12**,** 69-79.

Hesselink, J. R. 2003. *Basic Principles of MR Imaging* [Online]. Available: http://spinwarp.ucsd.edu/NeuroWeb/Text/br-100.htm [Accessed 3 Oct 2011].

Honghai, Z., Wahle, A., Johnson, R. K., Scholz, T. D. & Sonka, M. 2010. 4-D Cardiac MR Image Analysis: Left and Right Ventricular Morphology and Function. *Medical Imaging, IEEE Transactions on,* 29**,** 350-364.

Hornak, J. P. 1996. *The Basics of MRI* [Online]. Available: http://www.cis.rit.edu/htbooks/mri/index.html [Accessed 28 January 2009].

Hsu, L.-Y., Natanzon, A., Kellman, P., Hirsch, G. A., Aletras, A. H. & Arai, A. E. 2006. Quantitative myocardial infarction on delayed enhancement MRI. Part I: Animal validation of an automated feature analysis and combined thresholding infarct sizing algorithm. *Journal of Magnetic Resonance Imaging,* 23**,** 298-308.

Huang, W. C. & Goldgof, D. B. 1993. Adaptive-size meshes for rigid and nonrigid shape analysis and synthesis. *Pattern Analysis and Machine Intelligence, IEEE Transactions on,* 15**,** 611-616.

Jerry L. Prince & Links, J. M. 2006. *Medical Imaging Signals and Systems*, Pearson Prentice Hall.

Jia, L., Gangyi, D. & Yuwei, W. Year. Segmentation of the Left Ventricle from Cardiac MR Images Based on Radial GVF Snake. *In:* BioMedical Engineering and Informatics, 2008. BMEI 2008. International Conference on, 27-30 May 2008 2008. 238-242.

Jinsoo, C., Brummer, M. & Benkeser, P. J. Year. Velocity-aided cardiac segmentation. *In:* Engineering in Medicine and Biology Society, 2003. Proceedings of the 25th Annual International Conference of the IEEE, 17-21 Sept. 2003. 622-625 Vol.1.

Johnstone, R. I., Greenwood, J. P., Biglands, J. D., Plein, S., Ridgway, J. P. & Radjenovic, A. 2011. Assessment of tissue edema in patients with acute myocardial infarction by computer-assisted quantification of triple inversion recovery prepared MRI of the myocardium. *Magnetic resonance in medicine : official journal of the Society of Magnetic Resonance in Medicine / Society of Magnetic Resonance in Medicine*.

Jolly, M.-P. 2006. Automatic Segmentation of the Left Ventricle in Cardiac MR and CT Images. *International Journal of Computer Vision,* 70**,** 151-163.

Jolly, M.-P. 2008. Automatic Recovery of the Left Ventricular Blood Pool in Cardiac Cine MR Images. *In:* Metaxas, D., Axel, L., Fichtinger, G. & Székely, G. (eds.) *Medical Image Computing and Computer-Assisted Intervention – MICCAI 2008.* Springer Berlin / Heidelberg.

Junzhou, H., Xiaolei, H., Metaxas, D. & Axel, L. Year. DYNAMIC TEXTURE BASED HEART LOCALIZATION AND SEGMENTATION IN 4-D CARDIAC

IMAGES. *In:* Biomedical Imaging: From Nano to Macro, 2007. ISBI 2007. 4th IEEE International Symposium on, 12-15 April 2007. 852-855.

Kachenoura, N., Redheuil, A., Herment, A., Mousseaux, E. & Frouin, F. 2008. Robust assessment of the transmural extent of myocardial infarction in late gadolinium-enhanced MRI studies using appropriate angular and circumferential subdivision of the myocardium. *European Radiology,* 18**,** 2140-2147.

Kadir, K., Gao, H., Payne, A., Soraghan, J. & Berry, C. July,2011. VARIATIONAL LEVEL SET METHOD WITH SHAPE CONSTRAINT AND APPLICATION TO OEDEMA CARDIAC MAGNETIC RESONANCE IMAGE. *DSP 2011.* Corfu, Greece.

Kadir, K., Payne, A., Soraghan, J. & Berry, C. 2010a. Automatic Left Ventricle Segmentation in T2 Weighted CMR Images. *Image Processing and Communications Challenges 2.* Springer Berlin / Heidelberg.

Kadir, K., Payne, A., Soraghan, J. J. & Berry, C. 2010b. Automatic Quantification of Oedema from T2 Weighted CMR Image using a Hybrid Thresholding Oedema Sizing Algorithm (HTOSA). *Computing in Cardiology.* Belfast, United Kingdom.

Kass, M., Witkin, A. & Terzopoulos, D. 1988. Snakes: Active contour models. *INTERNATIONAL JOURNAL OF COMPUTER VISION,* 1**,** 321--331.

Kellman, P., Aletras, A. H., Mancini, C., Mcveigh, E. R. & Arai, A. E. 2007. T2-prepared SSFP improves diagnostic confidence in edema imaging in acute myocardial infarction compared to turbo spin echo. *Magnetic Resonance in Medicine,* 57**,** 891-897.

Kim, R. J., Fieno, D. S., Parrish, T. B., Harris, K., Chen, E.-L., Simonetti, O., Bundy, J., Finn, J. P., Klocke, F. J. & Judd, R. M. 1999. Relationship of MRI Delayed Contrast Enhancement to Irreversible Injury, Infarct Age, and Contractile Function. *Circulation,* 100**,** 1992-2002.

Kim, R. J., Wu, E., Rafael, A., Chen, E.-L., Parker, M. A., Simonetti, O., Klocke, F. J., Bonow, R. O. & Judd, R. M. 2000. The Use of Contrast-Enhanced Magnetic

Resonance Imaging to Identify Reversible Myocardial Dysfunction. *New England Journal of Medicine,* 343**,** 1445-1453.

Kurkure, U., Pednekar, A., Muthupillai, R., Flamm, S. D. & Kakadiaris, I. A. 2009. Localization and Segmentation of Left Ventricle in Cardiac Cine-MR Images. *Biomedical Engineering, IEEE Transactions on,* 56**,** 1360-1370.

Lauterbur, P. C. 1973. Image Formation by Induced Local Interactions: Examples Employing Nuclear Magnetic Resonance. *Nature,* 242**,** 190-191.

Lehmann, H., Kneser, R., Neizel, M., Peters, J., Ecabert, O., Kühl, H., Kelm, M. & Weese, J. 2009. Integrating Viability Information into a Cardiac Model for Interventional Guidance. *In:* Ayache, N., Delingette, H. & Sermesant, M. (eds.) *Functional Imaging and Modeling of the Heart.* Springer Berlin / Heidelberg.

Li, P., Prince, J. L., Lima, J. a. C. & Osman, N. F. 2005. Fast tracking of cardiac motion using 3D-HARP. *Biomedical Engineering, IEEE Transactions on,* 52**,** 1425-1435.

Liang, Z.-P. & Lauterbur, P. C. 2000. *Principles of Magnetic Resonance Imaging: A Signal Processing Perspective*, SPIE Optical Engineering Press.

Liang, Z. P. & Lauterburgh, P. 2000. *Principle of Magnetic Resonance Imaging: A Signal Processing Perspective*, SPIE Optocal Engineering Press.

Lieberman, A., Weiss, J., Jugdutt, B., Becker, L., Bulkley, B., Garrison, J., Hutchins, G., Kallman, C. & Weisfeldt, M. 1981. Two-dimensional echocardiography and infarct size: relationship of regional wall motion and thickening to the extent of myocardial infarction in the dog. *Circulation,* 63**,** 739-746.

Lin, X., Cowan, B. & Young, A. 2006. Automated Detection of Left Ventricle in 4D MR Images: Experience from a Large Study. *In:* Larsen, R., Nielsen, M. & Sporring, J. (eds.) *Medical Image Computing and Computer-Assisted Intervention – MICCAI 2006.* Springer Berlin / Heidelberg.

Lorenzo-Valdés, M., Sanchez-Ortiz, G., Mohiaddin, R. & Rueckert, D. 2002. Atlas-Based Segmentation and Tracking of 3D Cardiac MR Images Using Non-rigid Registration. *In:* Dohi, T. & Kikinis, R. (eds.) *Medical Image Computing and Computer-Assisted Intervention — MICCAI 2002.* Springer Berlin / Heidelberg.

Lorenzo-Valdés, M., Sanchez-Ortiz, G. I., Elkington, A. G., Mohiaddin, R. H. & Rueckert, D. 2004. Segmentation of 4D cardiac MR images using a probabilistic atlas and the EM algorithm. *Medical Image Analysis,* 8**,** 255-265.

Lynch, M., Ghita, O. & Whelan, P. F. 2006a. Automatic segmentation of the left ventricle cavity and myocardium in MRI data. *Computers in Biology and Medicine,* 36**,** 389-407.

Lynch, M., Ghita, O. & Whelan, P. F. 2006b. Left-ventricle myocardium segmentation using a coupled level-set with a priori knowledge. *Computerized Medical Imaging and Graphics,* 30**,** 255-262.

Lynch, M., Ghita, O. & Whelan, P. F. 2008. Segmentation of the Left Ventricle of the Heart in 3-D+t MRI Data Using an Optimized Nonrigid Temporal Model. *Medical Imaging, IEEE Transactions on,* 27**,** 195-203.

Lynch, M., Ilea, D., Robinson, K., Ghita, O. & Whelan, P. F. 2007. Automatic seed initialization for the expectation-maximization algorithm and its application in 3D medical imaging. *Journal of Medical Engineering & Technology,* 31**,** 332-340.

Macgregor, A. 2009, pp 230-266. Scottish Health survey 2008. *In:* Bromley, C., Bradshaw, P. & Given, L. (eds.). Endiburgh: National Statistic.

Mahrholdt, H., Wagner, A., Parker, M., Regenfus, M., Fieno, D. S., Bonow, R. O., Kim, R. J. & Judd, R. M. 2003. Relationship of contractile function to transmural extent of infarction in patients with chronic coronary artery disease. *J Am Coll Cardiol,* 42**,** 505-512.

Malladi, R., Sethian, J. A. & Vemuri, B. C. 1995. Shape modeling with front propagation: a level set approach. *Pattern Analysis and Machine Intelligence, IEEE Transactions on,* 17**,** 158-175.

Mansfield, P. 1977. Multi-planar image formation using NMR spin echoes. *Journal of Physics C: Solid State Physics,* 10**,** L55.

Maragos, P. & Schafer, R. W. 1990. Morphological systems for multidimensional signal processing. *Proceedings of the IEEE,* 78**,** 690-710.

Martini, F. & Nath, J. 2009. *Fundamentals of Anatomy & Physiology* Pearson.

Mcgill, R., Tukey, J. W. & Larsen, W. A. 1978. Variations of Box Plots. *The American Statistician,* 32**,** 12-16.

Medicinenet. *Heart Attack* [Online]. Available: http://www.medicinenet.com/heart_attack/article.htm [Accessed 18 June 2011].

Mitchell, Lieveldt, S., Geest, B. V. D., Reiber, H. C. & Sonka, M. 2000. Segmentation of cardiac MR images: an active appearance model approach. *Proc. SPIE Medical Imaging,* 3979**,** 224-234.

Mitchell, S. C., Bosch, J. G., Lelieveldt, B. P. F., Van Der Geest, R. J., Reiber, J. H. C. & Sonka, M. 2002. 3-D active appearance models: segmentation of cardiac MR and ultrasound images. *Medical Imaging, IEEE Transactions on,* 21**,** 1167-1178.

Mitchell, S. C., Lelieveldt, B. P. F., Van Der Geest, R. J., Bosch, H. G., Reiver, J. H. C. & Sonka, M. 2001. Multistage hybrid active appearance model matching: segmentation of left and right ventricles in cardiac MR images. *Medical Imaging, IEEE Transactions on,* 20**,** 415-423.

Miyamoto, M., Mcclure, D. E., Schertel, E. R., Andrews, P. J., Jones, G. A., Pratt, J. W., Ross, P. & Myerowitz, P. D. 1998. Effects of hypoproteinemia-induced myocardial edema on left ventricular function. *American Journal of Physiology - Heart and Circulatory Physiology,* 274**,** H937-H944.

Mrc Cognition and Brain Sciences Unit. 2008. Available: http://www.mrc-cbu.cam.ac.uk/facilities/mri/ [Accessed 21 July 2011].

Najarian, K. & Splinter, R. 2006. *biomedical Signal and Image Processing*, Taylor&Francis.

National Heart Lung and Blood Institute. *What Is Coronary Artery Disease?* [Online]. Available: http://www.nhlbi.nih.gov/health/dci/Diseases/Cad/CAD_WhatIs.html [Accessed 21 July 2011].

Noble, N., Hill, D., Breeuwer, M. & Razavi, R. 2004. The Automatic Identification of Hibernating Myocardium Medical Image Computing and Computer-Assisted Intervention – MICCAI 2004. *In:* Barillot, C., Haynor, D. & Hellier, P. (eds.). Springer Berlin / Heidelberg.

O'brien, S. P., Ghita, O. & Whelan, P. F. 2011. A Novel Model-Based 3D+Time Left Ventricular Segmentation Technique. *Medical Imaging, IEEE Transactions on,* 30**,** 461-474.

Ordas, S. & Frangi, A. F. Year. Automatic Quantitative Analysis of Myocardial Wall Motion and Thickening from Long-and Short-Axis Cine MRI Studies. *In:* Engineering in Medicine and Biology Society, 2005. IEEE-EMBS 2005. 27th Annual International Conference of the, 17-18 Jan. 2006 2005. 7028-7031.

Osher, S. & Sethian, J. A. 1988. Fronts propagating with curvature-dependent speed: Algorithms based on Hamilton-Jacobi formulations. *Journal of Computational Physics,* 79**,** 12-49.

Papageorgiou, C. P., Oren, M. & Poggio, T. Year. A general framework for object detection. *In:* Computer Vision, 1998. Sixth International Conference on, 4-7 Jan 1998. 555-562.

Paragios, N. 2003. A level set approach for shape-driven segmentation and tracking of the left ventricle. *Medical Imaging, IEEE Transactions on,* 22**,** 773-776.

Pavani, S.-K., Delgado, D. & Frangi, A. F. 2010. Haar-like features with optimally weighted rectangles for rapid object detection. *Pattern Recognition,* 43**,** 160-172.

Payne, A. R., Casey, M., Mcclure, J., Mcgeoch, R., Murphy, A., Woodward, R., Saul, A., Bi, X., Zuehlsdorff, S., Oldroyd, K. G., Tzemos, N. & Berry, C. 2011. Bright Blood T2 Weighted MRI Has Higher Diagnostic Accuracy Than Dark Blood STIR MRI for Detection of Acute Myocardial Infarction and for Assessment of the Ischemic Area-at-Risk and Myocardial Salvage. *Circulation: Cardiovascular Imaging*.

Pednekar, A., Kurkure, U., Muthupillai, R., Flamm, S. & Kakadiaris, I. A. 2006. Automated left ventricular segmentation in cardiac MRI. *Biomedical Engineering, IEEE Transactions on,* 53**,** 1425-1428.

Perona, P. & Malik, J. 1990. Scale-space and edge detection using anisotropic diffusion. *Pattern Analysis and Machine Intelligence, IEEE Transactions on,* 12**,** 629-639.

Petitjean, C. & Dacher, J.-N. 2011. A review of segmentation methods in short axis cardiac MR images. *Medical Image Analysis,* 15**,** 169-184.

Pham, D. L., Xu, C. & Prince, J. L. 2000. CURRENT METHODS IN MEDICAL IMAGE SEGMENTATION1. *Annual Review of Biomedical Engineering,* 2**,** 315-337.

Pluempitiwiriyawej, C. 2003. *Cardiac MR Image Segmentation STACS, A New Active Contour Scheme.* Electrical and Computer Engineering Phd, Carnegie Mellon.

Pluempitiwiriyawej, C., Moura, J. M. F., Yi-Jen Lin, W. & Chien, H. 2005. STACS: new active contour scheme for cardiac MR image segmentation. *Medical Imaging, IEEE Transactions on,* 24**,** 593-603.

Positano, V., Pingitore, A., Giorgetti, A., Favilli, B., Santarelli, M. F., Landini, L., Marzullo, P. & Lombardi, M. 2005. A Fast and Effective Method to Assess Myocardial Necrosis by Means of Contrast Magnetic Resonance Imaging. *Journal of Cardiovascular Magnetic Resonance,* 7**,** 487-494.

Positano, V., Santarelli, M. F., Pingitore, A., Lombardi, M., Landini, L. & Benassi, A. Year. Quantitative 3D assessment of myocardial viability with MRI delayed contrast enhancement. *In:* Computers in Cardiology, 2003, 21-24 Sept. 2003. 629-632.

Preparata, F. P. & Hong, S. J. 1977. Convex hulls of finite sets of points in two and three dimensions. *Commun. ACM,* 20**,** 87-93.

Punithakumar, K., Ben Ayed, I., Ross, I. G., Islam, A., Chong, J. & Shuo, L. 2010. Detection of Left Ventricular Motion Abnormality Via Information Measures and Bayesian Filtering. *Information Technology in Biomedicine, IEEE Transactions on,* 14**,** 1106-1113.

Reimer, K., Lowe, J., Rasmussen, M. & Jennings, R. 1977. The wavefront phenomenon of ischemic cell death. 1. Myocardial infarct size vs duration of coronary occlusion in dogs. *Circulation,* 56**,** 786-794.

Remme, E. W., Young, A. A., Augenstein, K. F., Cowan, B. & Hunter, P. J. 2004. Extraction and quantification of left ventricular deformation modes. *Biomedical Engineering, IEEE Transactions on,* 51**,** 1923-1931.

Richard Bitar, G. L., Richard Perng, Sameh Tadros, Alan R Moody, Josee Sarrazin, Caitlin Mcgregor, Monique Christakis, Sean Symons, Andrew Nelson, and Timothy P Roberts 2006. MR pulse sequences: what every radiologist wants to know but is afraid to ask. *Radiographics,* 26(2)**,** 513-537.

Robb, R. A. 1999. 3-D Visualization in Biomedical Applications. *Annual Review of Biomedical Engineering,* 1**,** 377-399.

Ruan, C. *MRI Artifacts: Mechanism and Control* [Online]. Available: http://ric.uthscsa.edu/personalpages/lancaster/DI2_Projects_2003/MRI_Artifacts.pdf [Accessed 7th May 2009].

S.K.Setarehdan & J.J.Soraghan 1997. Automatic Left Ventricular Centre Point Extraction in Echocardiographic Images. *Signal Processing Journal, EURASIP,* 61**,** 275-288.

Santarelli, M. F., Positano, V., Landini, L. & Benassi, A. Year. A new algorithm for 3D automatic detection and tracking of cardiac wall motion. *In:* Computers in Cardiology 1999. 133-136.

Santarelli, M. F., Positano, V., Michelassi, C., Lombardi, M. & Landini, L. 2003. Automated cardiac MR image segmentation: theory and measurement evaluation. *Medical Engineering & Physics,* 25**,** 149-159.

Savoy, R. & Jovicich, J. 2001. *MRI glossary* [Online]. Available: http://web.mit.edu/hst.583/www/course2001/LECTURES/MRIglossary.pdf [Accessed 7th May 2011].

Setser, R. M., Bexell, D. G., O'donnell, T. P., Stillman, A. E., Lieber, M. L., Schoenhagen, P. & White, R. D. 2003. Quantitative assessment of myocardial scar in delayed enhancement magnetic resonance imaging. *Journal of Magnetic Resonance Imaging,* 18**,** 434-441.

Smith, T. B. & Nayak, K. S. 2010. MRI artifacts and correction strategies. *Imaging in Medicine,* 2**,** 445-457.

Stalidis, G., Maglaveras, N., Efstratiadis, S. N., Dimitriadis, A. S. & Pappas, C. 2002. Model-based processing scheme for quantitative 4-D cardiac MRI analysis. *Information Technology in Biomedicine, IEEE Transactions on,* 6**,** 59-72.

Sun, H., Avants, B. B., Frangi, A. F., Sukno, F., Gee, J. C. & Yushkevich, P. A. 2008. Cardiac Medial Modeling and Time-Course Heart Wall Thickness Analysis. *Proceedings of the 11th International Conference on Medical Image Computing and Computer-Assisted Intervention, Part II.* New York, New York: Springer-Verlag.

Taratorin, A. M. & Sideman, S. 1995. 3D functional mapping of left ventricular dynamics. *Computerized Medical Imaging and Graphics,* 19**,** 113-129.

Termeer, M., Bescos, J. O., Breeuwer, M., Vilanova, A., Gerritsen, F. & Groller, M. E. 2007. CoViCAD: Comprehensive Visualization of Coronary Artery Disease. *Visualization and Computer Graphics, IEEE Transactions on,* 13**,** 1632-1639.

Thiele, H., Kappl, M. J. E., Conradi, S., Niebauer, J., Hambrecht, R. & Schuler, G. 2006. Reproducibility of Chronic and Acute Infarct Size Measurement by Delayed Enhancement-Magnetic Resonance Imaging. *J Am Coll Cardiol,* 47**,** 1641-1645.

Ting, C., Babb, J., Kellman, P., Axel, L. & Kim, D. 2008. Semiautomated Segmentation of Myocardial Contours for Fast Strain Analysis in Cine Displacement-Encoded MRI. *Medical Imaging, IEEE Transactions on,* 27**,** 1084-1094.

Tobon-Gomez, C., Butakoff, C., Yushkevich, P., Huguet, M. & Frangi, A. F. Year. 3D mesh based wall thickness measurement: Identification of left ventricular hypertrophy phenotypes. *In:* Engineering in Medicine and Biology Society (EMBC), 2010 Annual International Conference of the IEEE, Aug. 31 2010-Sept. 4 2010. 2642-2645.

Van Assen, H. C., Danilouchkine, M. G., Frangi, A. F., Ordás, S., Westenberg, J. J. M., Reiber, J. H. C. & Lelieveldt, B. P. F. 2006. SPASM: A 3D-ASM for segmentation of sparse and arbitrarily oriented cardiac MRI data. *Medical Image Analysis,* 10**,** 286-303.

Van De Werf, F., Bax, J., Betriu, A. & Al, E. 2008. Management of acute myocardial infarction in patients presenting with persistent ST-segment elevation. *European Heart Journal,* 29**,** 2909-2945.

Viola, P. & Jones, M. Year. Rapid object detection using a boosted cascade of simple features. *In:* Computer Vision and Pattern Recognition, 2001. CVPR 2001. Proceedings of the 2001 IEEE Computer Society Conference on, 2001. I-511-I-518 vol.1.

Weishaupt, D., Köchli, V. D. & Marincek, B. 2006. *How Does MRI Work? An Introduction to the Physics and Function of Magnetic Resonance Imaging*, Springer-Verlag Berlin Heidelberg.

Weishaupt, D., Kochli, V. D., Marincek, B. & Kim, E. E. 2007. How Does MRI Work? An Introduction to the Physics and Function of Magnetic Resonance Imaging. *J Nucl Med,* 48**,** 1910-.

Xiahai, Z., Rhode, K. S., Razavi, R. S., Hawkes, D. J. & Ourselin, S. 2010. A Registration-Based Propagation Framework for Automatic Whole Heart Segmentation of Cardiac MRI. *Medical Imaging, IEEE Transactions on,* 29**,** 1612-1625.

Xiang, L. 2008. *Model-based strategies for automated segmentation of cardiac magnetic resonance images.* PhD, The university of Auckland.

Yuwei, W., Yuanquan, W. & Kun, L. Year. Snake Model-Based Automatic Segmentation of the Left Ventricle from Cardiac MR Images. *In:* Biomedical Engineering and Informatics, 2009. BMEI '09. 2nd International Conference on, 17-19 Oct. 2009. 1-5.

Zhuang, X., Hawkes, D., Crum, W., Boubertakh, R., Uribe, S., Atkinson, D., Batchelor, P., Schaeffter, T., Razavi, R. & Hill, D. Year. Robust registration between cardiac MRI images and atlas for segmentation propagation. *In:* Society of Photonic-Optical Instrumentation Engineers(SPIE) Conference, 2008. 691408.

Zijdenbos, A. P., Dawant, B. M., Margolin, R. A. & Palmer, A. C. 1994a. Morphometric analysis of white matter lesions in MR images: method and validation. *IEEE transactions on medical imaging,* 13**,** 716-24.